

ELECTROMAGNETIC CRYSTAL BASED TERAHERTZ
THERMAL RADIATORS AND COMPONENTS

by

Ziran Wu

A Dissertation Submitted to the Faculty of the

DEPARTMENT OF PHYSICS

In Partial Fulfillment of the Requirements

For the Degree of

DOCTOR OF PHILOSOPHY

In the Graduate College

THE UNIVERSITY OF ARIZONA

2010

THE UNIVERSITY OF ARIZONA
GRADUATE COLLEGE

As members of the Dissertation Committee, we certify that we have read the dissertation prepared by Ziran Wu entitled Electromagnetic Crystal based Terahertz Thermal Radiators and Components and recommend that it be accepted as fulfilling the dissertation requirement for the Degree of Doctor of Philosophy.

_____ Date: 05/12/2010
Hao Xin

_____ Date: 05/12/2010
Li-Zhi Fang

_____ Date: 05/12/2010
Michael Shupe

_____ Date: 05/12/2010
Richard Ziolkowski

_____ Date: 05/12/2010
William Bickel

Final approval and acceptance of this dissertation is contingent upon the candidate's submission of the final copies of the dissertation to the Graduate College.

I hereby certify that I have read this dissertation prepared under my direction and recommend that it be accepted as fulfilling the dissertation requirement.

_____ Date: 05/12/2010
Dissertation Director: Hao Xin

STATEMENT BY AUTHOR

This dissertation has been submitted in partial fulfillment of requirements for an advanced degree at The University of Arizona and is deposited in the University Library to be made available to borrowers under rules of the Library.

Brief quotations from this dissertation are allowable without special permission, provided that accurate acknowledgment of source is made. Requests for permission for extended quotation from or reproduction of this manuscript in whole or in part may be granted by the head of the major department or the Dean of the Graduate College when in his or her judgment the proposed use of the material is in the interests of scholarship. In all other instances, however, permission must be obtained from the author.

SIGNED: Ziran Wu

ACKNOWLEDGEMENT

I am grateful to my advisor Professor. Hao Xin for his insight, advice, training, and support throughout this dissertation work, which have been crucial to its success. I enjoyed working with him and appreciate the efforts he has been putting on me. I gained a lot during the personal communication with him as well. I would also like to thank all the dissertation committee members for reading the dissertation and all the support they offered.

I owe many thanks to Abram Young at Physics Department for his great tutorial on FTS and THz-TDS instruments as well as many experimental skills, to Professor Richard Ziolkowski at ECE Department for the insightful discussions and patient answering of my research questions, to Professor Gehm and Wei-Ren Ng at ECE Department for their continuous support on sample fabrication, to Craig Kulesa, Christopher Groppi, Patrick, and Professor Christopher Walker at Astronomy Department for their generous offer of lab space, equipments and help on our thermal emission measurement, to Lu Wang in my group for her help on polymer metallization, sample preparation and dissertation writing as well as wonderful discussions about research, to Rongguo Zhou in my group for communications about research and lift, to Ian Zimmerman in my group for the days and nights together down in the Astronomy basement during the measurement week and his selfless coverage of my work duty so that I can have more time writing this dissertation, to Jiamin Xue at Physics Department and TC Chen in my group for their assistance on equipments and tools, and to Professor Hualiang Zhang as the former group member for helpful discussion and career advices. I also wish to thank all the members in the mmW Antennas and Circuits group for the past good times.

I would like to dedicate this dissertation to my beloved wife Xiaoyan Tu, who corrected my long-time procrastination problem and put my life into plans. Also, heartiness love and support from her all the time. I am forever grateful to my father Wencang Wu, my mother Shuheng Zhang, and the rest of my family for the unreserved love and support they have been giving to me over my life. I also would like to appreciate my dear friends Xinyu Miao and Si Wu at Physics Department for the meaningless but happy past-time they spent with me, as well as highs and lows we shared together.

TABLE OF CONTENTS

LIST OF FIGURES	7
LIST OF TABLES	11
ABSTRACT	12
CHAPTER 1. INTRODUCTION.....	15
1.1. BACKGROUND.....	15
1.1.1. Terahertz Technology	15
1.1.2. Electromagnetic Crystal Background and Application at THz.....	21
1.2. MOTIVATION.....	25
1.3. DISSERTATION ORGANIZATION.....	30
CHAPTER 2. THERMAL RADIATION FROM 3-D THz EMXT [54].....	33
2.1. MOTIVATION AND THEORETICAL PRINCIPLES.....	34
2.1.1. Motivation.....	34
2.1.2. Theoretical Principles	37
2.2. THz EMXT THERMAL EMISSIVITY CALCULATIONS.....	40
2.2.1. Woodpile EM Crystals.....	40
2.2.1.1. Silicon Woodpile Structure	40
2.2.1.2. Tungsten Woodpile Structure.....	47
2.2.2. Photonic Cavity Array	50
2.3. SAMPLE FABRICATION AND CHARACTERIZATION	55
2.3.1. Fabrication of THz Silicon Woodpile EMXT	55
2.3.2. Sample THz Characterizations	56
2.3.2.1. Comparison of THz Characterization Instruments.....	56
2.3.2.2. Sample Characterization Results.....	60
2.4. SAMPLE THERMAL EMISSIVITY MEASUREMENT	64
2.4.1. Experiment Setup.....	64
2.4.2. Calibration Scheme and Measurement Results.....	67
2.5. CONCLUSION AND DISCUSSION	72
CHAPTER 3. RAPID PROTOTYPING OF THz EMXT STRUCTURES [161].....	76
3.1. BACKGROUND AND MOTIVATION	77
3.2. THz RAPID PROTOTYPING BY POLYMER JETTING TECHNIQUE	79
3.3. THz 3-D EMXT EXAMPLES FOR DEMONSTRATION	83
3.3.1. Build Materials Characterization	83
3.3.2. Woodpile Structure	88
3.3.3. Johnson Structure.....	93
3.3.4. Photonic Cavity Array	97
3.4. CONCLUSION AND FUTURE WORK	99

TABLE OF CONTENTS - *Continued*

CHAPTER 4.	THZ WAVEGUIDE BASED ON HOLLOW-CORE EMXT FIBER [162].....	101
4.1.	BACKGROUND AND MOTIVATION	101
4.2.	THZ EMXT WAVEGUIDE DESIGN	103
4.2.1.	Design Procedures	103
4.2.1.1.	<i>Eigen-mode Simulations</i>	104
4.2.1.2.	<i>Driven Model Simulations</i>	106
4.2.2.	Parametric Study of Design Variables	110
4.2.2.1.	<i>Number of Cladding Rings</i>	111
4.2.2.2.	<i>Waveguide Length</i>	112
4.2.2.3.	<i>Defect Core Radius</i>	114
4.2.2.4.	<i>Build Material Loss</i>	116
4.3.	EXPERIMENTAL CHARACTERIZATION OF THE WAVEGUIDE LOSS.....	119
4.4.	CONCLUSION AND DISCUSSION	125
CHAPTER 5.	OTHER EMXT BASED THZ COMPONENTS TOWARD INTEGRATED MICROSYSTEMS	127
5.1.	THZ EMXT HORN ANTENNA	128
5.1.1.	Background and Motivation	128
5.1.2.	Antenna Designs and Simulations	131
5.1.3.	EMXT Antenna Fabrication and Measurement Plan.....	140
5.2.	THZ WAVEGUIDE TO MICROSTRIP LINE TRANSITION.....	143
5.2.1.	Motivation and Existing Transition Architects.....	143
5.2.2.	Transition Structure Design and Simulations	147
5.3.	CONCLUSION AND FUTURE WORK	155
CHAPTER 6.	CONCLUSIONS AND FUTURE WORKS	159
REFERENCES	169

LIST OF FIGURES

Figure 1-1. Schematic electromagnetic spectrum showing THz gap located in between electronics and photonics [5].	16
Figure 1-2. Spectra of several important molecules in the Earth's upper atmosphere [19].	18
Figure 1-3. Multiple quantum wells in between Sapphire substrates are THz-irradiated, while near-IR transmission spectrum is taken by the incident NIR laser probe from the top. The spectrum shows both the incident laser frequency f_{NIR} and the sidebands $f_s = f_{\text{NIR}} + nf_{\text{THz}}$, where $f_{\text{THz}} = 1.5$ THz. Insets show the schematics of the experimental setup (left) and the quantum well structure (right) [10].	18
Figure 1-4. Schematic presentation of various dynamical time scales in a general biological molecule. Collective modes of this heavy molecule fall into picosecond time scale (THz frequency) [20].	19
Figure 1-5. Demonstrations of a variety of THz applications in biomedical imaging (top left) [33], concealed weapon screening (top right, photo courtesy of ThruVision, UK), and chemical explosives detection (bottom) [34].	20
Figure 1-6. Schematics of typical one, two and three dimensional EM crystals. Two colors stand for either two dielectric materials with different refractive indices, or metal and dielectric. Periodical arrangements of them along one, two or three directions form corresponding EM crystals [4].	22
Figure 1-7. Schematics showing the formation of waveguide bend (left) and wave splitter (right) in a hexagonal-lattice 2-D EM crystal [40].	23
Figure 1-8. Performance of several THz continuous-wave sources [21].	26
Figure 2-1. Left: Schematic drawing of a woodpile EM crystal. Right: The first BZ of the WPS face-center-tetrahedron (fct) lattice, with apex of its irreducible BZ (characteristic k-points) marked.	41
Figure 2-2. Calculated band diagram of the silicon WPS. The 3-D complete band gap is indicated by the shaded region.	41
Figure 2-3. (a) Calculated photon density of states of the silicon woodpile structure, which has the filling ratio $w/d = 0.272$, and $D/d = 1.089$. The refractive index of the rods is $n = 3.40$ (silicon). The normalized frequency is given by $x = (a/c)f = d*f/c$. (b) Predicted radiation power intensities of the woodpile (solid) and the normal blackbody (dotted) at room temperature. (c) Thermal radiation power enhancement factor.	44
Figure 2-4. The real frequency DOS obtained using the HFSS eigen-solver (solid line) and the MPB (dashed line) for the silicon woodpile structure with the filling ratio $w/d = 0.272$, $D/d = 1.089$, and the rod periodicity $d = 646 \mu\text{m}$.	47
Figure 2-5. (a) Calculated photon DOS for the tungsten woodpile structure with the filling ratio $w/d = 0.272$, $D/d = 1.089$, and the periodicity $d = 646 \mu\text{m}$. (b) Thermal radiation power enhancement factor for this tungsten WPS.	49

LIST OF FIGURES - *Continued*

Figure 2-6. (a) A schematic drawing of the metallic micro-cavities. The dotted lines enclose one unit cell of the structure. (b) The predicted thermal radiation power enhancement factor assuming a 1% variation in the size of the micro-cavities.	54
Figure 2-7. Illustration of the fabrication process for a 9-unit cell silicon WPS [80] using saw blade dicing.	56
Figure 2-8. Left: THz-TDS experiment setup. Right: FIR-FTS block diagram.	57
Figure 2-9. Transmission responses (normal incidence) of the silicon WPS sample: (top) THz time-domain spectroscopy (TDS) measurement, (bottom) HFSS Simulation.	62
Figure 2-10. Silicon WPS transmittance: (a) FIR-FTS result (dash-dotted line with triangles, a.u.) compared with THz-TDS measurement (solid line, right ordinate) and HFSS simulation (dashed line with circles, left ordinate) results. (b)VNA measurement (solid line) compared with transfer-matrix-method (TMM) calculation (dashed line).....	63
Figure 2-11. Schematic of the Fourier transform spectrometer (FTS) setup for the direct thermal emission measurements.	65
Figure 2-12. Left: Image of the emission measurement setup in FTS sample chamber, showing the collimating mirror, the chopper, the sample stage and holder (Aperture not present). Right: Zoom-in image of the sample holder with silicon WPS sample mounted in the middle. The aluminum-made holder makes a good thermal bath, with thermal couple pinned on the top for temperature monitoring.	67
Figure 2-13. The thermal radiation differential spectra for the RAM (dashed) and the WPS (squares) samples at (a) 85°C and (b) 38°C. The error bars are based on statistics.	70
Figure 3-1. Illustration of the polymer-jetting process for 3-D objects prototyping.	81
Figure 3-2. Polymer slab THz characterization results. The real part of the permittivity ϵ' (open triangle) is plotted with left ordinate, and the loss tangent $\tan\delta$ (open rectangle) is plotted with right ordinate.	85
Figure 3-3. From left to right: artworks prototyped by Vero White, Vero Grey, and Vero Black polymers, respectively. Photo courtesy of Objet Inc.....	86
Figure 3-4. (a) Dielectric constants and (b) loss tangents of Vero Black, Grey, and White polymers, characterized by THz-TDS.....	87
Figure 3-5. Photographs of the fabricated polymer THz WPS. Inset is a zoomed-in view of the sample cross-section.	89
Figure 3-6. THz-TDS measured free space signal waveform (dashed) and the WPS sample transmitted waveform (solid). Inset shows the frequency domain signals of the sample (solid), the free space (dotted), and the experiment noise floor (dashed).	90
Figure 3-7. Comparison between the measured (open squares) and simulated (solid line) WPS normal-incidence power transmittances.	92
Figure 3-8. Schematics of the Johnson EBG structure, including: a 3-D model (left) showing one unit cell in the stacking direction and several periods in the horizontal direction (from [150]), the cross-sectional view (upper right), and the top view (lower right).....	94

LIST OF FIGURES - *Continued*

Figure 3-9. Photographs of the fabricated polymer Johnson EBG structure, including: the full view (left), the side (cross-sectional) view (upper right), and the top view (lower right). Clearly defined air hole and dielectric rod layers are observed.	95
Figure 3-10. Comparison between the measured (open squares) and simulated (solid line) Johnson structure normal-incidence power transmittances.	96
Figure 3-11. Photo of the photonic cavity array sample fabricated by THz rapid prototyping and then metalized via sputtering.	97
Figure 4-1. Band diagram of the complete EMXT structure and the defect waveguide modes. For the EMXT structure, dark (blue) regions denote the continuous modes region whereas in white regions no mode exists (band gaps). Inset (left) shows the schematic of the waveguide cross section when a center air core defect is introduced. Defect modes (waveguide modes) are marked by the dots (red) in the “Band Gap 1” region, among which the energy intensity profile of the fundamental HE_{11} mode is shown in the inset (right).	104
Figure 4-2. Simulated S-parameters of an 84 mm-long EMXT waveguide with lattice constant of 3 mm, center defect radius of 4.2 mm, and cladding air cylinder radius of 1.3 mm. The EMXT waveguide is fed by TE_{11} mode from circular PEC waveguide.	108
Figure 4-3. Power loss factors of the EMXT waveguide extracted from the wave-port (TE_{11} mode, circular PEC waveguide feeds) and the Gaussian beam (3 mm beam waist) incidence simulations.	110
Figure 4-4. Spectra of the waveguide power loss factor for various numbers of air cylinder cladding rings.	112
Figure 4-5. Spectra of the waveguide power loss factor for various waveguide lengths.	113
Figure 4-6. Spectra of the waveguide power loss factor for various defect core radii.	114
Figure 4-7. Spectra of the waveguide power loss factor for various defect core radii around 4.2 mm, with constant loss tangent used to describe material loss.	115
Figure 4-8. Spectra of the waveguide power loss factor for various material losses.	117
Figure 4-9. Linear fitting of the power loss factor (dB/mm) as a function of $\tan\delta$ at 113 GHz.	118
Figure 4-10. Cross-sectional and full views of a fabricated THz waveguide, with lattice constant of 3 mm, center core radius of 4.2 mm, and cladding air cylinder radius of 1.3 mm.	119
Figure 4-11. Setup of the characterization experiment: from left to right: THz transmitter, parabolic mirror 1, circular aperture, polymer lens 1, waveguide under test, polymer lens 2, parabolic mirror 2, and THz receiver.	121
Figure 4-12. (a) Transmitted waveforms of five waveguides with different lengths, and the reference scan transmitted through free space. (b) Normalized power transmission of the waveguides.	122

LIST OF FIGURES - *Continued*

Figure 4-13. (a) Semi-log plot of the measured transmitted power in dB versus waveguide length at 107 GHz. Linearly fitted slope gives the power loss factor at this frequency. (b) Measured and simulated waveguide power loss factor, both excited by Gaussian beam incidence.....	124
Figure 5-1. Left: Computer rendered image of the EMXT horn antenna. Right: Schematic drawing of the antenna defect shape, with four dimensions defining the horn antenna indicated.....	132
Figure 5-2. (a) EMXT antenna directivity at the boresight direction for various horn axial lengths, resulting a flare angle varying from 10.9° to 21.5°. (b) EMXT antenna radiation efficiency for various horn axial lengths.	133
Figure 5-3. Radiation efficiencies of EMXT horn antennas with various build material losses, and a circular horn antenna of exactly the same dimensions made by copper....	135
Figure 5-4. Return loss of the optimized EMXT horn antenna, with the material loss represented by $\sigma = 0.459$ Siemens/m.....	137
Figure 5-5. Radiation patterns of the EMXT and copper horn antenna at $\phi = 0^\circ$ cut plane with θ sweeping from 0 to 360 degree, at (a) 114 GHz and (b) 162 GHz..	138
Figure 5-6. Photos of the fabricated THz EMXT horn antenna, with $D = 16$ mm, $D_0 = 4.2$ mm, $L = 35$ mm, and $L_0 = 35$ mm.....	141
Figure 5-7. Schematic of the planned bench setup to measure the far-field radiation patterns of the EMXT horn antennas..	142
Figure 5-8. Schematics of the most commonly used circular waveguide-to-microstrip line transition. L_x is around quarter-wavelength long of the design frequency. The ground plane of the microstrip line on the back of the substrate connects with the ground of the circular waveguide [221].....	146
Figure 5-9. (a) Geometry and (b) E and H-field lines of the microstrip transmission line [166].....	148
Figure 5-10. Schematic of the EMXT waveguide-to-microstrip line transition design. Three zoomed-in insets demonstrate different sections of the transition structure..	151
Figure 5-11. Simulated S-parameters of a 60-mm long EMXT waveguide with 2.1 mm defect radius.....	152
Figure 5-12. Simulated S_{21} of the whole EMXT waveguide-to-microstrip line transition structure, including no-material-loss case, all-material-losses except the microstrip line section case, and all-material-losses case.....	154
Figure 5-13. Simulated S_{11} of the whole EMXT waveguide-to-microstrip line transition structure, including all the material losses.....	155
Figure 6-1. Integrated THz micro-system including various THz components. The system can be manufactured by the THz prototyping in a single fabrication.....	168

LIST OF TABLES

Table 2-1. Specification comparisons of THz-TDS, FIR-FTS and THz-VNA.	59
--	----

ABSTRACT

This dissertation presents the investigation of thermal radiation from three-dimensional electromagnetic crystals (EMXT), as well as the development of a THz rapid prototyping fabrication technique and its application in THz EMXT components and micro-system fabrication and integration. First, it is proposed that thermal radiation from a 3-D EMXT would be greatly enhanced at the band gap edge frequency due to the redistribution of photon density of states (DOS) within the crystal. A THz thermal radiator could thus be built upon a THz EMXT by utilizing the exceptional emission peak(s) around its band gap frequency. The thermal radiation enhancement effects of various THz EMXT including both silicon and tungsten woodpile structures (WPS) and cubic photonic cavity (CPC) array are explored. The DOS of all three structures are calculated, and their thermal radiation intensities are predicted using Planck's Equation. These calculations show that the DOS of the silicon and tungsten WPS can be enhanced by a factor of 11.8 around 364 GHz and 2.6 around 406 GHz respectively, in comparison to the normal blackbody radiation at same frequencies. An enhancement factor of more than 100 is obtained in calculation from the CPC array. A silicon WPS with a band gap around 200 GHz has been designed and fabricated. Thermal emissivity of the silicon WPS sample is measured with a control blackbody as reference. And enhancements of the emission from the WPS over the control blackbody are observed at several frequencies quite consistent with the theoretical predictions. Second, the practical challenge of THz EMXT

component and system fabrication is met by a THz rapid prototyping technique developed by us. Using this technique, the fabrications of several EMXTs with 3D electromagnetic band gaps in the 100-400 GHz range are demonstrated. Characterization of the samples via THz Time-domain Spectroscopy (THz-TDS) shows very good agreement with simulation, confirming the build accuracy of this prototyping approach. Third, an all-dielectric THz waveguide is designed, fabricated and characterized. The design is based on hollow-core EMXT waveguide, and the fabrication is implemented with the THz prototyping method. Characterization results of the waveguide power loss factor show good consistency with the simulation, and waveguide propagation loss as low as 0.03 dB/mm at 105 GHz is demonstrated. Several design parameters are also varied and their impacts on the waveguide performance investigated theoretically. Finally, a THz EMXT antenna based on expanding the defect radius of the EMXT waveguide to a horn shape is proposed and studied. The boresight directivity and main beam angular width of the optimized EMXT horn antenna is comparable with a copper horn antenna of the same dimensions at low frequencies, and much better than the copper horn at high frequencies. The EMXT antenna has been successfully fabricated via the same THz prototyping, and we believe this is the first time an EMXT antenna of this architecture is fabricated. Far-field measurement of the EMXT antenna radiation pattern is undergoing. Also, in order to integrate planar THz solid-state devices (especially source and detector) and THz samples under test with the potential THz micro-system fabricate-able by the prototyping approach, an EMXT waveguide-to-microstrip line

transition structure is designed. The structure uses tapered solid dielectric waveguides on both ends to transit THz energy from the EMXT waveguide defect onto the microstrip line. Simulation of the transition structure in a back-to-back configuration yields about -15 dB insertion loss mainly due to the dielectric material loss. The coupling and radiation loss of the transition structure is estimated to be -2.115 dB. The fabrication and characterization of the transition system is currently underway. With all the above THz components realized in the future, integrated THz micro-systems manufactured by the same prototyping technique will be achieved, with low cost, high quality, self-sufficiency, and great customizability.

CHAPTER 1. INTRODUCTION

Terahertz spectrum, as a region where electronics overlaps optics (Figure 1-1), includes frequencies between 100 GHz and 10 THz [1]. It has been one of the least tapped electromagnetic regions due to the paucity of technology especially sources and detectors. However it has enjoyed dramatic growth in terms of technical achievement as well as commercial implementation in recent years. Photonic crystal, or more generally to cover all frequencies, electromagnetic crystal, since being conceptually proposed in 1987 [2, 3], has been widely used in optical regime as a way to control the flow of light [4], and is continuing to find its applications in THz regime where manipulating photons is also demanded. In this chapter, a succinct introduction of terahertz technology and electromagnetic crystal, together with their existing / potential applications, will be presented. Research involving THz photonic crystals will be briefly reviewed as well. Then the motivation of this dissertation work will be discussed, followed by the dissertation organization.

1.1. Background

1.1.1. Terahertz Technology

The widely-acknowledged term “THz gap” well describes the insufficient exploration and development in terahertz spectrum when compared to its two neighbors, microwave and infrared/optics, as shown in Figure 1-1. Research in this

frequency range is hurdled mainly by the lack of efficient generation and detection of THz wave, as well as various components to manipulate the wave. It is therefore regarded as the final frontier of the electromagnetic spectrum. With the contributions from its two neighbor bands and the emerging of a wide range of new technologies, this gap has begun to be filled in the last decade.

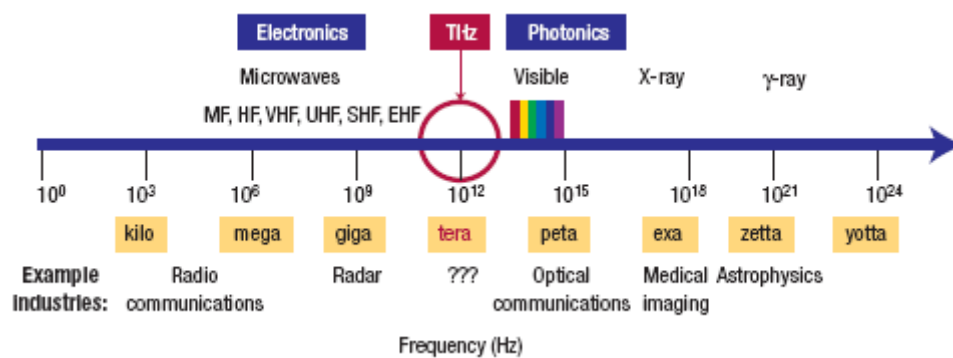


Figure 1-1. Schematic electromagnetic spectrum showing THz gap located in between electronics and photonics [5].

THz spectrum is a frequency range filled with a plethora of physical, chemical and biological sciences. Interstellar dust contains tens of thousands of THz spectral lines and these spectral signatures carry teeming information that is useful and important in interstellar and intragalactic sciences [6]. Due to the same richness of absorption lines, THz spectroscopy plays a vital role in planetary science and atmospheric monitoring [7, 8]. An example of the absorption spectra of several important molecules in the Earth's upper atmosphere can be seen in Figure. 1-2. Electrons in highly excited Rydberg atoms with $n = 20$ to 60 possess THz orbital frequencies. As interesting candidates for quantum information processing because of their rich states and good stability, Rydberg atoms can be manipulated by THz

radiation to demonstrate quantum database, quantum algorithms, and quantum chaos [9]. An exciton in quantum well is a bound electron-hole pair with a binding energy in the THz frequency range. Therefore a quantum well can be strongly pumped with THz radiation and the induced excitonic response can be observed [10]. Experiment shown in Figure 1-3 illustrates the feasibility of pumping quantum well strongly with THz illumination. Moreover, with exquisite design and control of the incident THz pulse waveform, coherent quantum control of carriers in semiconductor and their nanostructures can be achieved and lead to phenomena such as Rabi oscillations and photon echoes [11]. THz spectral region covers the rotational modes of light molecules, the low frequency collective modes and torsional modes of heavy molecules, and collective intermolecular modes of molecular clusters (Figure 1-4). Therefore dynamics of specific chemical and biological reactions involving these modes may be monitored and even controlled by THz spectroscopy [12, 13]. The exploration in this exciting area of basic science has just begun, and will enhance the understanding of molecules at the fundamental quantum mechanical level [14]. Examples include gas and liquid phase spectroscopy in chemistry [13, 15], and DNA folding spectroscopy [16] and solvent spectroscopy (especially water study) [17, 18] in biology.

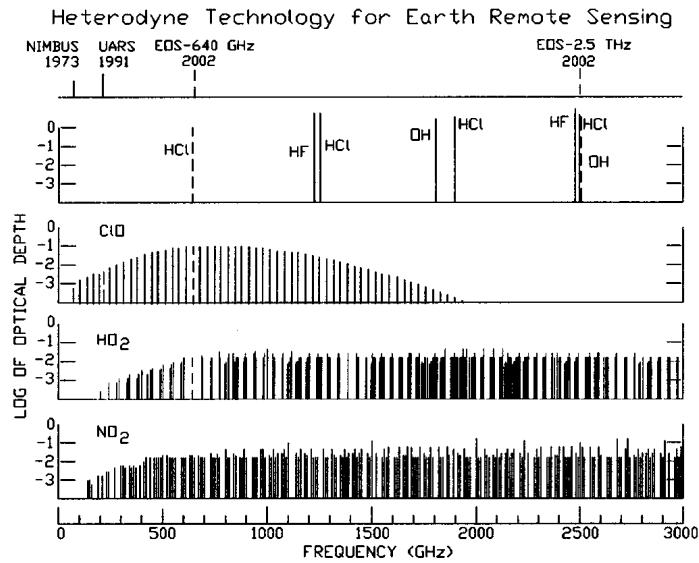


Figure 1-2. Spectra of several important molecules in the Earth's upper atmosphere [19].

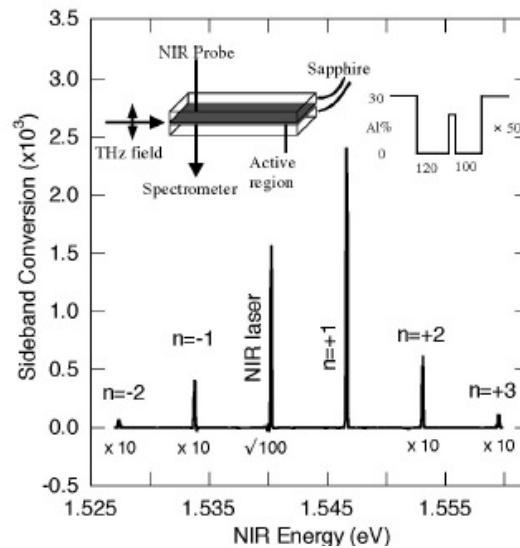


Figure 1-3. Multiple quantum wells in between Sapphire substrates are THz-irradiated, while near-IR transmission spectrum is taken by the incident NIR laser probe from the top. The spectrum shows both the incident laser frequency $f_{\text{NIR}} = 1.54 \text{ eV} = 373.84 \text{ THz}$ and the sidebands $f_s = f_{\text{NIR}} + n f_{\text{THz}}$, where $f_{\text{THz}} = 1.5 \text{ THz}$. Insets show the schematics of the experimental setup (left) and the quantum well structure (right) [10].

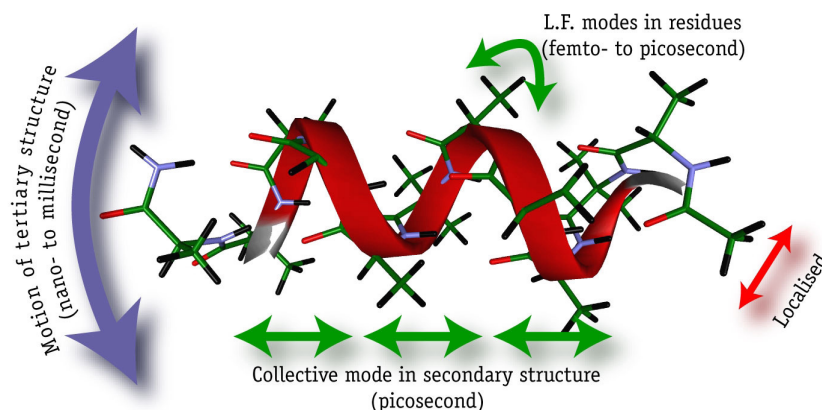


Figure 1-4. Schematic presentation of various dynamical time scales in a general biological molecule. Collective modes of this heavy molecule fall into picosecond time scale (THz frequency) [20].

Science always meets technology, and the terahertz regime is not an exception. A great deal of engineering potential in the THz field has been proposed; many have been realized and are becoming commercialized. To enumerate a few examples: the Terahertz frequency is the communication band of the next generation due to several advantages, including larger bandwidth and smaller antenna size than microwave frequencies, as well as less scattering loss (proportional to f^2 instead of f^4) and therefore much greater penetration depth through aerosols and clouds than IR and optical frequencies [21]; THz imaging, which benefits greatly from its tens to hundreds of micrometer resolution and capability to penetrate through many low-loss dielectric materials such as wood, foam, paper, clothing and cardboard, has taken a very advantageous position in biological and medical imaging [22, 23], electronic chips and medicine pills quality control [24, 25], package scanning [26] and airport security screening [27], and leak and concealed object detection [28, 29]; Richness of molecular spectral signatures makes THz frequency very suitable for chemical,

biological agent, and explosive detection [30-32], as well as standoff sensing [8] and atmosphere monitoring such as O-zone depletion [7]. Figure 1-5 demonstrates several of these THz engineering potentials: on the top left, a terahertz image of a human tooth reveals the cavity inside, which is not exposed by optical image; on the top right, a hidden hand-gun underneath a person's clothes is screened by THz reflective imaging; and the bottom plot shows a strong absorption signature around 800 GHz from various commonly used explosives, therefore detection of them at that frequency could be rather sensitive.

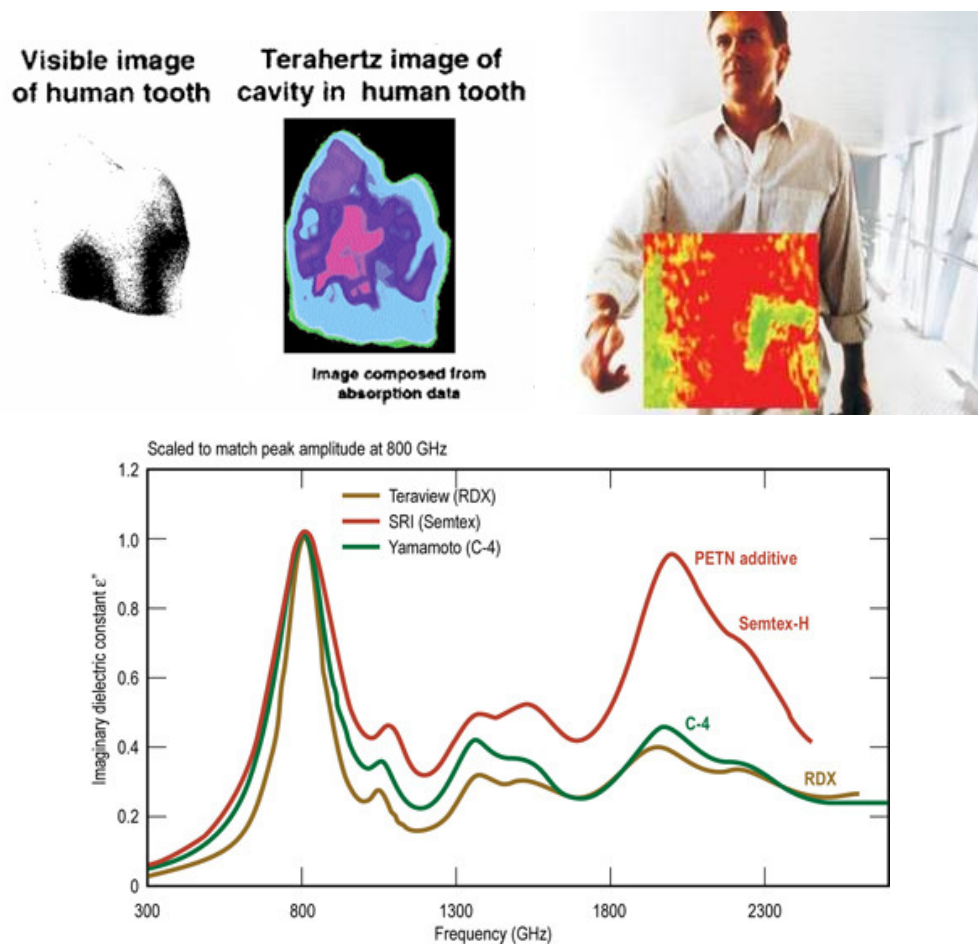


Figure 1-5. Demonstrations of a variety of THz applications in biomedical imaging (top left) [33], concealed weapon screening (top right, photo courtesy of ThruVision, UK), and chemical explosives detection (bottom) [34].

1.1.2. Electromagnetic Crystal Background and Application at THz

The term “photonic crystal” is more strictly associated with infrared and optical frequencies, while the terms electromagnetic (EM) crystal and electromagnetic band gap (EBG) structure are more general and cover all frequencies, including the THz range. They refer to the same behavior because of the physical equivalence between electromagnetic waves and photon modes. This dissertation will choose to use both of the more general terms, EM crystal (EMXT) and EBG structure.

The invention of the electromagnetic crystal was inspired by electrons in a semiconductor. Semiconductor crystals pose periodic potentials on electrons within them, therefore electrons have to fall into certain energy bands when traveling in them. Between the energy bands, band gaps form and electron propagation is forbidden. Equivalently, EM crystals pose periodic potentials for photons and exhibit band gaps in which electromagnetic waves can not propagate. Naturally occurring EM crystals exist, for example, the gemstone opal and many biological objects like butterfly wings and the surface ornamentation of crabs [35]. In order to engineer EM bands and band gaps, artificial EM crystals are a prerequisite. The solution is to arrange dielectric and / or metallic objects periodically, following various lattice formations such as square and hexagonal lattices in two dimensions, and face-centered-cubic (fcc) and body-centered-cubic (bcc) lattices in three dimensions. Bragg diffractions among these periodically arranged scatters make scattered electromagnetic waves interfere constructively or destructively at specific frequencies and along specific directions.

Therefore, an EMXT can exhibit EM bands and band gaps. Figure 1-6 below depicts the formation of typical one, two and three dimensional EM crystals.

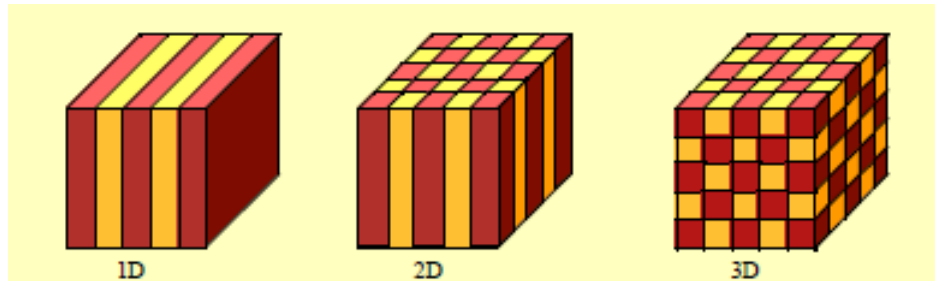


Figure 1-6. Schematics of typical one, two and three dimensional EM crystals. Two colors stand for either two dielectric materials with different refractive indices, or metal and dielectric. Periodical arrangements of them along one, two or three directions form corresponding EM crystals [4].

In virtue of their band structures, EM crystals lead to various functionalities to manipulate EM waves and thus interesting applications. EM crystals are readily transmission filters and perfect reflectors at the band gap frequencies; therefore, they find applications in frequency selection [36, 37], substrate mode suppression [37], and Bragg reflective mirror [38]. Similar to adding donors or acceptors into semiconductors, introducing defects into the EM crystal perturbs the periodic potential locally and makes defect modes emerge at the band gap frequency. A closed-space defect would result in a microcavity with very high quality factor [39]; A line defect forms a wave guiding channel and supports wave propagation along the defect [4, 40]; By controlling the shape of the line defect and combining it with a cavity defect, an EBG waveguide bend [41], wave splitter [40], or channel drop filter [42, 43] can be achieved, as shown in Figure 1-7. Since the dispersion properties of

the EM crystal is quite engineer-able via adjustments of pitch, lattice type, scatter shape, filling factor, and index contrast, its group velocity $v_g = \nabla_k \omega(k)$ could be either minimized to suit itself as an optical delay line [44], or diversified to make the EM crystal a superprism [45] or beam router [46]. Along with the same engineering of the structure's dispersion curve, metamaterials with negative refraction may be built with EM crystals [40, 47]. This property opens up new applications such as superlens [48] and sub-wavelength imaging [49]. If active materials like photoemissive III-V semiconductors or organic materials are introduced into the microcavity defect aforementioned, a laser can be built [50]. Given a small enough defect, photons can be localized into extremely small volume and the device can be used to study cavity quantum electrodynamics (QED) phenomena [51]. Last but not least, an EM crystal was first proposed to inhibit the spontaneous emission in a material [2], which makes thermal emission directly from EM crystal a rather interesting topic to explore [52- 54].

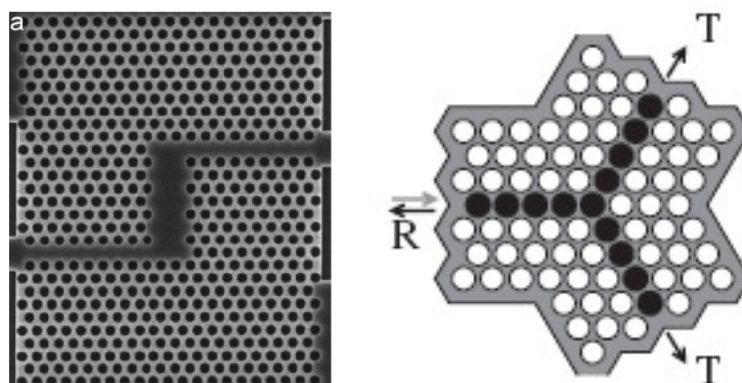


Figure 1-7. Schematics showing the formation of waveguide bend (left) and wave splitter (right) in a hexagonal-lattice 2-D EM crystal [40].

The marriage between THz and EM crystals is quite natural. To fully appreciate the potential of THz waves, components and techniques with appropriate photon functions to manipulate these waves are highly desired. Since Maxwell's equations are wavelength scalable, many of the EM crystal related techniques and applications could be readily employed at THz frequencies. On the other hand, THz suits itself in EM crystal research with its own advantageous features and instruments as well. Unlike EM crystal fabrications at optical wavelength, which intrinsically require complicated photolithography, laser milling or chemical self-organization processes [40, 55] and leaves quite some defects and mal-constructions in the sample, micrometer-scale THz wavelength determines that fabrication of a THz EM crystal could be in principle much more precise and defect-free with micromachining technologies. This leads to much more uniform and better prepared EM crystal samples. With techniques and equipments adopted from the microwave regime and application of photon-mixing sources, a millimeter-wave and THz network analyzer has been invented and allows simultaneous measurements of both transmitted and reflected signals from the sample. Therefore, the EM crystal under test can be fully characterized in one simple setup and measurement, which would be hard to achieve in a conventional optical setup. Also, the invention of the Auston switch [56] enabled THz time domain spectroscopy (THz-TDS) of an EM crystal. Therefore, not only the intensity but also the phase responses of the sample could be explored after Fourier transforming to frequency domain. The application of an ultrafast pulse to a sample in

a THz-TDS system characterizes it over a broadband frequency range as well, in contrast to many narrow-band experiments done at optical frequencies.

The introduction of an EM crystal into the THz region was first motivated by THz wave guiding in spectroscopy applications [21]. Free space THz propagation devices can be bulky, expensive and inflexible for many applications, for example, a sample under study may not always be accessible by a free space beam. Conventional waveguides have limitations on THz beam guiding due to their high loss, high dispersion and difficulties in fabrication, which results in severe THz pulse reshaping and attenuation problems [57]. THz waveguides based on EBG structures are able to guide THz beam efficiently with advantages of better confinement, smaller spot size, low dispersion and low loss. Continuous efforts have been paid on EBG-based THz components, among them, sources, detectors, filters, and waveguides [21, 37, 54]. However, the realization of THz EBG components still faces some challenging issues including efficient design and fabrication processes and accurate characterization methods, which become some of the motivations of this dissertation work.

1.2. Motivation

Optics and electronics converge in the THz gap, and are currently filling the gap with a variety of technologies and scientific instrumentations inherited and modified from their respective regimes. The THz field is experiencing tremendous technical advancement in recent years, and the most significant progress has been the

development of various THz sources. Nowadays, several options exist if a continuous-wave (CW) source of narrow band THz radiation is desired, including microwave frequency upconverters [58, 59], backward wave oscillators [60, 61], photocurrent based photomixers [62, 63], nonlinear optical crystal based photomixers [64, 65], CO₂ laser-pumped molecular gas lasers [66, 67], THz quantum cascade lasers [68, 69], resonant tunneling diodes (RTDs) and GaAs Schottky diodes [67, 70], and more. A comparison of the output power levels of various THz CW sources can be found in Figure 1-8. If a broadband THz source is to be pursued; the main options would be ultrafast laser excited photoconductive antennas [56] and electro-optical (EO) crystal optical rectifiers [71]. Major free-electron-laser (FEL) facilities including SLAC, UCSB-FEL, BNL-FEL, FELIX in the Netherlands, and FELBE in Germany would provide high field intensity narrow-band or broadband THz radiation for nonlinear and non-equilibrium researches.

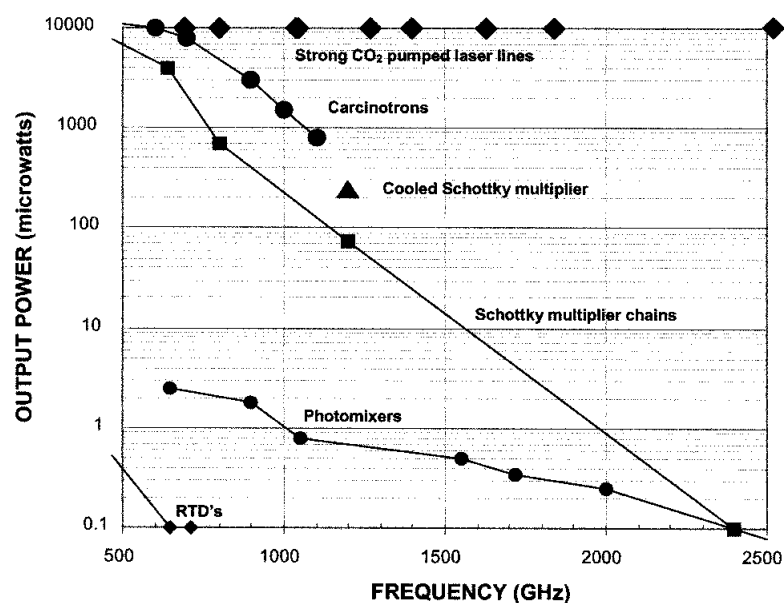


Figure 1-8. Performance of several THz continuous-wave sources [21].

However, all these THz sources are hampered by various limitations. Tube sources are usually cumbersome, require extremely high electric and magnetic fields and high current density, and have reliability and life time issues [60]. Infrared-pumped laser sources are also bulky and expensive, and have a limited frequency tuning range [72]. Electronic solid-state sources suffer from reactive parasitics, and the transit time of the carriers causes high frequency roll-offs [21]. Moreover, optical type sources, such as solid-state lasers, are not suitable for THz frequencies due to the comparable photon and dissipative lattice phonon energies [21]. A quantum cascade THz laser requires expensive cryogenics to operate [21]. Both of the frequency up-and-down conversion approaches have been proven to be extremely inefficient [73, 74]. Diode sources and photoconductive antennas fall into the low-power regions [21, 56, 67]. Although compact table-top electron accelerators are being developed, most researchers and users do not have access to FEL THz sources. All the above limitations led to our group's motivation to develop a compact, efficient, low-cost, and easily driven THz source. Blackbody radiation may be a good candidate under these criteria, however Planck's Law [75] determines that the blackbody radiation power level at THz frequencies is tiny even at very high temperatures. Modification of the spontaneous emission from a thermally or electrically pumped blackbody is therefore necessary to enhance its thermal radiation at THz frequencies. EM crystals, as initially proposed to inhibit spontaneous radiation, may very well fulfill the mission. Photon density of states, as a primary quantity in Planck's Law to

decide the irradiance, is greatly enhanced at the band edge frequency of an EBG structure due to the anti-crossing effect on its dispersion curve. Therefore, enhanced thermal radiation from an EM crystal may appear at the EBG band edge frequencies and may make it a good THz thermal source. Whether direct thermal emission from an EM crystal can exceed normal blackbody levels is also a long-time controversial question in the optical regime [52, 53, 76, 77]. To answer this question experimentally became one motivation to conduct this research work as well.

Besides sources, a second paucity of THz resources has been the THz component building blocks, such as guiding structures, filters and reflectors, antennas, transition to planar circuits, quasi-optics, and basic terahertz materials [21]. Conventional realization of these components relies on metals, whose conduction losses heavily depends on the metal surface smoothness and their manufacture involves complicated metal micromachining processes [78, 79]. EM crystals can be constructed with all-dielectrics, therefore components based on EBG structures could circumvent these issues. Endeavors has been put into this research field, however one of the most challenging issues is still how to fabricate THz EBG components with arbitrary shape accurately. Since the feature dimensions of THz EBG components fall in a transition region between the conventional micromachining techniques used for microwave applications and the micro/nano-fabrication methods in use at optical frequencies [80], none of the two methods fits THz EBG component fabrication very well. Several semiconductor fabrication approaches, including dicing saw machining [81], wet etching [82], deep reactive ion etching (DRIE) [83], deep X-ray lithography

[84], laser micromachining [80, 84], hot-drawn and chemical vapor deposition (CVD) processes [85-88] and even hand assembly [86, 89] have been reported. These methods are mostly complicated, expensive, and not mass-productive. Extraordinary care is required to achieve even relatively uniform THz EBG geometries using these fabrication techniques, let alone the more complicated structures such as defect cavities and wave splitters.

In order to fabricate arbitrary THz EBG shapes easily and enable mass production, a rapid prototyping technique of these structures alike the existing techniques in microwave EBG fabrication [90-93] needs to be developed. These existing methods include polymer and ceramic stereolithography [90, 91], fused deposition modeling [92] and selective laser sintering [92]. However, these methods have only been successful at frequencies up to approximately 30 GHz. To extend the rapid prototyping technique to THz frequencies is therefore very necessary. Post processing of the prototyped EBG component templates, including metallization and depositing silicon onto other dielectric materials, already exists [94-97]. Therefore, THz EBG components with high-and-low index contrasts or metal terminations at places are achievable. More importantly, THz prototyping would allow systematic integration of multiple components of different kinds from the very first point they are fabricated. Imagine a THz antenna array or a quasi-optics/waveguide system fabricated in one single prototyping, saving all the troubles of mounting and aligning. All these prospects make THz rapid prototyping highly desirable.

1.3. Dissertation Organization

The work presented in this dissertation will discuss the investigation of thermal radiation from electromagnetic crystals, as well as a three-dimensional THz rapid prototyping technique and its application to THz EBG components and to micro-system fabrication and integration. The dissertation is organized as follows.

Chapter 2 presents the theoretical calculation and experimental measurement of thermal radiation from three-dimensional THz EM crystals. Three THz EMXTs with infinite lattices are investigated, namely a silicon woodpile structure, a tungsten woodpile structure and a photonic cavity array. Their photon density of states (DOS) are calculated via an eigen-mode calculation and a K-space interpolation algorithm. Their respective thermal radiation behaviors are then calculated based on the DOS results and Planck's equation. Fabrication and characterization of the silicon woodpile structure are then presented, together with a discussion of three commonly used THz characterization instruments. Thermal radiation measurements have been carried out via a Fourier transform spectrometer (FTS) in emission measurement setup. Results show that the silicon woodpile structure exhibits a good agreement between its calculated and measured thermal emissivity.

Chapter 3 reports a THz rapid prototyping technique developed in our group using a commercially available 3-D printing machine based on polymer jetting. Basically any arbitrary 3-D shape can be printed out in a layer-by-layer manner with this technique, and the spatial printing resolution is comparable with THz wavelength scale, thus enabling features at THz frequencies. Two THz EMXT structures that are

hard to fabricate via common fabrication methods are produced with this technique. Characterization shows excellent agreement between simulations and measurements. Therefore the great accuracy and flexibility of this THz rapid prototyping method are demonstrated.

Chapter 4 presents further application of the THz rapid prototyping method to fabricate important THz waveguide structures. A hollow-core EMXT defect based THz waveguide is proposed and studied. A series of parametric simulations are conducted to explore the impacts of various design variables on the waveguide propagation loss performance. The waveguide is fabricated by the rapid prototyping method reported in Chapter 3. Waveguides of various lengths and identical cross-sections are printed and their THz transmittance characterized. The intrinsic propagation loss factor of the waveguide is extracted via a semi-log linear fitting algorithm. The measured loss factor again matches with the simulation results pretty well. The building block of a THz guiding structure is thus achieved through the successful demonstration of this THz EMXT waveguide.

Chapter 5 is a more theoretical section introducing proposals to extend the THz waveguide to an EMXT THz antenna and the transition of a THz wave from the waveguide to a planar transmission-line circuit. With these two components THz waves can be coupled from a free-space radiation system (such as THz-TDS) into the waveguide or onto THz planar circuits, which may lead to compact THz micro-systems. Simply by flaring the straight waveguide structure outwards, a THz EMXT circular horn antenna forms. Simulation shows good far-field radiation

patterns and reasonable antenna gain and efficiency when compared to a similar circular horn antenna made of copper. This antenna could be employed to couple free-space THz radiation from the THz-TDS into a straight waveguide efficiently, whereas on the waveguide end a transition to a THz microstrip line is also proposed. The transition is done by leading the THz wave within the waveguide channel onto a dielectric rod waveguide of square shape cross-section. This dielectric rod is then eventually tapered down to the size of the microstrip trace line, along the wave propagation direction. Therefore the electric field in the rod gets concentrated and profile-matched to the transmission line mode. Simulation shows low return loss, coupling loss and radiation loss associated with this transition design. Currently realization and characterization of both proposed THz components are underway.

Finally, Chapter 6 holds a discussion about the conclusions and future works.

CHAPTER 2. THERMAL RADIATION FROM 3-D THz EMXT

Thermal radiation in the THz range only occupies a tiny portion of the entire blackbody power spectrum at room temperature. In this chapter, it is demonstrated that a thermal radiator constructed from an EM crystal can be designed so that its photon density of states (DOS) is enhanced in the THz frequency range. As a consequence, this source may lead to large enhancements of the radiated power over the values associated with normal blackbody radiation at those frequencies. The THz thermal radiation enhancement effects of various EM crystals, including both silicon and tungsten woodpile structures and a cubic photonic cavity (CPC) array, are explored. The DOS of the woodpile structures and the CPC array are calculated, and their thermal radiation intensities are predicted numerically. These simulations show that their DOS can be enhanced by a factor of 11.8 around 364 GHz and 2.6 around 406 GHz, respectively, for the silicon and tungsten woodpile structures in comparison to the normal blackbody radiation values at these frequencies. It is also shown that an enhancement factor of more than 100 may be obtained by using the CPC array. A silicon woodpile EM crystal with a band gap around 200 GHz has been designed and fabricated. The transmission property of this woodpile structure is characterized via various THz instruments, including THz time-domain spectrometer (TDS), Fourier transform spectrometer (FTS), and THz network analyzer (TNA). A brief comparison of these three characterization instruments is given as well. Thermal emissions from the fabricated silicon woodpile and a control blackbody sample are measured.

Enhancements of thermal radiation from the EBG source over the control blackbody are observed at several frequencies quite consistent with the theoretical predictions.

2.1 Motivation and Theoretical Principles

2.1.1 Motivation

The Terahertz portion of the frequency spectrum is currently underutilized and is very important for many applications in the near future, including remote sensing, imaging, screening and communications [21]. THz frequencies combine some of the advantages of both the microwave and infrared (IR) spectra, i.e., they provide coverage in IR-blind conditions while offering more bandwidth and spatial resolution than is available with microwave frequencies. Together with technical advancement and application enthusiasms, THz technology has experienced a renaissance over the past few years. While continuing to make major strides in sub-millimeter wave astronomy and remote sensing, THz technology is blooming with potential applications in contraband detection, tumor recognition, DNA sequencing, tissue imaging, radar and communications [21-23, 98-102]. However, the availability of THz sources remains one of the major bottlenecks in the realization of the promises of THz technology for many of these exciting applications. Conventional tube sources are cumbersome, require high-voltage power supplies, necessitate high internal electric and magnetic field intensities, and have reliability and life time issues [60]. Conventional IR pumped laser sources are also bulky, have a limited tuning range,

and are expensive [72]. Traditional electronic solid-state sources suffer from reactive parasitics, and the transit time of the carriers causes high frequency roll-offs [21]. Moreover, optical type sources, such as solid-state lasers, are not suitable for THz frequencies due to the comparable photon and lattice phonon energies [21]. Quantum cascade laser is a promising instrument to generate THz wave, however its operation requires expensive cryogenics. One of the most popular methods currently used for generating THz power is frequency conversion: either up-conversion from millimeter wavelengths by frequency multipliers made of nonlinear capacitors such as heterostructure barrier varactor (HBV) diodes and planar Schottky diodes [73, 74, 103], or down-conversion from optical or IR frequencies through laser heterodyning or photo-mixing [62]. Both of these frequency conversion approaches have been proven to be inefficient. In this chapter, a potential THz source based upon thermal radiation enhancement enabled by electromagnetic crystals is proposed. Preliminary theoretical and experimental results are reported and give promising indications that a new type of thermal THz source may be realized using carefully designed EM crystal thermal radiators.

The inspiration for this THz source concept comes from a well known idea that a three-dimensional EM crystal can drastically modify the spontaneous emission spectra from an atomic or a semiconductor material via the redistribution of the photon density of states (DOS) in different frequency ranges. Within the EBG of an EM crystal, spontaneous emission is completely forbidden because there is no photon state in that frequency range that can couple with an atomic transition, yielding a zero

photon DOS. Outside the EBG, the emission rate is directly correlated with the photon DOS [52]. The existence of an EBG will result in a shift of the emission energy from the forbidden frequency range to adjacent EM band-pass frequency ranges. This in turn causes an enhanced DOS to emerge and hence an enhanced emission rate at those frequencies. This phenomenon is often known as the "anti-crossing" effect on the dispersion curve near the band gap edge. To the first order (assuming ideal coupling to the external environment), thermal radiation emitted by an object has a linear relationship with its photon DOS [52]. Consequently, a thermal radiation enhancement may be expected in a frequency range where the photon DOS is much higher than that of a normal black body. This phenomenon has been explored both theoretically and experimentally [52, 76, 104, 105]. For example, both passive experiments using one-dimensional or three-dimensional EM crystals as filters [106, 107], and active experiments using EM crystals directly as a radiation source [77, 108], have been reported. Possible interpretations of the underlying physics of the thermal radiation enhancement, and direct calculations based on these interpretations [76, 105, 109-111] have been reported as well. Some controversy still remains with these results [112]. However, while previous work focused mainly on IR and optical wavelengths, the goal in this chapter is to explore the phenomenon in the THz frequency range, build a potential THz thermal radiation source with tunable operation frequency by tuning the band gap frequency, and understand the physics within EMXT thermal radiation better.

2.1.2 Theoretical Principles

Artificially engineered EM crystals consist of periodic dielectric and/or metallic structures. Because of their periodicity, these structures have unique electromagnetic properties, such as the existence of band gaps and a photon density-of-states (DOS), which are analogous to semiconductor energy band gaps and the electron DOS. Since the physics of an EM crystal is highly scalable in frequency, EBG based devices have already shown promise as effective methods for controlling and manipulating wave propagation for both microwave and optical frequencies [113]. Lately, more attention has been devoted to EBG based devices in the THz regime [114] due to the increased scientific and engineering interests [115] in THz sensing, imaging, and communication areas. Besides controlling and manipulating the propagation of EM waves through wave-EM crystal interactions, EBG structures can also be used to alter and tailor EM processes such as the emission and detection of EM radiation. For example, spontaneous emission may be inhibited [2] or enhanced. The possibility of designing EBG structures to manipulate the final states of electromagnetic processes may have significant implications in many physical, chemical, and biological processes in nature.

Blackbody radiation has been a subject of interest since the beginning of the past century due to Planck [75]. The thermal power radiated by a normal blackbody at temperature T (degrees Kelvin) within the frequency range f to $(f + df)$ (Hz) per unit volume is well defined by the free space Planck's equation:

$$u(f)df = \rho(f) \cdot \frac{hf}{e^{hf/kT} - 1} \cdot df = \frac{8\pi f^2}{c^3} \cdot \frac{hf}{e^{hf/kT} - 1} \cdot df \quad (2.1),$$

where $\rho(f)$ is the photon density of states, $h = 6.626 \times 10^{-34} \text{ m}^2\text{kg/s}$ is the Planck constant, hf is the individual photon energy, $k = 1.381 \times 10^{-23} \text{ J/K}$ is the Boltzmann constant, and the term $1/[\exp(hf/kT)-1]$ is the Bose-Einstein distribution representing the photon statistics. At room temperature, Equation (2.1) predicts that the blackbody radiation peak will occur at an IR frequency (9.75 micron), while the radiated power in the THz range will occupy only a tiny portion of the entire blackbody power spectrum. However, it is conceivable that the Planck distribution could be modified if the emitting object is an EM crystal and its photon DOS is different than the one typically associated with a normal blackbody object. In Equation (2.1), all quantities are fixed except the overall photon DOS $\rho(f)$. To modify the thermal radiation of an object, a nontrivial redistribution of the DOS is required. Thus, the idea of modifying the normal blackbody DOS with a three-dimensional (3D) EM crystal arises naturally, following the general rule of thumb that the presence of a complete EBG usually means a drastic redistribution of the photon DOS into different frequency regions [52].

A passive approach to modify spontaneous emission is to use the EM crystal as a filter, i.e., the source emission spectrum is reshaped corresponding to the pass/stop band characteristics of the EM crystal [107]. On the other hand, spontaneous emission directly from atoms in the EM crystal itself, i.e., the EM crystal is the active emission source, is yet another approach. Previous theoretical [52] and experimental [116] work have indicated that the thermal emission from an EBG structure could indeed be different than the Planck distribution and, in certain frequency bands, the

output intensity could be higher than that emitted by a normal blackbody. In some experiments [112, 116], a controversial effect that seemingly violates the second law of thermodynamics was reported. For example, the levels of thermal emission from a tungsten woodpile structure (WPS) were shown to exceed its absorption dramatically. This behavior contradicts the Kirchoff's law, i.e., for an object in thermal equilibrium, its thermal emission at any frequency should not exceed the value defined by the Planck curve [110-112]. The explanation for this contradiction was that the WPS may not be in thermal equilibrium [117]. Several other theoretical works have confirmed that enhanced thermal emission would occur when the EM crystal is not in thermal equilibrium [76, 105]. In summary, there have been a series of experimental studies on thermal emission from metallic WPSs; and their results are not all consistent [53, 76, 77, 116, 118, 119]. The key controversy is whether the metallic WPS emission enhancement over the blackbody values has actually been observed experimentally [53, 76, 116] or not [77, 118, 119]. Nonetheless, the focus of all previous work has been in the near-IR regime and has targeted light source applications. This investigation of thermal emission from an EBG structure in the THz regime contributes to the understanding of the fundamental properties of EM crystals and may lead to useful THz applications.

2.2 THz EMXT Thermal Emissivity Calculations

Three structures are commonly known to have complete 3-D EBGs: inverse-opal, diamond and woodpile structures. The WPS (also named the Lincoln-Log structure [76] because its relatively simple geometry is similar to structures attainable with Lincoln-Log building toy sets) is selected for our study here. A drawing of a WPS is shown in Figure 2-1, left [120]; it consists of a unit cell containing 4 layers of infinitely long silicon square rods stacked with a periodicity D . Within the unit cell, the rods in each layer are distributed with the same periodicity d ; and the adjacent layers that have the same rod orientation are shifted with respect to each other by $d/2$. Each rod has a height $h = D/4$ and a width $w = h$. Thus, the filling ratio of the rods with respect to the whole structure is equal to w/d . This EM crystal can be treated as a face-centered-tetragonal (*fcc*) or a simple tetragonal (*st*) lattice. In this case, the simple tetragonal lattice whose unit cell contains four attached rods with periodicity d in the $\langle 110 \rangle$ and $\langle \bar{1}\bar{1}0 \rangle$ lattice directions and periodicity D in the $\langle 001 \rangle$ stacking direction (see Figure 2-1) is considered. The center frequency of the WPS band gap is scalable by its lattice parameters. By varying the WPS filling ratio, its band gap width can also be adjusted.

2.2.1 Woodpile EM Crystals

2.2.1.1 Silicon Woodpile Structure

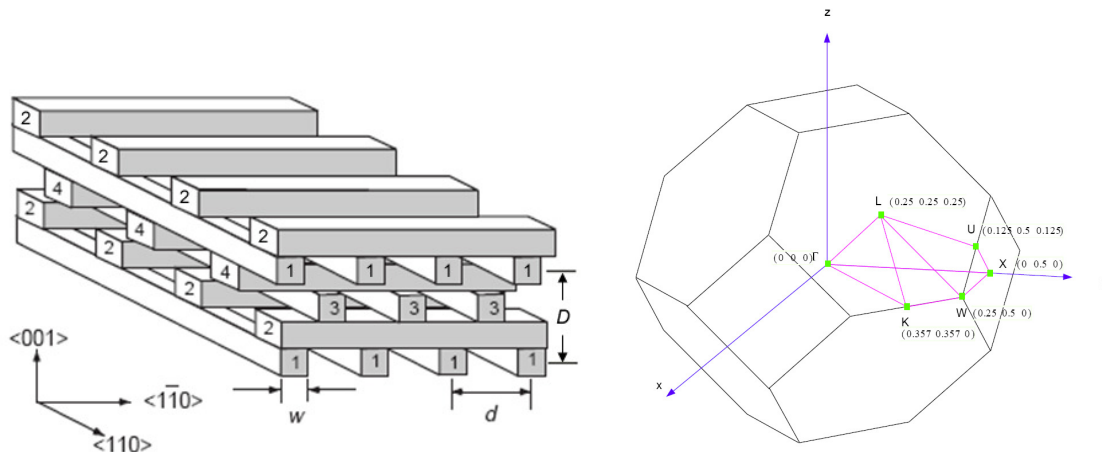


Figure 2-1. Left: Schematic drawing of a woodpile EM crystal. Right: The first BZ of the WPS face-center-tetrahedron (fct) lattice, with apex of its irreducible BZ (characteristic k-points) marked.

The photon DOS of a silicon (refractive index 3.4) WPS designed with $w/d = 0.272$ and $D/d = 1.089$ is obtained by determining the eigen-modes of the WPS within the irreducible Brillouin zone of its reciprocal lattice (Figure 2-1, right). The computation code MIT MPB [121] is used for the calculation of the eigen-modes. Figure 2-2 shows the calculated band diagram (or dispersion relation) of the above silicon WPS design. A 3-D complete band gap region where no eigen-modes exist is obtained and marked as the blue shaded area.

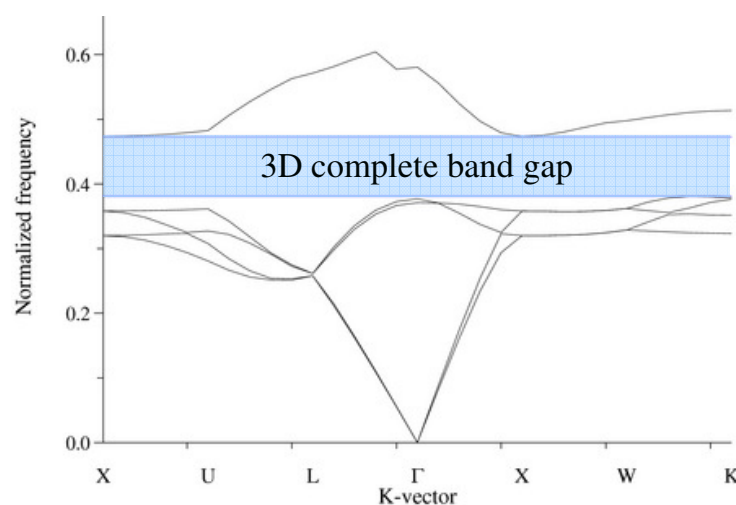


Figure 2-2. Calculated band diagram of the silicon WPS. The 3-D complete band gap is indicated by the shaded region.

The DOS is then generated with a numerical interpolation method in the reciprocal lattice space [122, 123], which is based on all of the eigen-mode frequencies obtained as the k-points sweep the irreducible Brillouin zone. The calculation results are plotted in Figure 2-3. Notice that the abscissa of Figure 2-3(a) is the normalized frequency x , which is related to the absolute frequency as $x = (a/c)f = d \cdot f/c$, where c is the speed of light in vacuum, and $a = d$ is the st -lattice constant. Therefore, a simple scaling of d can fit the response of the whole structure into any frequency band of practical interest. The ordinate is the photon DOS $\rho(x)$ at the normalized frequency x . The transformation from the DOS at the normalized frequency, $\rho(x)$, to the DOS at the real frequency, $\rho(f)$, is given by the relation: $\rho(f) = \rho(x)(1/ca^2)$. The thermal radiation power per unit surface area per unit frequency $j(f)$ is,

$$j(f) = \int_0^{2\pi} d\varphi \int_0^{\pi/2} d\theta \cdot \frac{c}{4\pi} u(f) \cos\theta \sin\theta = u(f) \cdot c/4 \quad (2.2)$$

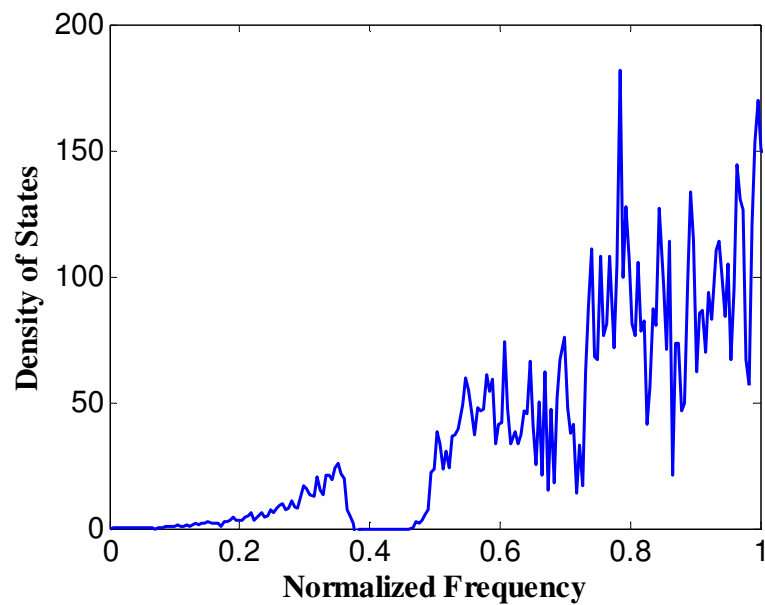
Using the expression of $u(f)$ in Equation 2.1 and the relation between $\rho(f)$ and $\rho(x)$, $j(f)$ is explicitly given by the expression

$$j(f) = \frac{hcf \rho(f)}{4(e^{hf/kT} - 1)} = \frac{hcx\rho(x)}{4a^3(e^{hcx/akT} - 1)} \quad (2.3)$$

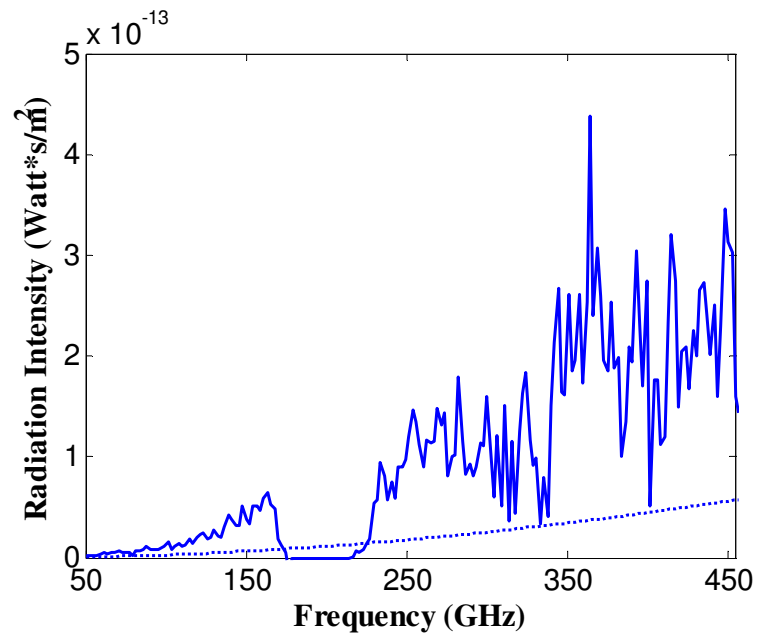
The corresponding formula that is used to calculate the radiation power density of a normal blackbody is

$$j_0(f) = \frac{2\pi hf^3}{c^2(e^{hf/kT} - 1)} = \frac{2\pi hcx^3}{a^3(e^{hcx/akT} - 1)} \quad (2.4)$$

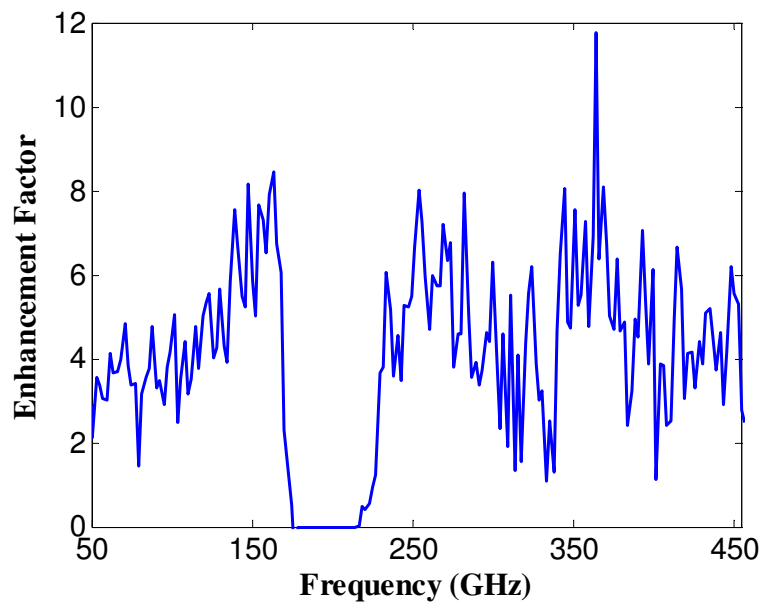
The computed j for the silicon WPS having the rod periodicity $d = 646 \mu\text{m}$ and the computed j_0 for room temperature are plotted in Figure 2-3(b) versus the real frequency. The center of the band gap is determined to be 195 GHz. With these calculations, an enhancement factor of j/j_0 can be defined. This thermal emission power enhancement factor for the silicon WPS is plotted in Figure 2-3(c). Those results illustrate how the silicon woodpile EM crystal may greatly modify the thermal power emitted within a specific portion of the THz frequency range.



(a)



(b)



(c)

Figure 2-3. (a) Calculated photon density of states of the silicon woodpile structure, which has the filling ratio $w/d = 0.272$, and $D/d = 1.089$. The refractive index of the rods is $n = 3.40$ (silicon). The normalized frequency is given by $x = (a/c) f = d \cdot f / c$. (b) Predicted radiation power intensities of the woodpile (solid) and the normal blackbody (dotted) at room temperature. (c) Thermal radiation power enhancement factor.

The plots in Figure 2-3 explicitly show a complete band gap from around 175 GHz to 216 GHz, i.e., there is no thermal energy radiated in that frequency band. The photon DOS gaps, peaks, and consequently the modified thermal radiation power at these frequencies originate from Bragg diffractions in between the EM crystal lattice points. For example, the DOS peaks can be regarded as the Bragg diffraction resonances. In particular, there are several thermal radiation power enhancement peaks observed, for example, around 148, 163, 254, 283, 364, 393, 415 and 448 GHz. The power enhancement factor is as high as 11.8 at the 364 GHz peak, which means there is more than 1080% power output increase at 364 GHz over the normal blackbody value.

To verify the accuracy of these numerical results, an alternative method is developed to calculate the WPS eigen-modes. In particular, we used the commercial 3-D finite-element electromagnetics solver from ANSOFT, the High Frequency Structure Simulator (HFSS), to calculate the eigen-modes of the same silicon WPS [124]. Although much more computationally intensive, one valuable benefit of using the HFSS Eigen-solver, in contrast to the MPB code, is that it can handle lossy structures such as a lossy dielectric or a metallic EM crystal. The same lossless silicon WPS structure modeled with the MPB code is modeled again with the HFSS Eigen-solver. The HFSS Master/Slave boundary conditions are applied on the tetragonal unit cell surfaces to sweep the corresponding k-space in the irreducible Brillouin zone, with the same sweeping density as in the MPB simulation. In HFSS a phase difference Φ between one pair of Master/Slave boundaries can be assigned,

which corresponds to a k-space component along the normal direction $k_{//}$ by $\Phi = k_{//} \cdot l$, l being the normal distance between the boundary walls. Therefore a k-space point (k_x, k_y, k_z) can be exactly mapped to a combination of three phase differences of three Master/Slave boundary pairs along x, y, and z direction. After the completion of the HFSS simulation, the eigen-mode data is collected and the same interpolation method aforementioned is used to compute the photon DOS. The resulting DOS is plotted in Figure 2-4. The MPB result shown in Figure 2-3 (a) (converted to the real frequency DOS $\rho(f)$ by using the formulas presented above, with the lattice constant $a = 646 \mu m$) is also plotted in Figure 2-4 for comparison purpose. In general, it matches well with the HFSS-simulated DOS especially that most of the DOS peaks align up between the two methods. It can also be seen that there is some difference between the HFSS and the MPB results, for example, the slight shift of the main enhancement peak position and the small band gap width difference in Figure 2-4. The discrepancies are probably due to the following reasons. First, only 52 energy bands are included in the HFSS simulation approach (notice that the HFSS simulation is stopped around 400 GHz) because of limited computing resources. In contrast, the MPB simulation method includes 90 bands and these extra bands contribute to the DOS. Second, the strong Bragg resonances that result in the band gap may degrade the HFSS Eigen-solver calculation accuracy. Nevertheless, the agreement between the MPB and HFSS results shown in Figure 2-4 is still quite reasonable in terms of both the band gap position and the relative values of the DOS peaks. In the cases of the tungsten WPS and the photonic cavity discussed in later

sections, HFSS is the only software available to us that can deal with metallic and lossy dielectric structures. The fact that the HFSS and MPB computed DOS for the silicon WPS agree reasonably well serves as a validation of using HFSS to compute the DOS of the tungsten WPS and the Q factor of the photonic cavity.

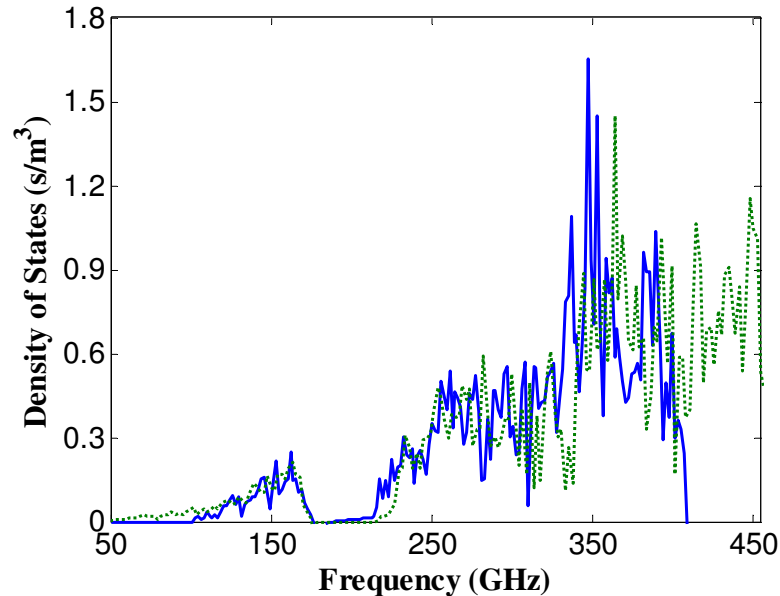
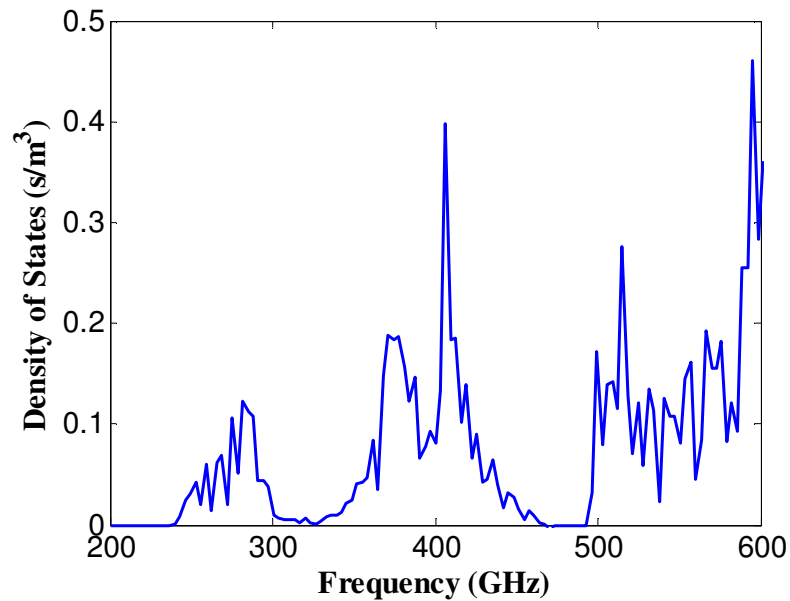


Figure 2-4. The real frequency DOS obtained using the HFSS eigen-solver (solid line) and the MPB (dashed line) for the silicon woodpile structure with the filling ratio $w/d = 0.272$, $D/d = 1.089$, and the rod periodicity $d = 646 \mu\text{m}$.

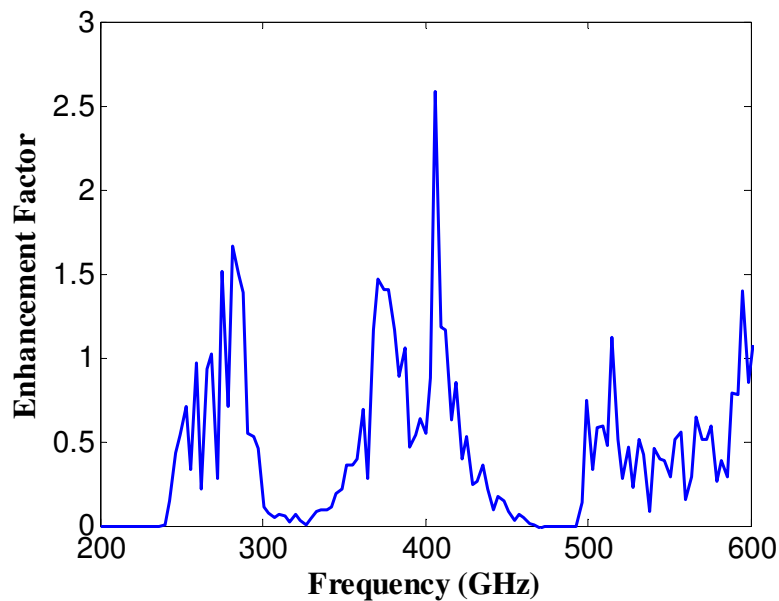
2.2.1.2 Tungsten Woodpile Structure

One significant advantage of building a WPS with metal is that the structure can be easily heated by applying an electric current to it. This would also lead to thermal emission power at much higher levels than at room temperature. Moreover, because silicon oxidizes when its temperature reaches 800-1200 °C in an atmosphere that contains oxygen or water vapor [125], the oxidation prevents silicon EM crystal from being heated to higher temperatures, as would be desirable for a potential thermal source.

The DOS of a tungsten WPS is calculated using the HFSS Eigen-solver approach. Tungsten has a bulk conductivity $\sigma = 1.82e7$ Siemens/m. The designed tungsten WPS has a filling ratio $w/d = 0.272$, $D/d = 1.089$, and a lattice constant $d = 646 \mu\text{m}$ exactly the same as the silicon WPS discussed before. The simulation results for the tungsten WPS DOS and the thermal radiation power enhancement factor are plotted in Figure 2-5(a) and 2-5(b), respectively. A complete band gap can be seen between 470 and 493 GHz. In comparison to the silicon WPS with exactly the same geometry, the gap center frequency is blue shifted and the overall gap is narrower. From Figure 2-4(b), it can be seen that an enhancement factor of 1.5 ~ 2.5 can be obtained around 282, 371 and 406 GHz.



(a)



(b)

Figure 2-5. (a) Calculated photon DOS for the tungsten woodpile structure with the filling ratio $w/d = 0.272$, $D/d = 1.089$, and the periodicity $d = 646 \mu\text{m}$. (b) Thermal radiation power enhancement factor for this tungsten WPS.

These numerical results indicate that the photon DOS can be redistributed through electromagnetic band engineering, thus leading to enhanced thermal radiation in, for instance, a desired THz frequency range. However, at room temperature, the normal blackbody radiation power peaks at IR frequencies; as a result, the fraction of the total radiated thermal power in the THz region is very small. Even at 1000 K, the total radiance in the frequency range from 0.5 to 1.0 THz is less than $10 \mu\text{W}/\text{cm}^2/\text{sr}$. Therefore, the enhancement factor of around 10 predicted above for the simple silicon and tungsten WPSs will not be sufficient for realizing a high power THz source. Nonetheless, a THz EBG object will certainly have a distinct thermal signature; and, consequently, it will be useful in thermal imaging and identification applications. In addition, advanced electromagnetic band engineering techniques may be used to

dramatically increase the photon DOS of an object hence dramatically increase the thermal radiation power enhancement factor to orders of magnitude higher in a narrow band of frequencies in the desired THz range. This large enhancement factor can be achieved with resonant cavity arrays.

2.2.2 Photonic Cavity Array

A special type of EM crystal with each unit cell consisting of a metallic micro-cavity will produce the desired large enhancement factors. It is well-known that those metallic micro-cavities can result in very narrow lines in their emission spectra at certain optical frequencies, and that those resonant frequencies can be controlled by appropriate cavity size adjustments [126-128]. By properly designing the micro-cavities, similar resonant emissions can be achieved at THz frequencies.

We consider here cubic dielectric boxes surrounded by metallic walls to achieve enhanced THz emissions. The schematic diagram given in Figure 2-6(a) shows the basic configuration. The unit cell of this quasi-3D structure is demarked by the dotted lines. The top metal layer will have either a thickness that is on the same order of its skin depth at the frequency of interest or a small aperture so that the resonant EM wave trapped in the micro-cavity can evanescently leak out [108].

According to theory, the only electromagnetic waves that can exist in a cavity have the specific wavelengths given by the expression

$$\lambda_{klm} = \frac{2na}{\sqrt{k^2 + l^2 + m^2}} \quad (2.5),$$

where n is the refractive index of the dielectric material filling the cavity, a is the side-length of the cavity, and the k , l and m indices are either zero or positive integers, but at least two of them should be nonzero [129]. These specific wavelengths are called the resonant wavelengths of the cavity. The largest one, for which two of the indices are unity and the other one is zero, is called the cutoff wavelength of the 110-mode and is given by $\lambda_{cutoff} = \sqrt{2}na$. Between the cutoff wavelength and an infinitely long wavelength, no electromagnetic wave is allowed to exist in the cavity. This behavior is analogous to an EBG structure. Due to the photon statistics (Bose-Einstein distribution), the amount of thermal radiation power at longer wavelengths is much more favored than that at shorter wavelengths. Thus, the mode at the cutoff wavelength is dominant over all other resonant modes and is the fundamental mode we focus on for the potential EM crystal based THz source.

To demonstrate these effects, we considered an array of metallic box micro-cavities, each with the side-length $a = 141 \mu\text{m}$ and filled with a dielectric material having a refractive index $n = 1.5$. We calculated the thermal radiation intensity at the cutoff frequency 1 THz ($300 \mu\text{m}$ wavelength). The radiation comes from two parts: one is the thermal emission from the dielectric box, whose DOS is denoted by $\rho_d(\lambda)$, and the other is from the surrounding metal walls. The latter wall contributions follow Planck's law. The total radiated thermal power density is then given by the expression

$$u(\lambda)d\lambda = \left(V_d \rho_d(\lambda) + V_m \frac{8\pi}{\lambda^4} \right) \cdot \frac{hc/\lambda}{e^{hc/\lambda kT} - 1} d\lambda \quad (2.6),$$

where V_d and V_m are, respectively, the total volumes of the dielectric box and the metal wall. All other physical constants are the same as indicated in Equation (2.1). Ideally, the DOS $\rho_d(\lambda)$ would be a delta function were the sizes of all the boxes exactly identical. In practice, the box size variations due to fabrication tolerances widen the DOS $\rho_d(\lambda)$. For our calculations, we treated it as a Gaussian function with a full-width half-maximum (FWHM) of 1% of the cutoff wavelength $300 \mu\text{m}$. Therefore, we obtained

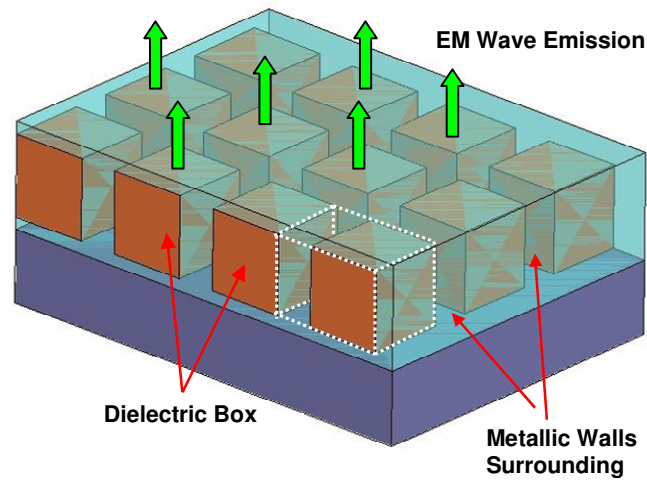
$$\rho_d(\lambda) = \frac{N_{res}}{\sqrt{\pi/a}} e^{-t(\lambda-\lambda_0)^2}, \quad \text{where } t = \frac{0.693}{(FWHM/2)^2} \quad (2.7)$$

In Equation (2.7), N_{res} is the total number of states at the lowest resonant frequency. It is equal to 3 due to the 3-fold degeneracy of the indices k , l and m . The aspect ratio V_d/V_m is another critical quantity that determines the thermal radiation power density for the micro-cavity array. It is taken to be 12 here, a reasonable value for typical fabrication processes. The thermal radiation power enhancement factor of this whole structure is given by

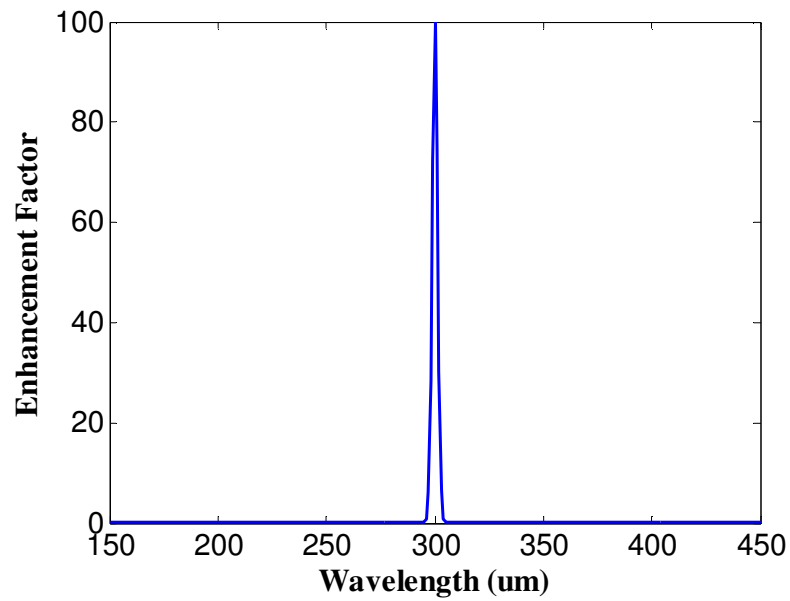
$$\text{Enhancement factor} = \frac{V_d \rho_d(\lambda) + V_m \cdot 8\pi / \lambda^4}{(V_d + V_m) \cdot 8\pi / \lambda^4} \quad (2.8)$$

The calculated result is plotted in Figure 2-6(b). An enhancement of 100 times over the normal blackbody radiation value is obtained. As anticipated, the power output is quite narrow-band. The FWHM of 1% of the cutoff wavelength is roughly equivalent to a variation in the box size of $3 \mu\text{m}$, an easily achievable one with standard fabrication processes such as photolithography and reactive ion etching [130-132].

In realistic scenarios, losses in the dielectric and the surrounding metal of the cavity will further broaden the thermal radiation spectrum. They can be taken into consideration by calculating the quality factor Q of the cavity at its cutoff frequency, given the cavity dimensions and material properties. The modified radiation FWHM including losses would be a combination of the FWHM from the cavity size variation and the FWHM from the losses (f_{cutoff} / Q). A cavity filled with polyethylene ($n = 1.52$ and loss tangent = 0.001 for the frequency band of interest here [133]) and with Platinum ($\sigma = 9.3e7$ Siemens/m) walls has been simulated in HFSS. The dielectric cubic box is $141 \mu\text{m}$ on each side, and the metal wall thickness between adjacent boxes is set to be $11.3 \mu\text{m}$. These choices gave an aspect ratio of about 12. The thickness of the top metal cover is chosen to be 180 nm , only slightly thicker than the Platinum skin depth at 1 THz. The simulation results show that this cavity has a quality factor Q around 285. This corresponds to a FWHM of 0.35%. Including the material losses of the micro-cavities, we find that the peak value of the enhancement factor is reduced and the width of the thermal emission peak shown in Figure 2-6(b) will be widened by about 35%.



(a)



(b)

Figure 2-6. (a) A schematic drawing of the metallic micro-cavities. The dotted lines enclose one unit cell of the structure. (b) The predicted thermal radiation power enhancement factor assuming a 1% variation in the size of the micro-cavities.

2.3 Sample Fabrication and Characterization

2.3.1 Fabrication of THz Silicon Woodpile EMXT

To verify our design and the fabrication process, a silicon WPS with the aforementioned dimensions is fabricated using a simple but robust mechanical layer-by-layer dicing process [80, 81]. Figure 2-7 illustrates the fabrication process. A series of grooves are cut into both the front and back faces of a silicon wafer (with a resistivity of $\sim 10^4 \text{ Ohm-cm}$) by using a programmable diamond dicing saw. The front and back cut orientations are rotated by 90° . The depth of the cut is set to open a window at the crossing point of the cuts, but to leave the array joined at the crossing points of the resulting bars. One wafer thus makes up one half of the WPS unit cell shown in Figure 2-1, left. The DISCO DAD320 dicing saw used here has horizontal and vertical step resolutions of $0.2 \text{ }\mu\text{m}$ and $1.0 \text{ }\mu\text{m}$, respectively. In addition, its horizontal and vertical minimum positioning accuracies are $2.5 \text{ }\mu\text{m}$ and $1.0 \text{ }\mu\text{m}$, respectively. Thus the estimated fabrication tolerances should be less than $5 \text{ }\mu\text{m}$ in the x- and y-dimension and less than $2.0 \text{ }\mu\text{m}$ in the z-dimension. The complete WPS is then assembled by stacking many wafers together with the help of pre-registered alignment marks. Figure 2-7(c) shows a photograph of the fabricated silicon WPS. Characterizations of this EBG sample at THz frequencies are carried out with various instruments, including THz time-domain spectrometer (THz-TDS), far-infrared Fourier transform spectrometer (FIR-FTS) and THz vector network analyzer (THz-VNA). A comparison among these three commonly used THz characterization instruments is given below.

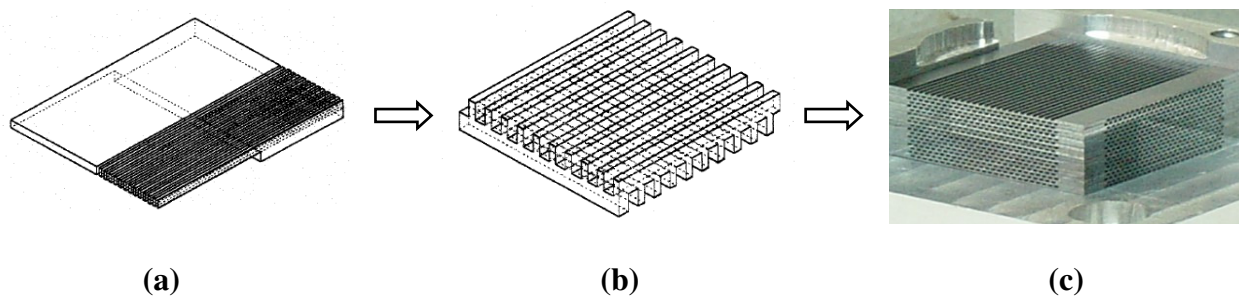


Figure 2-7. Illustration of the fabrication process for a 9-unit cell silicon WPS [80] using saw blade dicing.

2.3.2 Sample THz Characterizations

2.3.2.1 Comparison of THz Characterization Instruments

THz characterization of a sample is usually done by measuring the transmission or reflection responses of a probing signal. It has been a great technical challenge due to the relatively low photon energy at THz and the lack of efficient THz components. The former condition implies a vast amount of noise and thus poor signal-to-noise ratio (SNR) originating from the ambient background thermal radiation. The latter situation includes the lack of efficient THz sources, detectors and wave guiding components. Currently available THz sources are usually expensive and limited to low power output. THz spectra are occupied by many molecular vibration lines, which hinder THz spectral characterization too.

Most commonly used and commercially available THz characterization instruments include THz-TDS, FIR-FTS, and millimeter-wave and THz VNA. Other

THz instruments include THz radiometer, ellipsometer and confocal microscope, but they are not as widely used. The transmission measurement setups of THz-TDS and FIR-FTS are illustrated in Figure 2-8.

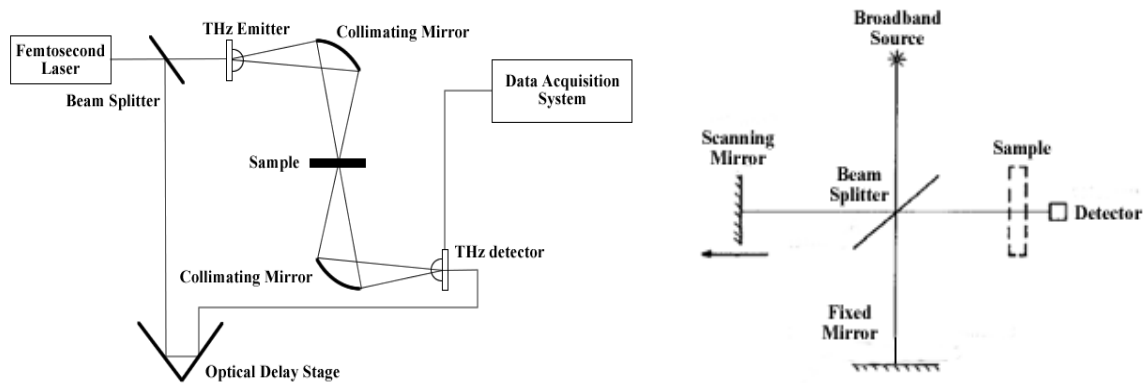


Figure 2-8. Left: THz-TDS experiment setup. Right: FIR-FTS block diagram.

A typical THz-TDS includes a femto-second laser, a beam splitter, a pair of THz emitter and receiver, collimating optics, an optical delay stage and data acquisition system (see Figure 2-8, left). The emitter utilizes either photoconductive antenna based on free electron radiation or electro-optical crystal based on nonlinear optical rectification to generate the THz signal. The detector of a THz-TDS is capable to record pico-second-duration pulse waveform via ultrafast gating and sampling system [56]. The measured waveform is Fourier transformed to extract the frequency-domain spectrum. In a transmission configuration the sample is placed in and out of the THz beam path, and comparison of the two spectra provides the transmission characteristics of the sample.

A far-IR FTS, on the other hand, consists of a broadband high-pressure mercury arc lamp as the source, a beam splitter, one fixed mirror and one scanning mirror, a power detector and data acquisition system (see Figure 2-8, right). Path difference between the scanning and fixed mirrors brings in a phase delay between the two split beams. Different frequency components in the beam experience different phase delays and interfere accordingly. Therefore, these components are amplitude-modulated and recorded as an interferogram, whose modulation frequencies are directly scaled-down frequencies from the original signal [54]. The spectrum of the signal is then recovered by Fourier transformation of the interferogram. Similar to the THz-TDS, two scans with sample in and out of the beam path are sufficient to characterize the transmission response of the sample.

THz-VNA consists of a frequency-tunable THz source based on photo-mixing [62] or EO crystal optical rectification [56], two-channel transmitter and receiver, phase detection unit and data acquisition systems. Incident wave with very narrow bandwidth – approximately monochromatic- passes through the sample via waveguide or free space coupling. Reflected and transmitted signals are recorded, and by calibration procedures they can be de-embedded to the sample surfaces. Reflectance and transmittance of the sample are obtained with both magnitude and phase. Time domain response of the sample may also be obtained by real-time inverse Fourier transform of the detected frequency-domain signal.

Each of these three characterization instruments has its own advantages and disadvantages. Table 2-1 compares some of the main characteristics of these instruments [134].

Table 2-1. Specification comparisons of THz-TDS, FIR-FTS and THz-VNA.

	THz-TDS	Far- IR FTS	VNA
Measure. Domain	Time domain	Frequency domain	Frequency domain
Transmission / Reflection	Both available	Both available	Measured simultaneously
Phase Measurement	Available	Need special setup	Available
Dynamic Range of Power	1e8 (< 3 THz)	~ 300 (< 3THz)	1e19 @ 200 GHz 1e6 @ 700 GHz
Typical Resolution	3 GHz	3 GHz	10 KHz
Peak Power	1 mW (integrate over the bandwidth)	0.1 uW (integrate over the bandwidth)	1.3 mW @ 200 GHz 0.001 mW @ 600 GHz
Bandwidth	Tens of 10 GHz to 45 THz	100 GHz to visible	Up to 1THz
Noise Equivalent Power	1e-16 W/ rtHz (< 3 THz)	8e-10 W/ rtHz (< 3 THz)	1e-12 W/ rtHz min.
Source Stability	Good	Not good	Good
Setup Difficulty	Initial stages	Mature, easy	Initial stages

Transmission and reflection setups are available for all three instruments; however, both measurements can be done simultaneously by a THz-VNA without the necessity of rearranging the equipment. Phase measurement is readily available for THz-TDS and THz-VNA, whereas FIR-FTS cannot measure phase directly since it uses a power detector such as bolometer or Golay cell; however, the phase delay introduced by a sample is measurable if the sample is placed between the beam

splitter and either the scanning or the fixed mirror (see Figure 2-8, right) [134]. In that case, sample in and out result in two different interference intensities when the mirrors are at the same positions. By comparing the phase difference of the Fourier transformed interferograms, the extra phase delay due to the sample can be obtained. For the spectral specifications, THz-TDS has an exceptionally high dynamic range over a wide bandwidth, because its unique gating system excludes most of the background radiation. Frequency resolution of the THz-VNA is the best so that it is capable of resolving very fine spectral lines. However, its overall measurement bandwidth is limited in comparison with the other two instruments. Also, different transmitter/detector modules and calibration kits are necessary to cover different frequency ranges.

2.3.2.2 Sample Characterization Results

The THz-TDS system used is a commercially available T-ray 2000 from Picometrix Inc. with photoconductive antenna emitter and detector. The system covers from around 50 GHz to 1.2 THz with a best resolution of 1.8 GHz. Normal incidence is applied, with the incoming wave along the stacking direction of the WPS sample. In the measurement, the silicon WPS is placed in the path of a pico-second-duration pulse of THz radiation, and the transmitted pulse waveform is compared with a reference pulse (no sample being present). Then by Fourier transforming the signal transmitted through the sample, the sample transmission coefficient is obtained in the frequency domain. The TDS result shown in Figure 2-9

explicitly reveals the predicted stop-band centered around 200 GHz. Also plotted in Figure 2-9 is the HFSS simulated transmission coefficient for normal incidence. Not only does the predicted band gap around 200 GHz match well, but also the predicted secondary band gap near 310 GHz and the various predicted transmission peaks match quite well with the measured data. The slight red shift observed in all of the features in the TDS spectrum with respect to the simulation is probably due to errors associated with the fabrication tolerances. Oblique incidence transmission measurements are also performed. The results (not shown) verify that the band gap at 200 GHz is omni-directional (a true 3-D band gap). The good agreement between the measured and simulated transmission results verifies the WPS design and fabrication procedures.

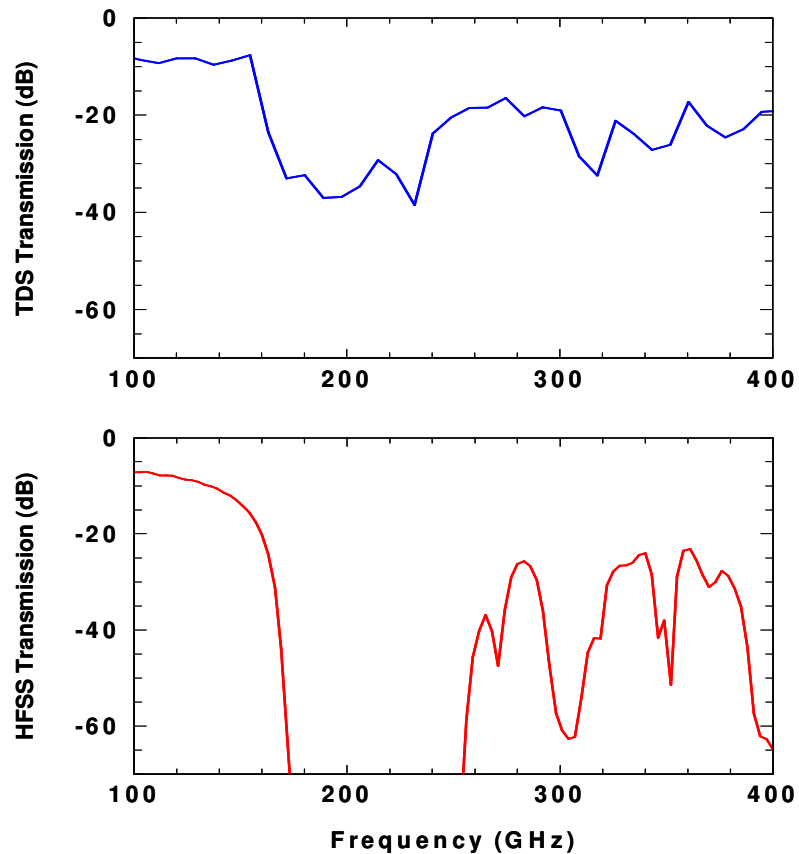


Figure 2-9. Transmission responses (normal incidence) of the silicon WPS sample: (top) THz time-domain spectroscopy (TDS) measurement, (bottom) HFSS Simulation.

The FIR-FTS used is a Beckman FS-720 step-scan Michelson interferometer with mercury arc lamp as source and liquid Helium cooled bolometer as detector to cover from 150 GHz to 3.6 THz. The THz-VNA measurement is done with an Agilent PNA E836x network analyzer equipped with N5260A mmWave controller and Oleson frequency extension modules WR-5, WR-6 and WR-8. The best frequency resolution is 4.5 GHz for the FTS and 1 KHz for the THz-VNA. Normal incidence is also applied in both measurements.

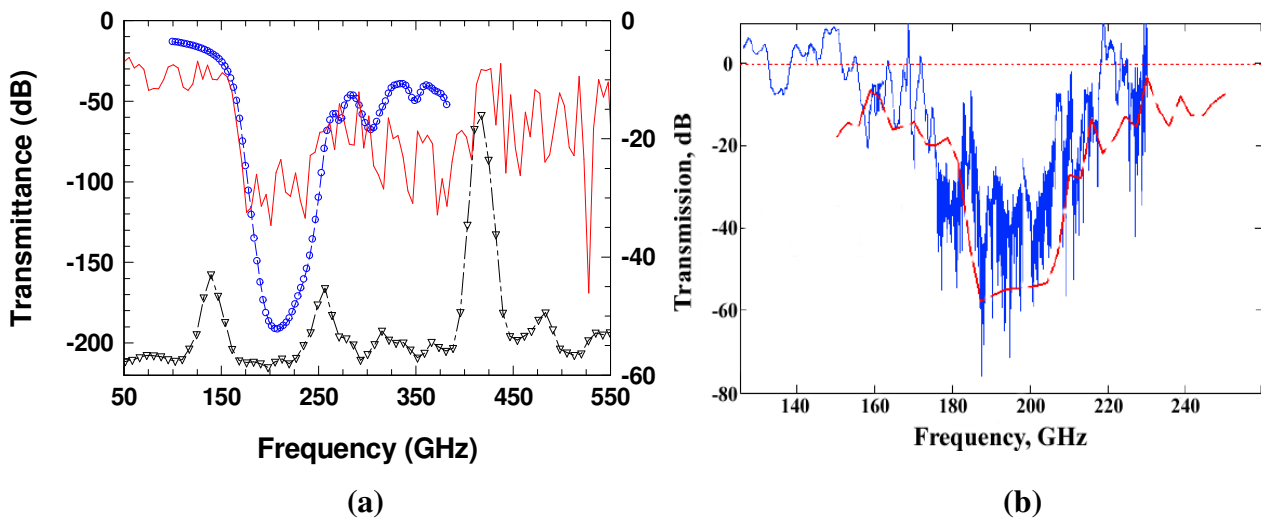


Figure 2-10. Silicon WPS transmittance: (a) FIR-FTS result (dash-dotted line with triangles, a.u.) compared with THz-TDS measurement (solid line, right ordinate) and HFSS simulation (dashed line with circles, left ordinate) results. (b) VNA measurement (solid line) compared with transfer-matrix-method (TMM) calculation (dashed line).

In Figure 2-10(a), THz-TDS (right ordinate) and FTS characterization results are plotted together with the HFSS simulated transmittance. The FIR-FTS transmission spectrum is vertically shifted for a clearer view. For normal incidence, simulation predicts the WPS band gap spanning from 180 to 250 GHz. Both the TDS and FTS spectra verify very good agreement. Pass-bands from 100 GHz to 160 GHz and around 270 GHz are also observed in both measurements and are in good agreement with the simulation. Correspondence with the second band gap at 300 GHz can also be found in both measurements. In general, the sensitivity of the FTS is poor due to low power content at the low frequency (THz) end of the mercury lamp source. In addition, the amplitude modulation from the multiple reflections within the beam splitter can also cause spurious peaks (for example, near 420 GHz).

Figure 2-10(b) shows the THz-VNA characterization result (solid line) and as a comparison, the calculation result using the transfer-matrix-method (TMM) is also plotted. The TMM treats each cascaded section of a structure separately and solves Maxwell's equations to obtain the scattering matrix of each section. By successive multiplication of each scattering matrix, the reflection and transmission coefficients of the overall structure can be calculated [37]. The fundamental band gap around 200 GHz is again verified and good agreement between simulation and experimental results is observed. Due to uncertainties in the calibration procedure, the VNA measured transmittance goes beyond 0 dB at places. Overall, all three measurements are reasonably consistent in the silicon WPS band gap characterization, thus verifying the WPS design and fabrication procedures. Furthermore, from the experimental procedure and results, it is concluded that the THz-TDS is probably the most convenient instrument with sufficient accuracy for our purpose.

2.4 Sample Thermal Emissivity Measurement

2.4.1 Experiment Setup

To experimentally study the predicted THz thermal radiation enhancement, direct thermal emission measurements of the fabricated silicon WPS are performed using the same Beckman FS-720 Fourier transform spectrometer as in the characterization. The FTS employs a scanning Michelson interferometer to transform the incoming radiation into an amplitude-modulated signal whose modulation

frequencies are the scaled-down frequencies in the original signal. The modulated signal is recorded as an interferogram and the original spectrum is then recovered by Fourier transformation. The maximum resolution of the FTS achieved in this work is 4.5 GHz. The schematic of the experimental configuration is shown in Figure 2-11. The commonly used mercury lamp source for the FTS is replaced by the silicon WPS sample under study, sitting on a sample holder with heating bath. For comparison, a THz radiation-absorption-material (RAM) [135] with an absorption coefficient close to 1 from 100 to 600 GHz and the same form factors as the WPS sample is used as the reference (control) blackbody source. A liquid helium cooled (4.2 K) silicon composite bolometer (IR Labs model JPKI06MA) is used as the signal detector, and a lock-in amplifier (SR510m) is employed to enhance the measurement sensitivity.

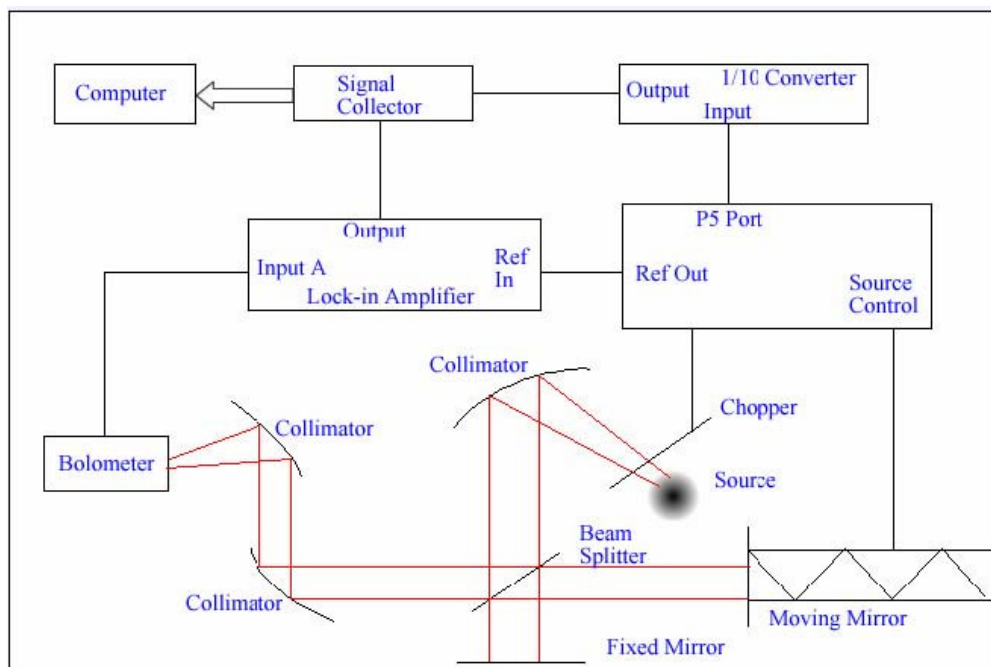


Figure 2-11. Schematic of the Fourier transform spectrometer (FTS) setup for the direct thermal emission measurements.

The sample is mounted on an adjustable stage with a sample holder, an aperture, and electrical heating elements. The aperture, which is made from aluminum, blocks thermal emission from the sample except at the center aperture area. The aperture has a diameter of 0.64 cm, making the sample under study a good point source with respect to the FTS collimator mirror. A mechanical chopper is located in between the collimator and the aperture and provides the reference signal for the lock-in amplifier. The thermal radiation from the sample gets modulated by the chopper on-and-off positions, gets collimated, and passes through the FTS. It is then detected by the cooled bolometer, which is positioned right behind the FTS output window. The optical beam path is located in a vacuum environment except between the FTS output window and the bolometer to reduce signal fluctuations and attenuation caused by the atmosphere. The heating elements are Ni-Chrome alloy made resistive wires directly attached to the back of the aluminum-made sample holder, and the holder is kept in good thermal contact with the sample under study while being thermally isolated from the stage by a ceramic thermal isolator. A closed-loop thermal-couple temperature controller is used to maintain the sample to within 0.1 Kelvin of a specified constant temperature. Since the temperature sensor is mounted on top of the sample holder, the actual sample temperatures at the aimed areas would be slightly different than the control temperature because of the thermal conductivity differences between the holder and different samples (silicon WPS and RAM), which inevitably lead to a temperature gradient. To compensate that, a

pin-to-point temperature measurement right at the aimed sample area is carefully carried out and the control temperatures are calibrated accordingly for different emitting samples.

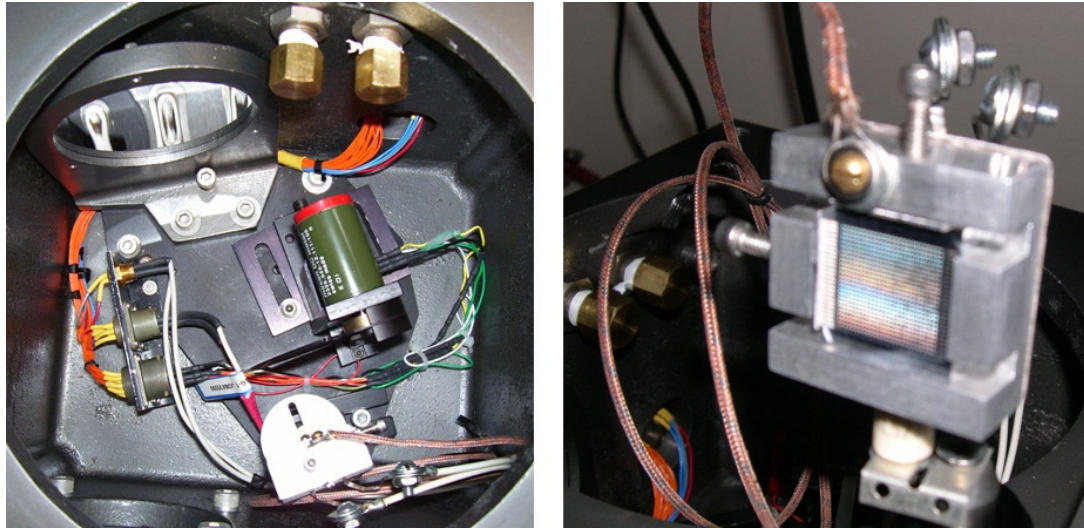


Figure 2-12. Left: Image of the emission measurement setup in the FTS sample chamber, showing the collimating mirror, the chopper, the sample stage and holder (Aperture not present). Right: Zoom-in image of the sample holder with the silicon WPS sample mounted in the middle. The aluminum-made holder makes a good thermal bath, with a thermal couple pinned on the top for temperature monitoring.

2.4.2 Calibration Scheme and Measurement Results

The detector sees the sample thermal radiation when the chopper is open and the chopper thermal radiation when it is closed. Because of the working principles of the lock-in amplifier, the detected signal is proportional to the power difference between the sample radiation and the chopper radiation. The final emission spectrum recorded by the FTS was therefore $W_{sample}(f) - W_{chopper}(f)$, where the suffix denotes the specific radiation source. In addition, the recorded signal consists of the sample

thermal emission, the thermal emission from the heating element transmitted through the sample, the background thermal emission reflected by the sample into the FTS, and the thermal emission from the aperture. The recorded differential spectrum can then be expressed as the following equation

$$W(f, T_s) = \varepsilon_s \cdot W_{BB}(f, T_s) + R_s \cdot W_{SUR}(f, T_{RT}) + X_s \cdot W_{HE}(f, T_s) + W_{Aperture}(f, T_{RT}) - W_{Chopper}(f, T_{RT}) \quad (2.9),$$

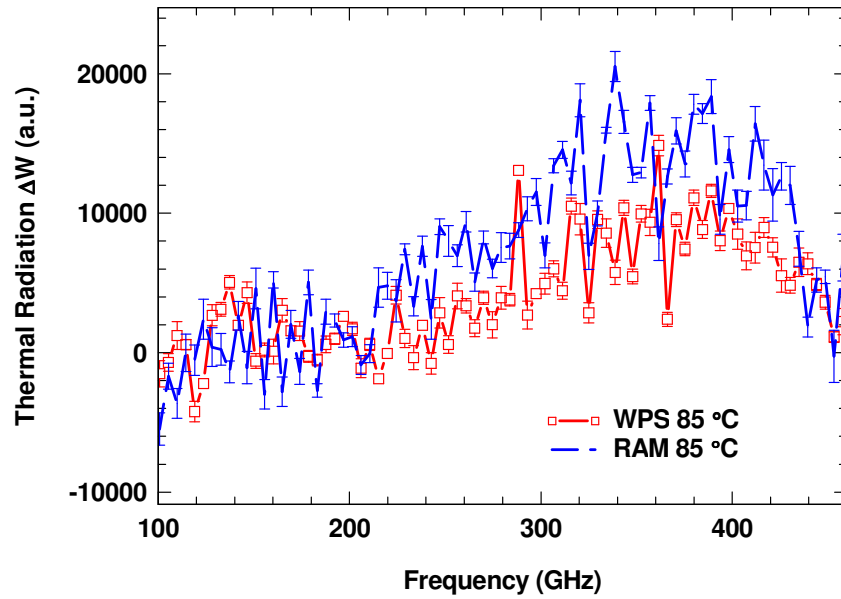
where ε_s , R_s , and X_s are the emission, reflection, and transmission coefficients of the sample, respectively, and T_s and T_{RT} are the sample and room temperatures. The first term in Equation 2.9 represents the thermal emission from the sample, where W_{BB} is the normal blackbody radiation power density at the sample temperature T_s . The second term represents the thermal radiation from the surrounding environment (W_{SUR}) that is reflected by the sample into the FTS. Since the heating stage is thermally isolated from the surrounding environment, the surrounding environment is at room temperature T_{RT} . The third term is the thermal radiation from the heating element (W_{HE}) transmitted through the sample at temperature T_s . The last two terms are the thermal radiations from the aperture ($W_{Aperture}$) and the chopper ($W_{Chopper}$). One thing to point out is that ε_s , R_s , and X_s are all considered to be independent of the temperature, which is a valid assumption over the studied temperature range.

In order to compare the sole thermal emissions from the silicon WPS and the RAM samples, the background signals from the surrounding environment, the heating element, the aperture, and the chopper need to be eliminated. This is achieved by

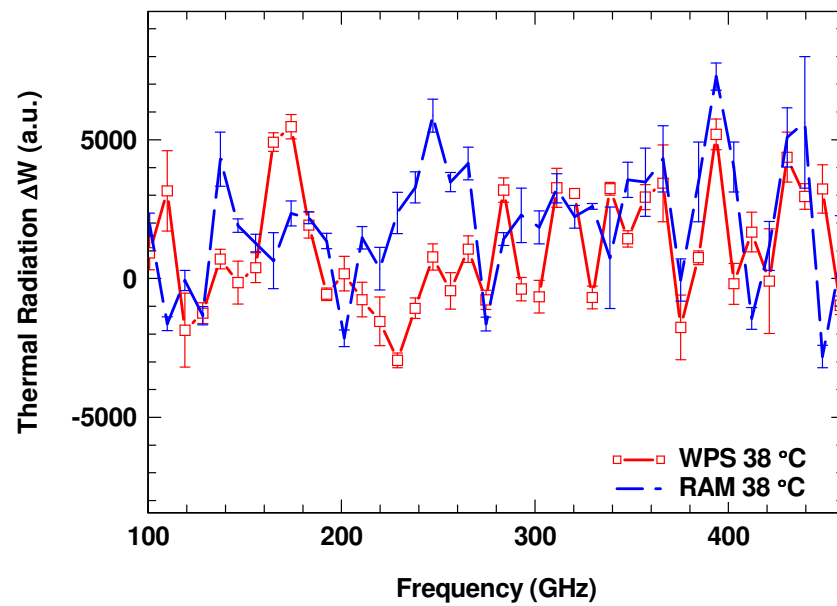
subtracting the measured spectrum at room temperature T_{RT} from the measured spectrum at an interested higher temperature T_s . This way the second, fourth, and fifth terms in Equation 2.9 are canceled out, and the resulting spectrum is then:

$$\begin{aligned}\Delta W &= W(f, T_s) - W(f, T_{RT}) \\ &= \varepsilon_s \cdot (W_{BB}(f, T_s) - W_{BB}(f, T_{RT})) + X_s \cdot (W_{HE}(f, T_s) - W_{HE}(f, T_{RT}))\end{aligned}\quad (2.10).$$

This expression is a combination of the sample thermal emission and the heating element thermal emission transmitted through the sample. According to the THz-TDS transmission measurement, the transmission coefficient of the RAM can be well approximated to be zero. Therefore the RAM differential spectrum represents the RAM thermal emissions directly. In addition, from Figure 2-9, it is observed that the power transmission through the silicon WPS is also quite low (less than -10 dB for most of the spectrum). Therefore, the second term in Equation 2.10 can also be omitted. A comparison of the WPS and RAM emissions is given in Figure 2-13 by plotting the ΔW (in arbitrary units) obtained for both the silicon WPS and the RAM samples. This comparison is fair since the term $W_{BB}(f, T_s) - W_{BB}(f, T_{RT})$ in Equation 2-10 is a constant factor for both the WPS and the RAM samples at the same temperature.



(a)



(b)

Figure 2-13. The thermal radiation differential spectra for the RAM (dashed) and the WPS (squares) samples at (a) 85°C and (b) 38°C. The error bars are based on statistics.

The thermal radiation results measured at two different temperatures (38°C and 85°C) are plotted in Figure 2-13. Because the absolute thermal emission power at these temperatures are low and the sensitivity of the FTS system is not optimal at the

lower frequency end (100 GHz to 500 GHz) [136], all of the emission spectra are measured multiple times and averaged to reduce the noise level. The error bars in Figure 2-13 represent the statistical measurement errors.

Experimentally measured enhancements of the WPS thermal radiation over the control blackbody sample can be observed around 110, 146, 165, 288, 362 and 440 GHz for the 85°C spectrum. Enhancements at similar frequencies are also seen for the 38°C spectrum. These enhancement peaks match up qualitatively well with the predicted enhancement peak positions given in Figure 2-3(c). Consider the most significant enhancement peak at 364 GHz in Figure 2-3(c) as an example, a sharp enhancement peak at 362 GHz is observed in the measured 85°C spectrum (Figure 2-13(a)). The corresponding enhancement peak in the 38°C spectrum (Figure 2-13(b)) appears at 340 GHz. This 20 GHz shift is probably due to the relatively low signal-to-noise ratio (SNR) at the lower temperature of 38°C compared to 85°C. Besides the main enhancement peak, other frequencies at which enhancement peaks occur also qualitatively match well with the predictions in Figure 2-3. The measured thermal radiation spectra in Figure 2-13 look quite noisy because of the limited SNR in the measurements at this frequency range. However, statistical error bars verify that the measured WPS emission enhancements over the control blackbody sample are repeatable observations. Therefore, based on the good matching between the predicted and measured (for both temperatures) enhancement peak frequencies, the results shown in Figure 2-13 justify, at least qualitatively, the prediction of the thermal radiated power using the DOS calculation. They are also good indications that an

EBG emission source with enhanced THz thermal radiation may be feasible. Quantitative comparison between the measured and the predicted values is not attempted, since the measurement sensitivity is not high enough at this frequency range. Also, one possible reason for the enhancement level measured to be much lower than shown in Figure 2-3 is the coupling from the photon states in the EMXT to outer-space radiation. Not all these photon states are propagating modes and can radiate the energy out. Therefore, a more advanced model considering the coupling from the local density of states (LDOS) of an EMXT with finite lattices to free space is necessary.

2.5 Conclusion and Discussion

In this chapter we present a novel idea of modifying THz thermal emission spectrum by using different types of EMXTs as the active THz sources. It is demonstrated that large enhancements over normal blackbody radiation may be achievable with the large redistribution of the photon DOS enabled by the EBG effects associated with an EM crystal. These enhancement factors are shown to be independent of the temperature. The design and fabrication of a silicon woodpile crystal are also accomplished. The silicon WPS sample is characterized by the transmission spectroscopy methods using THz-TDS, FIR-FTS, as well as THz-VNA instruments. The results from three characterization instruments agree well with each other, and are all quite consistent with the simulation.

Direct thermal emission measurements are carried out with the fabricated silicon woodpile sample and a RAM sample (approximately a blackbody radiator) as the sources. Emission enhancements of the WPS over the RAM are observed at several frequencies. These enhancements occurred at frequencies very close to those predicted in the photon DOS calculations. The observed enhancements are a good indication that properly engineered EM crystals may lead to an alternative THz thermal source. However, the poor enhancement level measured in comparison to the calculated values implies that the coupling between the interior photon modes and the outer-space propagation modes can not be omitted in the calculation, and prediction of the thermal emissivity based on an infinite-lattice DOS is not adequate.

In order to verify, as predicted, that the observed enhancement is a total thermal radiation power enhancement over the entire 4π solid angle sphere, emission measurements covering the entire space are required. In the experiment reported here, the power detection is confined within a 0.11π solid angle along the sample surface normal direction. However, transmission and reflection characterizations of a scaled-down WPS at optical frequencies have been reported previously with minimal angular variances [120, 137]. The oblique-incidence THz-TDS transmission characterization of the WPS sample used in this work also shows small angular variance. Therefore, it is reasonable to assume that the thermal radiation enhancement should not have a strong angular dependence. It is worth emphasizing that the thermal radiation enhancement predicted in Figure 2-3 is a total power enhancement in the THz regime based on the calculation of the DOS for the WPS sample, and that the

measured WPS emission enhancements along the surface normal direction support those calculations. Nevertheless, Kirchoff's law holds at all directions due to the Helmholtz reciprocity law [138-140]. Therefore, the measured enhancement from silicon woodpile EMXT over the RAM at the surface normal direction puts a question mark on the validity of Kirchoff's law when the radiating body is an EM crystal. After all, Kirchoff's law will not hold if a thermally pumped EMXT is not in an equilibrium state [76, 105]. Also, [141] states that Kirchoff's law would not hold for the perfect reflector case with experimental evidence, and blackbody radiation is critically dependent on the nature of the emitting body. However, in order to draw a solid conclusion on this question, more obvious emission enhancements than shown in Figure 2-13 over the blackbody need to be observed in experiments. After all, the RAM is nearly as perfect as a blackbody in the measurement frequency range according to its data sheet, but it is still a greybody. Also this emission measurement should really be conducted at frequency bands where the FTS system exhibits good sensitivity, preferably between 600 GHz and 3.2 THz, meaning EM crystals with band gaps falling into that frequency range shall be employed as the thermal radiation source in future measurements.

Along the path of trying other EM crystals than the silicon WPS, structures such as the tungsten WPS and the metallic micro-cavity array will be designed with optimized thermal emissions in the THz region to achieve higher thermal radiation powers. Also, dual-gap or even multiple gap EM crystals will be investigated, and their thermal radiation characteristics will be explored. Multiple gaps would result in

much stronger photon DOS redistributions and possibly much higher thermal radiated power enhancements over the normal blackbody values than could be realized by single gap EBG structures. In addition, the possibility of making the proposed sources tunable will be explored. Since the stop-band positions within an EM crystal are largely dependent on the refractive index n of its constitutive material, and since the refractive indices of certain materials such as semiconductors or liquid crystals can be controlled by external biases, we believe that tunable EM crystal-based THz sources are possible. If the feasibility of making EM crystals with such materials is confirmed, tunable THz radiation achieved by a tunable n would be quite interesting. Future theoretical and experimental work may lead to a promising alternative type of THz source, as well as to a better understanding of the physics underlying thermal power radiated by an EM crystal.

CHAPTER 3. RAPID PROTOTYPING OF THz EMXT STRUCTURES

As briefly reviewed in Chapter 1, electromagnetic crystals can be employed to realize multiple photon functionalities and achieve various components from these functionalities. Since Maxwell's equations are scalable with wavelength, many of those EMXT based components proposed or realized in the optical regime can be directly scaled to THz wavelengths. However, one serious challenge is how to fabricate these EMXT components with feature sizes around THz wavelengths, as well as how to integrate these components together to build a THz micro-system. Moreover, can we fabricate an entire system instead of making individual components and mounting and aligning them together? The best solution would be to have a feasible THz prototyping technique. Modern rapid prototyping technologies are now capable of assemblage resolutions that allow direct fabrication of EM structures in the GHz and THz frequency regimes. We have developed a novel polymer jetting rapid prototyping technique and demonstrated the fabrication of several structures with 3D electromagnetic band gaps in the 100-400 GHz range. Characterization of these structures via THz Time-domain Spectroscopy (THz-TDS) shows very good agreement with simulation, confirming the fabrication accuracy of the approach. This rapid and inexpensive 3-D fabrication method may be very useful for a variety of potential THz applications, such as fabrications of THz EMXT components, sub-wavelength effective medium, THz holograph generator, and integrated THz micro-system, etc.

3.1 Background and Motivation

Research involving the Terahertz (THz) spectrum has recently been experiencing rapid growth [21]. This growth is application-driven and involves wide-ranging topics including: chemical and astronomic spectroscopy and sensing [21], medical and biological imaging and analysis [22], defense and security screening [21], material research and semiconductor industry [142], and next generation communication networks and radars [37]. The great potential of THz technology originates from the plethora of physical and chemical processes occurring in this region as well as the relatively high resolution and bandwidth of THz compared with microwave frequencies. On the other hand, free space THz communication suffers less scattering loss than free space optical communication, and is able to function under IR and optical blind conditions such as smoke, cloud and sandstorm. THz imaging would “see through” many common obstacles such as paper, cardboard, clothes, wood, etc. for the same reason, therefore find itself very suitable for security screening and concealed weapon detection. Recently, many THz applications have become closer to reality with the rapid advancing of THz components such as sources, detectors, filters, reflectors, guiding structures, antennas, (transition to) planar circuits and materials [21].

Electromagnetic band gap materials—materials in which certain propagating modes are forbidden—are currently one of the most fast developing subfields in electromagnetic research. Because of their special nature, EBG structures (or more generally, structures with periodic lattices) can be used to control and tailor optical

processes such as emission and detection of electromagnetic radiation [2, 52, 54], wave propagation guiding [4, 40], and refraction under artificial permittivity tensor [91]. Many works have been reported on EBG-based THz components, including sources, detectors, filters, waveguides and artificial dielectrics [21, 37, 136, 173]. However, one of the major challenges remaining to be overcome involves the practical difficulties in component fabrication, as the feature dimensions of THz EBG components fall in a transition region between the conventional micromachining techniques used for microwave applications and the micro/nano-fabrication methods in use at optical frequencies [80]. Several semiconductor fabrication approaches, including dicing saw machining [81], wet etching [82], deep reactive ion etching (DRIE) [83], deep X-ray lithography [84] and laser micromachining [80, 84], have been reported. These methods are expensive, and require extraordinary care to achieve even relatively uniform THz EBG geometries, let alone the more complicated structures such as defect cavities and waveguides.

Alternatively, a variety of rapid prototyping technologies have been explored for fabricating 3-D microwave circuits and EBG components, including polymer and ceramic stereolithography [90, 91], fused deposition modeling [92] and selective laser sintering [92]. Among them, polymer stereolithography has the highest accuracy [91]. Using these methods, EMXT waveguides [93], 3-D antennas [91, 144] and band-pass filters [90] have been demonstrated. However, these techniques are only successful at frequencies up to approximately 30 GHz.

More importantly, integration of various types of components is demanded to achieve a self-sufficient THz system. How to integrate those components together while maintaining high performance and low cost is a big challenge for practical applications. Besides that, the integrated THz system shall be easily customizable, for instance the system shall be easily adaptable to a specific working frequency range assigned by the user, or can be quickly reconfigured if certain component(s) in the system needs to be modified or replaced according to users' requirements.

The ultimate solution to meet all aforementioned challenges is to develop a THz prototyping technique. The prototyping technique should not only allow fast fabrication of THz components with arbitrary shapes, but also bring the fabrication to a systematic level to manufacture the whole THz micro-system from scratch, therefore saving all the troubles of components alignments and integration afterwards. The prototyping should be low-cost and flexible, so whenever a specific customization to a THz micro-system is necessary, the system design can be conveniently updated and a new system can be quickly re-prototyped. Also, the prototyping shall enable mass production of THz components and micro-systems.

3.2 THz Rapid Prototyping by Polymer Jetting Technique

The multiple-scattering nature of EBG-physics requires that the EBG structure exhibit sub-wavelength features. For the frequency range of interest (100 GHz—10 THz), the corresponding wavelength range is 3 mm—30 μm . Of course, the particular

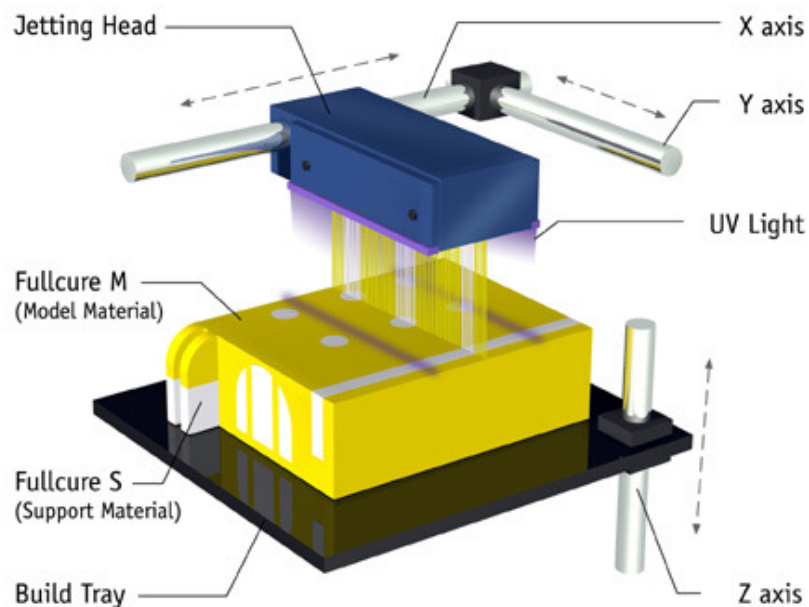
constant of proportionality between a characteristic feature size and the wavelength at which the band gap occurs depends critically on particular structure design. However, in general, to produce useful band gap structures in this wavelength range, a fabrication technique that can provide feature sizes in the range 1mm—10 μm would be required.

Polymer-jetting rapid prototyping machines now have fabrication resolutions that fall in this range. The lab of our collaborator's group contains a commercial rapid prototyping machine (Objet Eden 350 [145]) that claims a fundamental resolution of 42 μm in the x and y directions and 16 μm in z direction, based on the step control length of the automated polymer printing head and the fabrication tray in the machine (see Figure 3-1).

For this prototyping machine, the fabrication process is relatively straightforward. Figure 3-1 gives a demonstration of the 3-D prototyping process. The desired EBG structure is designed and analyzed in an electromagnetic simulation program such as HFSS [124] or CST [146]. Once the design is finalized, the resulting 3-D geometry is exported into a CAD program where it is converted into a series of layered slices, each representing a 16 μm -thick region of the model. As earlier slices provide the surface upon which later slices are constructed, the slice description consists of two different material types—a model material which is assigned to regions that are actually part of the cross-section of the desired object (grey regions of the sample in Figure 3-1), and a support material, which is used to provide a base

upon which the model sections of future slices can rest (white regions of the sample in Figure 3-1).

The data describing the slices are sent sequentially to the prototyping machine. As each slice arrives, a series of print heads, much like the print heads of an inkjet printer, deposit a thin layer of two different UV-curable materials onto the construction tray. Regions identified as model material in the slice are covered with uncured acrylic polymer, while support material regions receive uncured water-soluble polymer. UV lamps on the print head immediately cure both materials as they are being deposited. After the layer is complete, the construction tray is lowered by 16 μm and the next slice is processed.



The Objet PolyJet Process

Figure 3-1. Illustration of the polymer-jetting process for 3-D objects prototyping.

After the entire model is complete, the construction tray rises and the part may be removed. The finishing step involves using a high-pressure water spray to remove the water-soluble support material, leaving just the model material in the desired 3D shape. Printing involving both model and support materials is called “matt mode”, whereas the machine can also print only the model material under “glossy mode”, if the support material is not necessary in the fabrication process. This way improved surface termination could be achieved, but may lose some printing dimension accuracy since support materials as fillers yield more accurate dimension definitions.

Our initial attempts at constructing THz EBG structures via this approach reveal several areas where we needed to modify the standard fabrication methodology, or adapt certain limitations into our design process. First, despite the stated resolution of the machine ($42\ \mu\text{m} \times 42\ \mu\text{m} \times 16\ \mu\text{m}$), we find that the minimum practical feature sizes in the horizontal dimensions x and y are approximately $150 - 200\ \mu\text{m}$ because the polymer droplets spread on the tray. Thus we limited our designs to these scales initially. Second, the resulting structures are often too fragile to withstand prolonged washing with the high pressure water jet. We find that soaking any part in a 3% aqueous solution of sodium hydroxide (NaOH) softens the support material to the point where it can be gently washed away.

Construction of THz EBG structures with this system is extremely quick and inexpensive. The time required to fabricate parts with the rapid prototyping machine is volume dependent (as this controls the size and number of slices that must be fabricated). For the EBG structures constructed so far, build times have been

approximately 30 minutes, with consumable costs of approximately \$10. Mass production of multiple parts is also feasible because the current prototype machine allows a build volume of up to 1 ft x 1 ft x 1 ft, which may consist of thousands of THz components.

3.3 THz 3-D EMXT Examples for Demonstration

To validate the prototyping technique, we designed and fabricated two different EBG structures and measured their transmission responses via the same THz Time-domain spectrometer (THz-TDS) as introduced in Section 2.3.2.2 of Chapter 2. The THz-TDS operates by propagating a picosecond pulse through the material under test and Fourier transforming the time-domain transmitted signal to extract frequency response. The results of the THz-TDS measurements are then compared to finite-element simulations of the transmission properties of the structures.

3.3.1 Build Materials Characterization

For the design (and eventual simulation) of the structures, it becomes necessary to characterize the electromagnetic properties of the model polymer, specifically the complex permittivity ($\epsilon = \epsilon' - i\epsilon''$) and permeability ($\mu = \mu' - i\mu''$). As the polymer is non-magnetic ($\mu = 1$), the complex permittivity can be determined by performing a single transmission experiment using a THz-TDS [147]. The dielectric constant ϵ' and the loss tangent $\tan\delta = \epsilon''/\epsilon'$ (a convenient parameter representing

loss of a dielectric material) are extracted from the measured phase and magnitude of the transmission coefficient of a uniform 3-mm thick slab of the polymer material. The transmission setup of the THz-TDS can be found in Figure 2-8, left, with the sample in the middle of the THz beam being the polymer slab. The cross-section area of the slab is large enough to cover the entire THz beam spot at the beam waist position.

As the fabrication process involves water and aqueous solutions as discussed in the previous section, sample desiccation might be necessary to avoid the significant loss of THz signals in water [22]. To investigate the impact of water content in the polymer structures, the polymer slab was first characterized, and then placed in a desiccation chamber to remove the water content. Initially, the weight of the sample decreased as water was extracted, but eventually the weight stabilized, and then the sample was removed from the chamber. During this process we observed a weight decrease of approximately 0.5%. After desiccation, the slab characteristics were measured again and compared with the pre-desiccation results. In the 100—600 GHz spectral range, the loss tangent of the desiccated sample is smaller than the undesiccated sample, but the two differ by less than 30% at the worst case and the differences for most frequencies are less than 20%. The dielectric constants in the two cases are almost identical. Therefore, we considered signal attenuation from the water content in the polymer as mild (would result in an additional transmission loss of ~ 1 dB), and did not desiccate the EBG structures before testing. The dielectric constant and loss tangent for the desiccated sample are plotted in Figure 3-2. A slow decrease

of the dielectric constant is observed as the frequency increases, from 2.78 at 100 GHz to 2.7 at 600 GHz. The material loss tangent slowly increases from 0.02 around 100 GHz to 0.05 at 600 GHz.

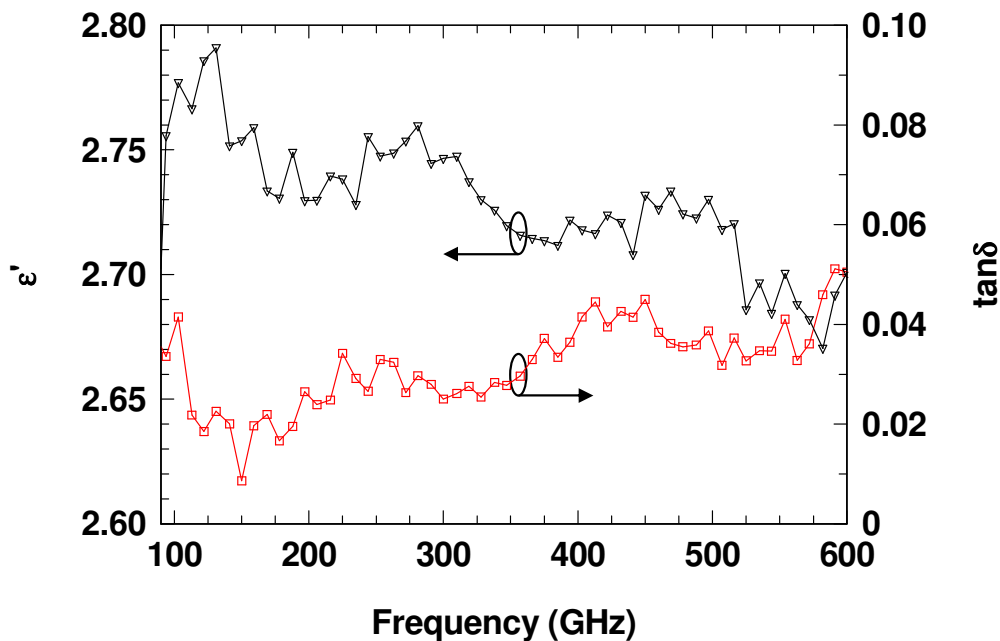


Figure 3-2. Polymer slab THz characterization results. The real part of the permittivity ϵ' (open triangle) is plotted with left ordinate, and the loss tangent $\tan \delta$ (open rectangle) is plotted with right ordinate.

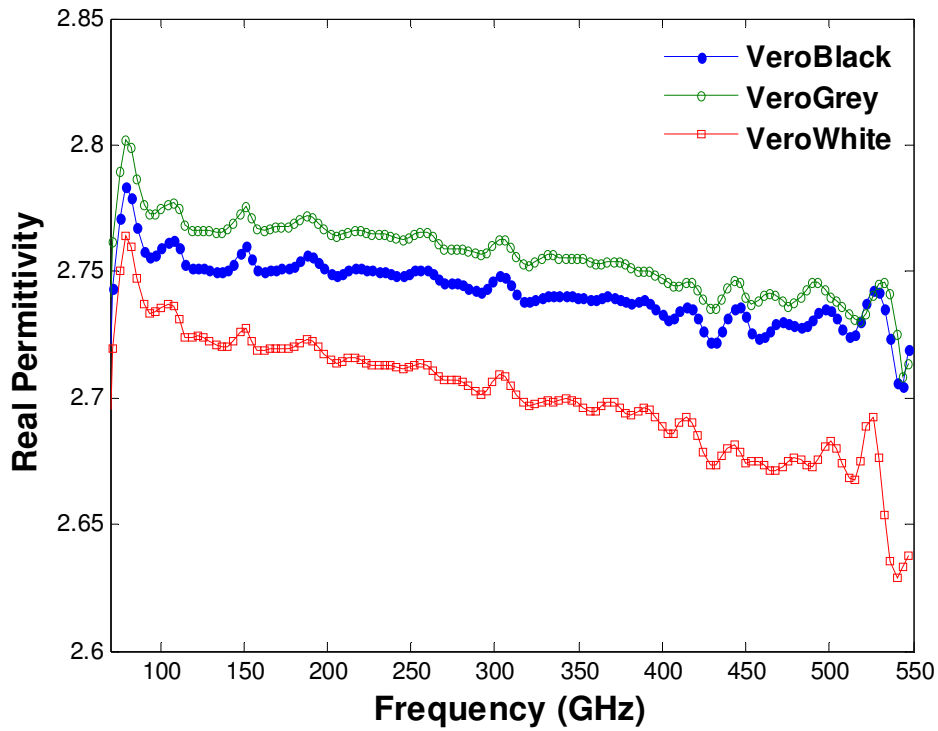
According to the above results, a refractive index ($n = \text{Re}(\epsilon^{1/2})$) contrast of around 1.66, with respect to the air background, is provided by the model material. With this refractive index contrast, periodic structures may exhibit EBG behaviors, although the band gap will not be as deep as EBG structures made of materials with larger refractive index contrast such as silicon ($n \sim 3.6$). The band gap may not be three-dimensional as well, meaning EM waves propagating along oblique directions may still travel through the EMXT at band gap frequencies.

There are several different polymer formulations available for this particular rapid-prototyping machine from the company. They are Vero Grey, Vero Black, and Vero White, named after their colors respectively. Figure 3-3 shows several images of artworks prototyped by these polymers.

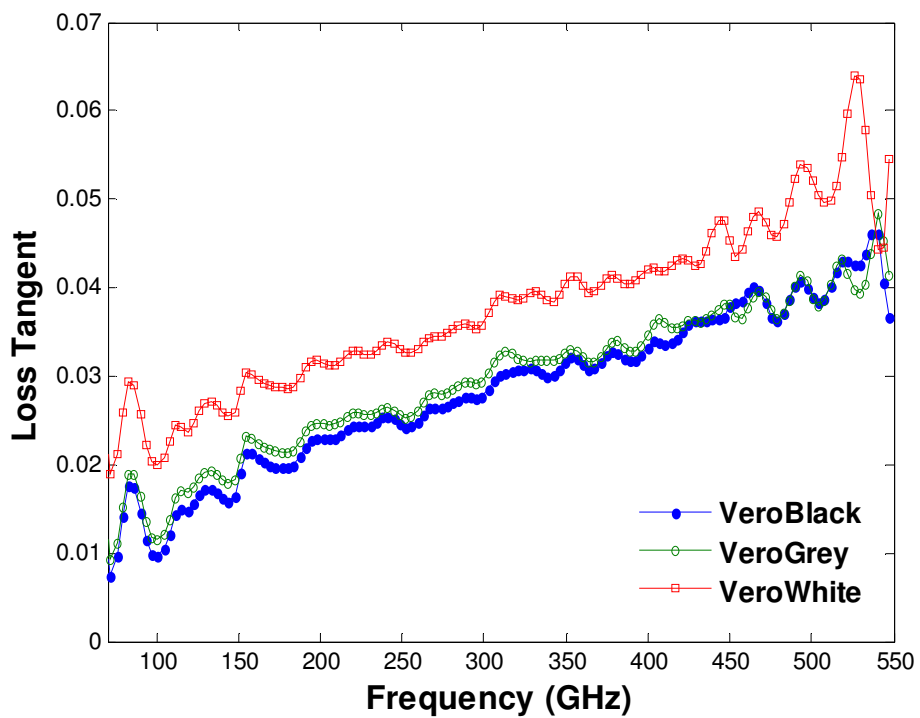


Figure 3-3. From left to right: artworks prototyped by Vero White, Vero Grey, and Vero Black polymers, respectively. Photo courtesy of Objet Inc.

The polymer measured above and applied for sample fabrications throughout this dissertation work is Vero Blue. The electromagnetic properties of these other polymer materials are also tested with the same experimental setup. Figure 3-4 below depicts their measured dielectric constants and loss tangents.



(a)



(b)

Figure 3-4. (a) Dielectric constants and (b) loss tangents of Vero Black, Grey, and White polymers, characterized by THz-TDS.

From the characterization results, it can be seen that all four Vero polymers have similar dielectric properties. They all show a dielectric constant of around 2.75 from 100 to 500 GHz, decreasing as the frequency goes up. This is expected because they all belong to the same family of polymers, which also means that there will not be enough refractive index contrasts among these build materials. As typical dielectrics, their loss tangents all increase as the frequency ascends, among which the Vero White exhibits the largest material loss as well as the smallest dielectric constant. Therefore it is the last build material one would like to pick to fabricate the EMXT components.

3.3.2 Woodpile Structure

The first EBG structure we tested is the well-known woodpile structure (WPS) with a complete 3D band gap [148]. A schematic representation of the WPS has been shown previously in Figure 2-1, together with a detailed description of the structure at the beginning of Section 2.2.

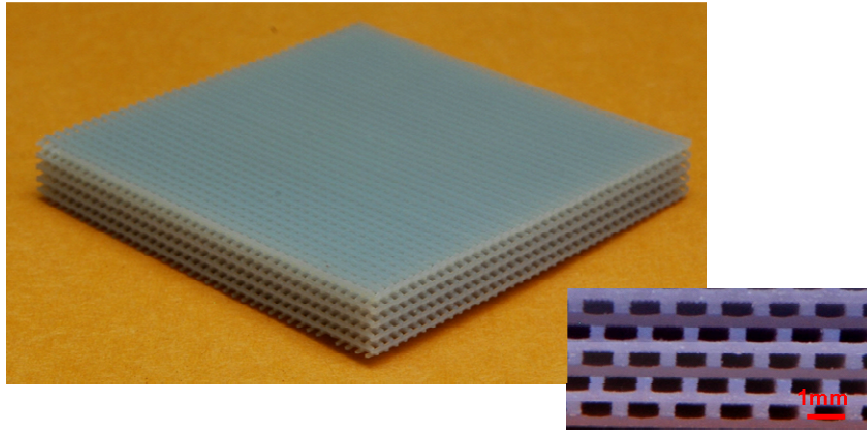


Figure 3-5. Photographs of the fabricated polymer THz WPS. Inset is a zoomed-in view of the sample cross-section.

Using the previously-measured electromagnetic properties of the model material, we designed a WPS structure so that the band gap was positioned at 185 GHz. Figure 3-5 shows a photograph of the fabricated polymer WPS. It has a rod dimension of $w = h = 352 \mu\text{m}$ and a periodicity $d = 1292 \mu\text{m}$. In the stacking direction, it consists of five unit cells (20 layers of rods). The transverse area is sufficient to fully cover the incident beam of the THz-TDS at its beam focal point. The inset of Figure 3-5 is a zoomed-in view of the sample cross-section. Clean, sharp feature edges are clearly visible and match the structure shown in the schematic.

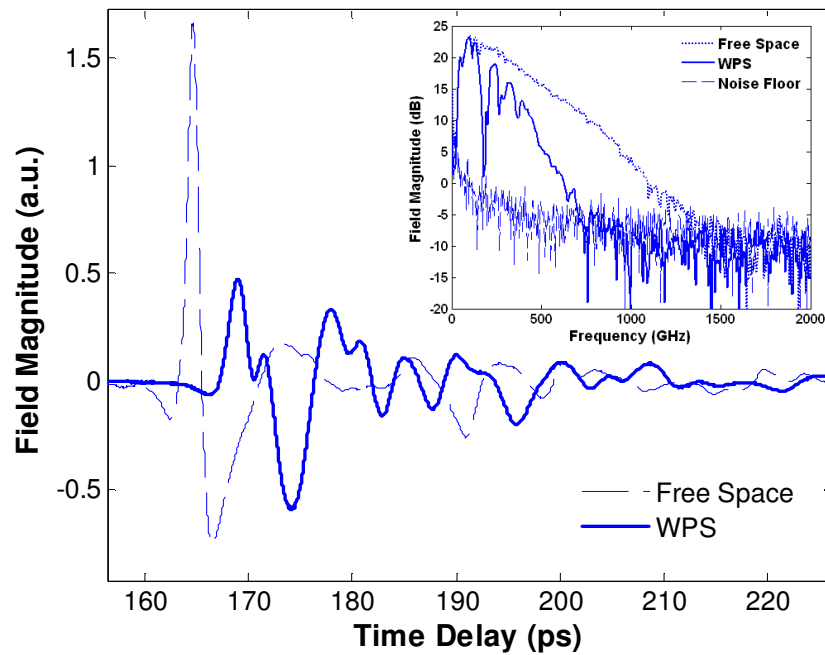


Figure 3-6. THz-TDS measured free space signal waveform (dashed) and the WPS sample transmitted waveform (solid). Inset shows the frequency domain signals of the sample (solid), the free space (dotted), and the experiment noise floor (dashed).

The transmission response of the fabricated polymer WPS sample is then measured with the THz-TDS, with the incident energy propagating along the stacking direction ($\langle 0\ 0\ 1 \rangle$ in the schematic of Figure 2-1). The transmitted waveform is recorded and plotted as the solid line in the main portion of Figure 3-6. The dashed line in the main portion of Figure 3-6 is the time domain signal of the waveform through free space (with the EBG sample removed from the beam path). The decaying resonances introduced in the periodic structure of the WPS can be clearly seen. The inset of Figure 3-6 plots the Fourier transformed transmitted signal spectrum of the pulse through free space (dotted) and through the WPS sample (solid). In addition, the experiment noise floor (dashed) is also plotted. The noise floor is measured by completely blocking the incident pulse with a metal plate placed in front of the

THz-TDS receiver head. The noise floor is important since it indicates the dynamic range and the usable frequency range of the measurement results [149]. From the measured sample transmission and noise level, the WPS sample response is valid from 50 GHz to 600 GHz.

The WPS power transmittance spectrum is then obtained by taking the ratio of the frequency domain signals between the WPS and free space and the result is plotted in Figure 3-7. We see that the fabricated polymer WPS exhibits a fundamental EBG at around 180 GHz, with a band rejection of more than 35 dB. The secondary and tertiary band gaps at 278 GHz and 372 GHz, respectively, are also observed in the measured power transmittance. Using -15 dB as the criteria of band edges, the sample has a main EBG bandwidth of 48 GHz. Its full bandwidth to mid-gap frequency ratio $\Delta f / f_0$ is therefore around 26.7%. The measured EBG performance qualifies this polymer WPS as a good band pass / stop filter.

As a comparison to the measurement, the same WPS is simulated with the full-wave finite-element electromagnetic solver HFSS [124]. For the purposes of the simulation, the polymer material is modeled as a pure dielectric with $\epsilon' = 2.76$ and $\tan\delta = 0.06$. We used a loss tangent that is slightly higher than the maximum observed value of 0.05 (as shown in Figure 3-2) so that the material loss would not be underestimated in the simulation. The WPS normal-incidence power transmittance from 100 GHz to 450 GHz is simulated and the result is also plotted in Figure 3-7 as the solid line. We observe excellent agreement between measurement and simulation. Not only is the fundamental band gap (centered at 185 GHz) verified, but a small

resonance near 202 GHz can also be consistently seen in both the simulated and the measured results. Moreover, the simulated and measured secondary and tertiary band gaps (centered at 278 GHz and 372 GHz, respectively) are in very good agreement in terms of location, width and depth. The small (< 2 dB) discrepancy of the transmission level at the low frequency end between the simulation and the measurement is a result of the overestimation of the material loss. As previously mentioned, the simulation assumes a loss tangent of 0.06, while the measured loss tangent near 100 GHz is approximately 0.02. The overall excellent consistency between the measurement and the simulation results confirms the fabrication accuracy of the polymer jetting technique for this woodpile structure.

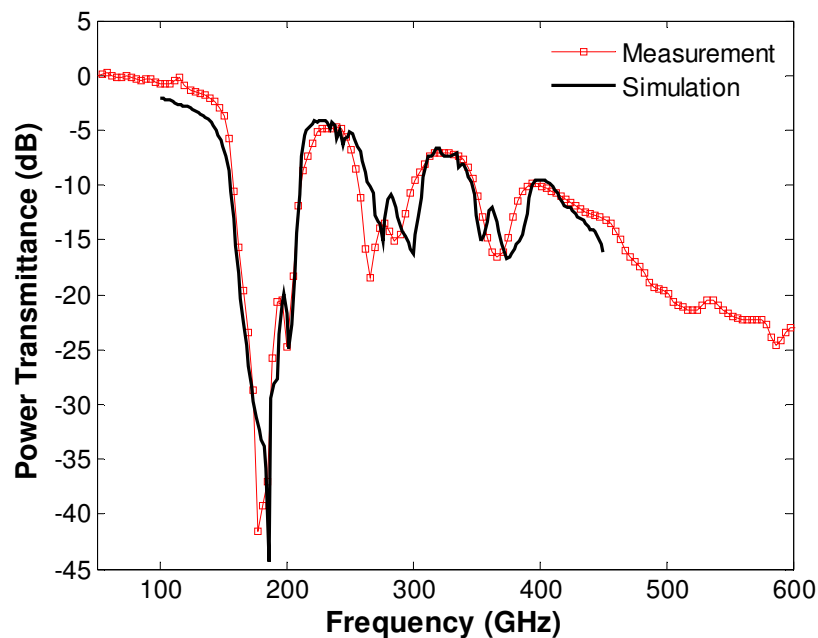


Figure 3-7. Comparison between the measured (open squares) and simulated (solid line) WPS normal-incidence power transmittances.

3.3.3 Johnson Structure

The second EBG structure we test is a much more complicated three-dimensional band gap structure first proposed by Johnson and Joannopoulos [150], and later fabricated by the same group at IR frequencies [151]. We refer to this as the “Johnson-structure” (JS). A computer rendered structure model is shown in Figure 3-8 (left). The structure consists of two alternating 2-D triangular lattice layers, one being pseudo-hexagonal dielectric pillars standing in air (rod layer) and the other being air holes in dielectric (hole layer). Each air hole has a radius r , and the size of each dielectric pillar is defined by the three surrounding air holes. The rod and hole layers have the same lattice constant x . The adjacent rod (hole) layers are shifted from each other by $x/\sqrt{3}$ in the x direction, thus forming the ABCA sequence in the stacking z direction as shown in Figure 3-8 (lower right). The structure unit cell therefore includes three rod layers and three hole layers in the stacking direction. Figure 3-8 (upper right) shows the cross section of the structure: the height of the through air holes is h , and the height of two touching layers (one hole layer and one rod layer) is t . The omni-directional band gap of this structure has a scalable center frequency with the above parameters, among which the air hole radius is the primary determinant of the gap bandwidth [80].

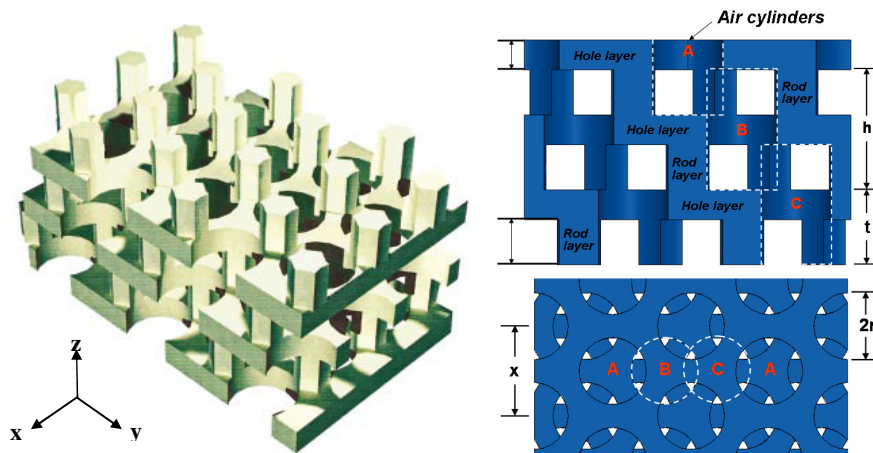


Figure 3-8. Schematics of the Johnson EBG structure, including: a 3-D model (left) showing one unit cell in the stacking direction and several periods in the horizontal direction (from [150]), the cross-sectional view (upper right), and the top view (lower right).

In this trial, we take the dimensions of the original fabricated sample (designed to work at optical frequencies in [151]) and scale them to THz region. The resulting THz JS has the following dimensions: triangular lattice constant $x = 1346 \mu\text{m}$, air hole radius $r = 500 \mu\text{m}$, air hole height $h = 1713 \mu\text{m}$, and rod / hole layer height $t = 1071 \mu\text{m}$. Based on the results in [151], the structure is expected to exhibit a band gap around 200 GHz.

A photograph of the fabricated JS is shown in Figure 3-9, left. A top and a side microscopic view of the structure are also included in Figure 3-9, right. In the top view (lower right), the hexagonal air hole array is clearly defined, and lower shifted hole layers are observed. A design choice results in the posts having truly circular cross-sections, but this is not expected to dramatically impact the EM behavior of the structure [150]. The shifted adjacent rod layers are also correctly fabricated, as can be seen in the side view. Three unit cells including 9 hole layers and 9 rod layers in the

stacking direction are fabricated, resulting in an overall EMXT dimension of 25 mm x 25 mm x 9.6 mm.

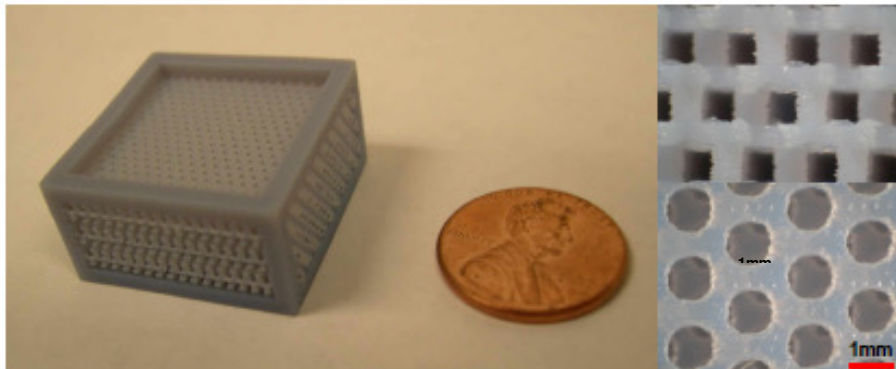


Figure 3-9. Photographs of the fabricated polymer Johnson EBG structure, including: the full view (left), the side (cross-sectional) view (upper right), and the top view (lower right). Clearly defined air hole and dielectric rod layers are observed.

Same as the WPS structure, THz-TDS is used to measure the normal-incidence transmission properties of the JS. The sample power transmittance spectrum is measured and plotted in Figure 3-10. A larger loss through this thicker sample (compared with the WPS) results in smaller transmitted signals. As a consequence, the noise floor becomes significant at frequencies above 350 GHz. As such, we limited our analysis to the 50—350 GHz region. A fundamental band gap centered at 223 GHz is clearly observed, with a band rejection of around 25 dB, and a full bandwidth to mid-gap frequency ratio of 15.4%. The structure also exhibits a smaller transmission dip at 117 GHz, with band rejection of less than 15 dB. We have also investigated non-normal incidence (specifically, along the x-direction of Figure 3-8). In this case, the measured transmittance (not shown) is very similar to the

normal-incidence results, showing a 117 GHz transmission dip and the fundamental band gap starting at around 200 GHz. This result partially confirms the expected isotropic property of the JS band gap even with the low-refractive-index polymer as the build material.

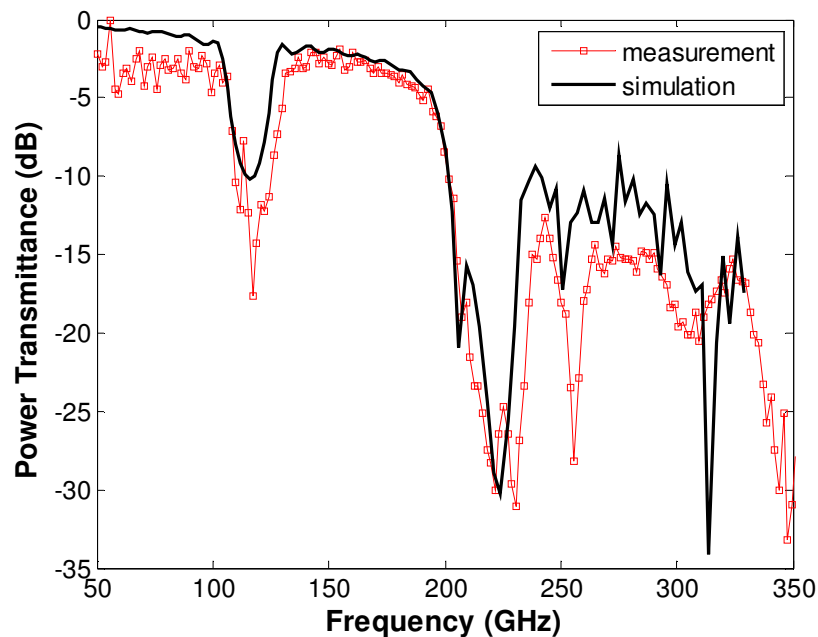


Figure 3-10. Comparison between the measured (open squares) and simulated (solid line) Johnson structure normal-incidence power transmittances.

As before, we simulate the JS with HFSS. The solid curve in Figure 3-10 shows the simulated normal-incidence, three-unit cell sample power transmittance from 50 GHz to 330 GHz. Both the mid-gap frequency and the gap rejection depth of the fundamental EBG around 220 GHz are verified. The secondary transmission dip around 120 GHz is also confirmed. Both gaps are slightly wider in the measurement than in the simulation, probably as a result of a small inhomogeneity of array pitches. The two additional transmission dips measured at 255 GHz and 309 GHz can also be

matched to features in the simulated spectrum, although their correspondence is not as clear. The overall agreement between the design simulations and characterization results is significant. This once again demonstrates the capability of the polymer jetting approach to handle complicated THz structures.

3.3.4 Photonic Cavity Array

The same THz rapid prototyping technique is also employed to fabricate the photonic cavity array structure introduced in Section 2.2.2. The purpose is to not only manufacture the structure, but also explore the possibility of metalizing polymer components at desired locations. A box side length of $150\ \mu\text{m}$ has been applied. With refractive index of 1.66 available from Vero Blue, the resonance frequency of the fundamental mode would be around 852 GHz according to Equation (2.5).

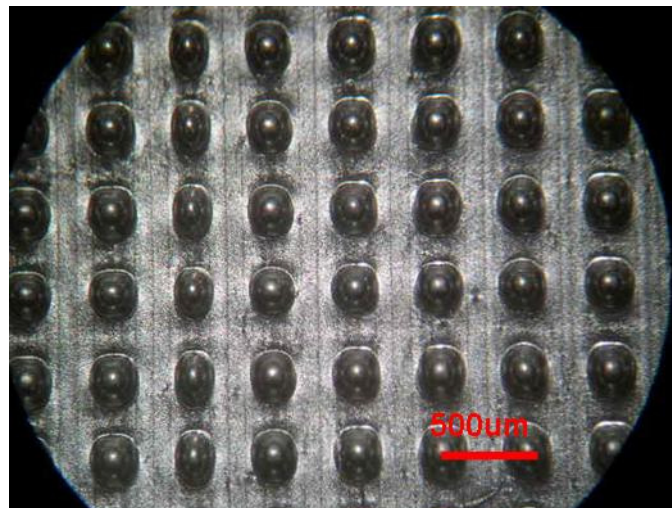


Figure 3-11. Photo of the photonic cavity array sample fabricated by THz rapid prototyping and then metalized via sputtering.

In order to prepare the best surface smoothness for the next step of metallization, glossy mode is chosen when printing the box array. After the prototyping, polymer box array sitting on a polymer substrate is sputtered on a layer of Titanium of 100 nm thick. Sputtering is a process intended for 2-D circuit metallization. However since the box height is only 150 μm , we still hope metal would be sputtered onto the box sidewalls as well. An SEM image of the fabricated sample is shown in Figure 3-11. Instead of cubic boxes, we obtained hemisphere shaped boxes in the final sample. This could be possibly due to two reasons: first, because of the lack of support materials in glossy mode printing, the droplets of the liquid polymer jetted out of the printer head spread on the substrate and formed the hemisphere shape; second, the sputtering process would cause a temperature increase of up to 100 degree Celsius on the sample surface. According to the data sheet from the company, Vero Blue has a deformation temperature of only 48 $^{\circ}\text{C}$, meaning the polymer boxes may be melted down in the sputtering step and transformed into the hemisphere shapes. The first cause could be eliminated in future fabrication by printing the structure under matt mode, whereas the second cause would only be circumvented by metallization through other processes, such as electroplating [152, 153] and electro-less deposition [94, 95, 154]. Also, shown in the SEM image is that the third column counting from the left has an apparently smaller printed box width comparing with other columns, implying that a certain error occurs when prototyping that column. The metallization via sputtering is a success though, with SEM images

showing Titanium on both top surfaces and sidewalls of the boxes. A long-lasting good adhesion between the polymer and the Titanium layer is obtained as well.

3.4 Conclusion and Future Work

In this chapter, we have successfully used a polymer jetting technique to fabricate high-quality 3-D THz EMXT structures. THz-TDS characterizations of the fabricated WPS and JS structures show very good correspondence with EM simulations, confirming the high dimensional accuracy and geometric complexity achievable by this fabrication technique at THz wavelengths. The speed, convenience, flexibility, scalability and low-cost nature of the technique make this methodology highly promising for manufacturing future THz micro-systems. Attempt to deposit metal onto the prototyped sample surfaces via sputtering also yields promising results in terms of the adhesion between polymer and metal. Therefore metallic termination is achievable when it is demanded in the prototyped component or system. However, metallization processes other than sputtering need to be explored in order to avoid the high-temperature deformation problem with the polymer as well as to deposit thicker layer of metal (i.e., several microns) onto surfaces of arbitrary 3-D prototyped shapes.

Now that we have the approach to fabricate arbitrary THz EMXT components, the next question to consider is whether we can realize most of the THz components mentioned in Section 3.1 with this fabrication technique. The answer is yes. An EMXT structure itself is a good filter and Bragg reflector at its band gap frequencies.

We will demonstrate the realization of wave guiding structures via this prototyping technique in the next chapter, as well as proposed designs and simulation results of THz EMXT antennas and transitions to planar circuits in Chapter 5.

In addition, an effective medium is a sub-wavelength concept in contrast to an EMXT, since its unit cell size is much smaller than one half of the working wavelength as in the case of an EM crystal. The prototyping method however, is still capable of fabricating these small unit cells and, therefore, it can be used to realize a THz effective medium. This may open up interesting applications such as artificial anisotropy and THz wave-front control [91], as well as a gradient index antenna for THz far-field pattern manipulation [56].

There are also possibilities to mix different printing materials such as conducting polymers and magnetic polymers during the prototyping, so that specified spatial distribution of material properties could be achieved. If micro-fluidic channels are integrated into the printed EMXT structure, liquid crystal can then be infiltrated into these channels to make the working frequency of the structure tunable.

Once all these building blocks with different functionalities are proven to be manufacturable with the prototyping technique, integration of the components via the same fabrication technique would yield a completely packaged THz micro-system. Further investigations of these concepts are currently underway in our lab.

CHAPTER 4. THZ WAVEGUIDE BASED ON HOLLOW-CORE EMXT FIBER

In the previous chapter, we have demonstrated the capability of THz rapid prototyping to fabricate THz structures of arbitrary shapes. THz filters and Bragg reflectors can be realized directly from THz EMXT structures fabricated by this technique. The next important component to explore is the THz waveguide since it delivers energy over a distance while keeping the integrity of the signal intact. In this chapter, all-dielectric THz waveguides are designed, fabricated and characterized. The design is based on hollow-core electromagnetic crystal (EMXT) waveguide, and the fabrication is implemented with the polymer-jetting rapid prototyping method. Measurement results of the waveguide power loss factor show good consistency with simulation. As an initial example, a waveguide with a low propagation loss, 0.03 dB/mm at 105 GHz, is demonstrated. Several design parameters are also varied and their impacts on the waveguide performance are investigated theoretically.

4.1 Background and Motivation

The large growth of THz technology in recent years is driven by scientific and engineering applications, with interest from various fields including chemical and astronomic spectroscopy and sensing, medical and biological imaging and analysis, defense and security screening, communication networks and radars, etc [21]. Many of these applications are based on free-space propagation, however, resulting in weak

beam confinement and vulnerability to environmental fluctuations. The focal spot size is diffraction limited and relatively large as well [155], which inconveniently requires large sample area in material characterization applications and makes the miniaturization of a system challenging. THz waveguides, on the other hand, provide a promising approach to overcome these drawbacks, and may lead to compact and low-cost integrated THz systems.

Various types of THz waveguides based on both electronic and photonic technologies have been proposed and studied, including metallic rectangular/circular waveguides [78], [79], parallel-plate waveguide [156], metal wire [157], [158], coaxial transmission line [159], plastic fiber [85], [155], [160], photonic crystal fiber [86]-[89], etc. However, the realization of a THz waveguide with acceptable performance is still a challenge in many aspects, including loss, cost, coupling, and especially fabrication and component integration. For most of the THz waveguides reported, as far as the fabrication is concerned, they usually involve either complicated photolithography or micromachining work flows [78], [79], [89], [156], or high-temperature and hazardous hot-draw or CVD processes [85]-[88]. A few of the demonstrated THz waveguides also need hand assembly work [86], [89], which compromises the fabrication accuracy and prohibits large scale production. Moreover, none of them has much flexibility when a certain modification of a section of waveguide (i.e., non-uniform cross section) or integration with other components is necessary.

In this chapter, an all-dielectric waveguide operating near 112 GHz is proposed based on a hollow-core electromagnetic crystal (EMXT) waveguide structure [4]. Both eigen-mode and driven-mode simulations are performed to verify the low waveguide transmission loss in the pass bands. Parametric study is conducted as well to explore the impacts on the waveguide performance from various design variables. Waveguide fabrication is done by the polymer-jetting rapid prototyping technique introduced in the last chapter [161]. Due to the layer-by-layer printing nature of this technique, the fabrication is convenient, accurate and highly flexible. Several waveguides of identical cross-section and various lengths are fabricated to enable THz Time-domain Spectroscopy (THz-TDS) characterization of its intrinsic power loss factor. Measurement results agree well with the simulation, exhibiting a power loss as low as 0.03 dB/mm at 105 GHz [162].

4.2 THz EMXT Waveguide Design

4.2.1 Design Procedures

The waveguide structure studied is based on introducing an air core defect into a triangular-lattice air-cylinder array in a dielectric background. Because of the Bragg diffraction in the lattice, this structure exhibits electromagnetic band gaps (EBGs) in certain frequency bands. Within the EBGs, wave propagation is prohibited and therefore the structure is able to confine the wave propagation. If a defect is present, this structure will support wave propagation along the defect channel at the band gap

frequencies, whereas the radiation loss along the propagation path will be greatly suppressed because of the EBG cladding. More importantly, the wave suffers much less material loss than in conventional optical fiber, because a majority of the power is confined within the hollow defect air core under the proper transmission mode(s) [4]. Therefore, this type of waveguides is quite promising to achieve low transmission loss.

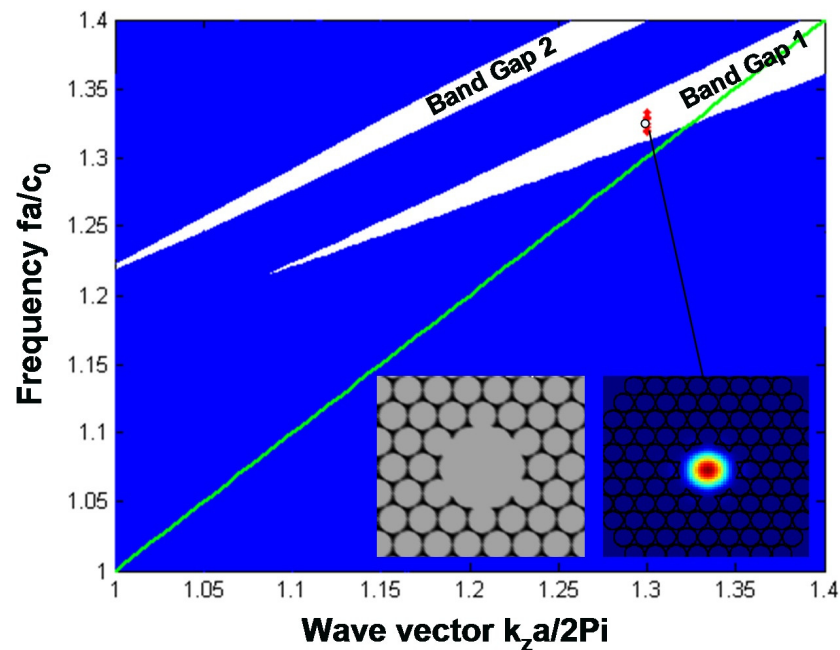


Figure 4-1. Band diagram of the complete EMXT structure and the defect waveguide modes. For the EMXT structure, dark (blue) regions denote the continuous modes region whereas in white regions no mode exists (band gaps). Inset (left) shows the schematic of the waveguide cross section when a center air core defect is introduced. Defect modes (waveguide modes) are marked by the dots (red) in the “Band Gap 1” region, among which the energy intensity profile of the fundamental HE_{11} mode is shown in the inset (right).

4.2.1.1 Eigen-mode Simulations

Figure 4-1 is an example of the band diagram of the complete EMXT structure and the defect waveguide, which is calculated using the MIT Photonic Bandgap package (MPB) based on the plane-wave expansion method [121]. Dark (blue) regions on the band diagram consist of continuous modes of the EMXT structure. White regions denote where no mode exists, therefore opening several band gaps. As shown in the cross-sectional schematic of the waveguide structure on the inset (left), a triangular-lattice arrangement of small air cylinders (grey) are embedded in the black dielectric background with dielectric constant of 2.75, while a large air-hole defect is present at the center. The cladding cylinders have a radius of $0.47a$, with a being the lattice constant, and the defect core has a radius of $1.4a$. This defect results in a few defect modes within each band gap of the complete EMXT structure, as denoted by the dots (red) in Figure 4-1. Note that only modes beyond the light line (green line) are capable of propagating. Since the band gap of the cladding rings suppresses energy from radiating out in the transverse directions, these defect modes support efficient energy confinement and propagation along the center core. The image on the right of the inset figure demonstrates the energy distribution of the fundamental HE_{11} mode within the first EBG, obtained from the eigen-mode simulation using the Lumerical MODE Solutions package [163] based on effective-index method. The MPB simulations revealed that approximately 91% of the energy is concentrated within the central defect for this propagating mode, and the closer to the center the higher the power density is. The energy intensity profile resembles a Gaussian

distribution so that this mode could be efficiently excited by an incident linearly-polarized Gaussian beam, according to field matching theory [164].

The waveguide design is completely scalable with frequency as the band diagram in Figure 4-1 illustrates. In the practical design reported here, a lattice constant of 3 mm is selected, which results in a center defect radius of 4.2 mm. The cladding air cylinder radius is slightly shrunk to 1.3 mm. Dielectric wall thickness at its thinnest place is 400 μm in this case, so that the structure has better mechanical robustness for this initial trial. The dielectric property of the polymer used in the rapid prototyping process is pre-characterized with the THz-TDS system. It has a dielectric constant of 2.75 and loss tangent of 0.02 near 150 GHz [161]. Using these properties, the simulated operating frequency of the fundamental HE_{11} mode is around 112 GHz. Although 5 periods of the cladding lattice is applied in the design, in general, 2 to 3 periods are sufficient for realizing low loss propagation as will be discussed in a later parametric study section. With these practical design parameters, the intrinsic radiation loss of the HE_{11} mode at 112 GHz (without considering the material loss) is calculated to be 0.012 dB/mm by Lumerical MODE Solutions.

4.2.1.2 Driven Model Simulations

In order to estimate the overall propagation loss of the waveguide design, including the material loss, effects from other higher-order modes and excitation efficiency, the waveguide is simulated under two different excitations, using a Finite-Difference-Time-Domain based package (GEMS [165]). The first excitation

employs two circular metallic (perfect electric conductor, PEC, is used here) waveguide feeds inserted into the dielectric waveguide apertures at both ends. Two wave ports excite the TE_{11} mode in the feeds, which then propagates through an 84-mm long EMXT waveguide.

Figure 4-2 depicts the resulting S-parameters [166]. Four pass bands are observed around 112, 130, 161 and 182 GHz, corresponding to the band gaps of the original EMXT structure. The field profile in the waveguide at 112 GHz resembles the desired HE_{11} mode as shown in Figure 4-1. The 3-dB bandwidth of the first pass band centered at 112 GHz is about 15.8 GHz, giving a full bandwidth to mid-gap frequency ratio of 14.1%. The reflection coefficient S_{11} is generally below -30 dB, indicating a very good coupling from the feeding TE_{11} mode to the EMXT waveguide modes. Once the S-parameters are obtained, the waveguide power loss factor can be calculated by the following equation

$$\alpha = \ln\left(\frac{|S_{21}|^2}{1 - |S_{11}|^2}\right)/(-l), \quad (4.1)$$

where l is the waveguide length.

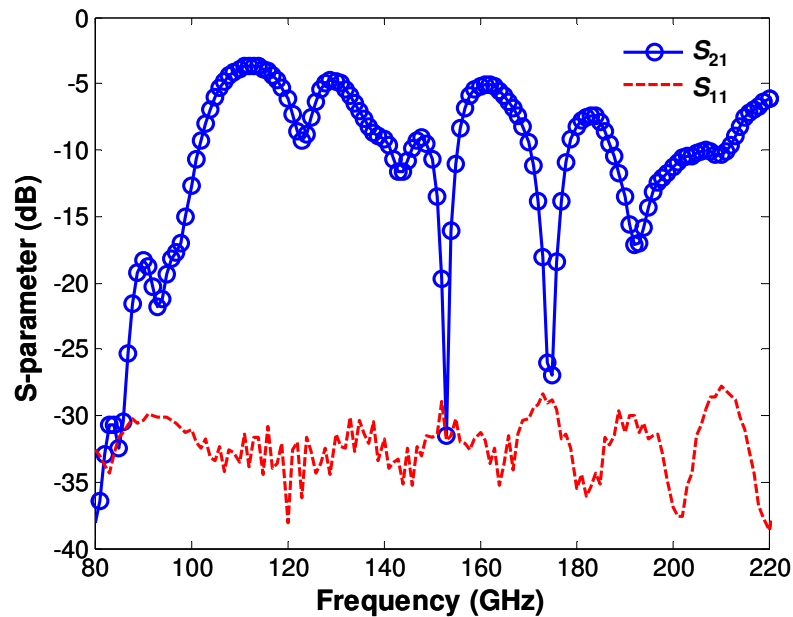


Figure 4-2. Simulated S-parameters of an 84 mm-long EMXT waveguide with lattice constant of 3 mm, center defect radius of 4.2 mm, and cladding air cylinder radius of 1.3 mm. The EMXT waveguide is fed by TE_{11} mode from circular PEC waveguide.

In a practical experiment, circular metallic waveguide feeds are inconvenient due to cost and issues in calibrating their losses. Instead, quasi-optical measurements using an incident THz Gaussian beam are preferred. A second set of simulations was performed for this configuration. In this case, a Gaussian beam with a 3-mm beam waist is aimed at the EMXT waveguide aperture, and the power flux transmitted out of the other end of the waveguide is calculated. The power flux calculation is done by integrating the Poynting vector component along the longitudinal direction, S_z , over a surface covering the cross-sectional area of the waveguide. Since the coupling coefficients at the input and output ends are identical and independent of the waveguide length, the transmitted power flux has an exponentially decaying relation with the waveguide length. A semi-log plot of the transmitted power flux (in dB)

versus waveguide length would then be a straight line with a negative slope, which is the intrinsic power loss factor of the waveguide. This conclusion, however, only holds when multiple reflections within the waveguide are excluded either via time-gating, or because they have negligible magnitudes. Time-domain gating is in principle not quite suitable for an EMXT waveguide, because it is a highly dispersive system with narrow band features. Its time-domain responses, therefore, decay very slowly. This behavior may make all the multiple reflection waveforms mix together so that they are hard to isolate from each other. Nevertheless, the assumption that multiple reflections have negligible magnitude may very well be true in our case, since the energy is incident from free space into the air core, and couples to those defect propagation modes with an effective refractive index very close to 1 (from Lumerical MODE simulation). Therefore, multiple reflections within the EMXT waveguide are neglected in our calculations.

Four waveguides with lengths of 100, 110, 120 and 130 mm are simulated under the same Gaussian beam excitation, and the transmitted power flux indeed shows an exponential decay relation with the waveguide length for the pass bands. The extracted waveguide losses using the above two simulation methods are compared in Figure 4-3. The two loss spectra show very good consistency in terms of frequency and depth of the low-loss bands. Out of the low-loss bands, the transmitted power in dB does not follow a linear relationship with the waveguide length, because no specific defect modes are associated with the energy propagation at these frequencies. This explains why most discrepancies observed in Figure 4-3 are located

at high-loss frequencies, i.e., 152 GHz and 176 GHz. The lowest propagation loss obtained is 0.022 dB/mm at 112 GHz. Therefore the material loss and potential losses from higher-order modes excited by the incident Gaussian beam bring in an extra 0.01 dB/mm of loss at this frequency, when compared to the eigen-mode simulation result of the fundamental HE_{11} mode in the last section.

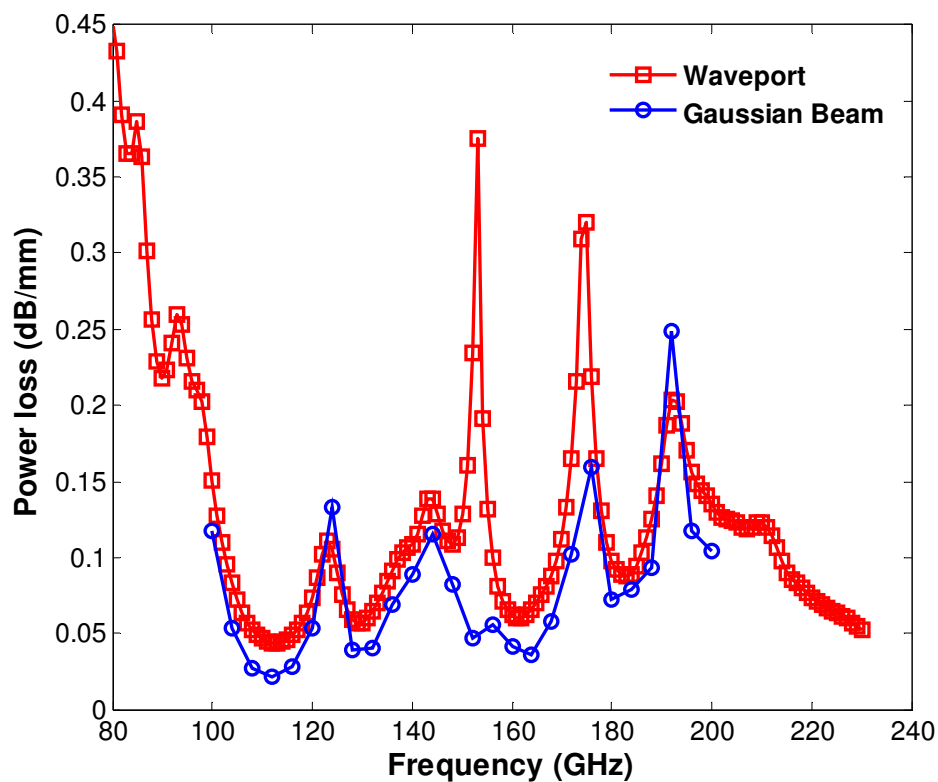


Figure 4-3. Power loss factors of the EMXT waveguide extracted from the wave-port (TE_{11} mode, circular PEC waveguide feeds) and the Gaussian beam (3 mm beam waist) incidence simulations.

4.2.2 Parametric Study of Design Variables

Several aforementioned design variables were subject to explorations of their effects on the EMXT waveguide performance, including the number of cladding rings,

waveguide length, defect core radius, build material loss, etc. Parametric simulations were carried out to study their impacts. To be computationally more efficient, the relatively simple wave-port excitation method was applied throughout the parametric study to calculate the waveguide losses via Equation (4.1). The radius of the cladding air cylinders as well as the triangular lattice constant were not included in this parametric study, therefore their values were kept the same as in Section 4.2.1, 1.3 mm and 3 mm, respectively.

4.2.2.1 Number of Cladding Rings

One cladding ring is defined as one hexagonal ring of small air cylinders surrounding the center defect core, and the counting of the number of rings starts from the center core edge. All other parameters are kept constant, for example, the waveguide is 84 mm long, the center core radius is 4.2 mm, and a constant conductivity of 0.459 Siemens/m (equivalent to a loss tangent of 0.02 at 150 GHz) is used as the material loss.

Figure 4-4 depicts the spectra of the waveguide power loss factor with 1, 2, 3, and 5 cladding rings. The plot reveals that two cladding rings would be enough to achieve low-loss transmission along the waveguide. Three and five cladding rings yield almost identical power loss factor in the four pass bands as the two-ring case, since the energy can not reach these positions because of the band gap effect. None of the pass bands is observed in 1-ring case, simply because there are not enough unit cells to form the EMXT structure.

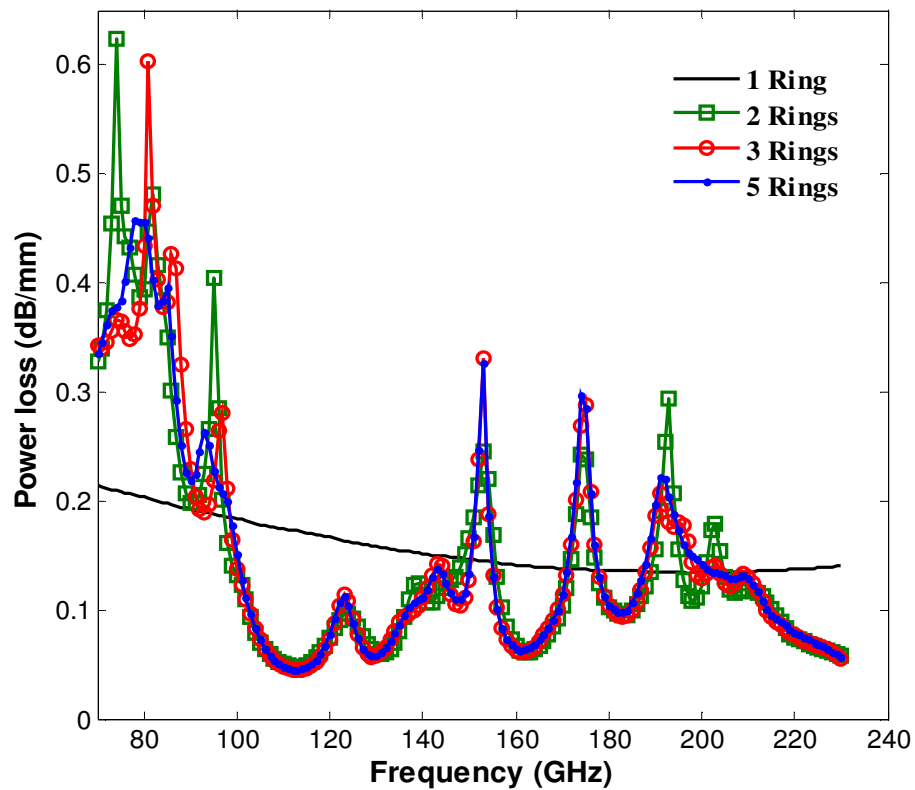


Figure 4-4. Spectra of the waveguide power loss factor for various numbers of air cylinder cladding rings.

4.2.2.2 Waveguide Length

During the sweep of the waveguide length, the defect core radius is kept at 4.2 mm with three cladding rings around it. Material loss is still approximated by the constant 0.459 Siemens/m conductivity as before.

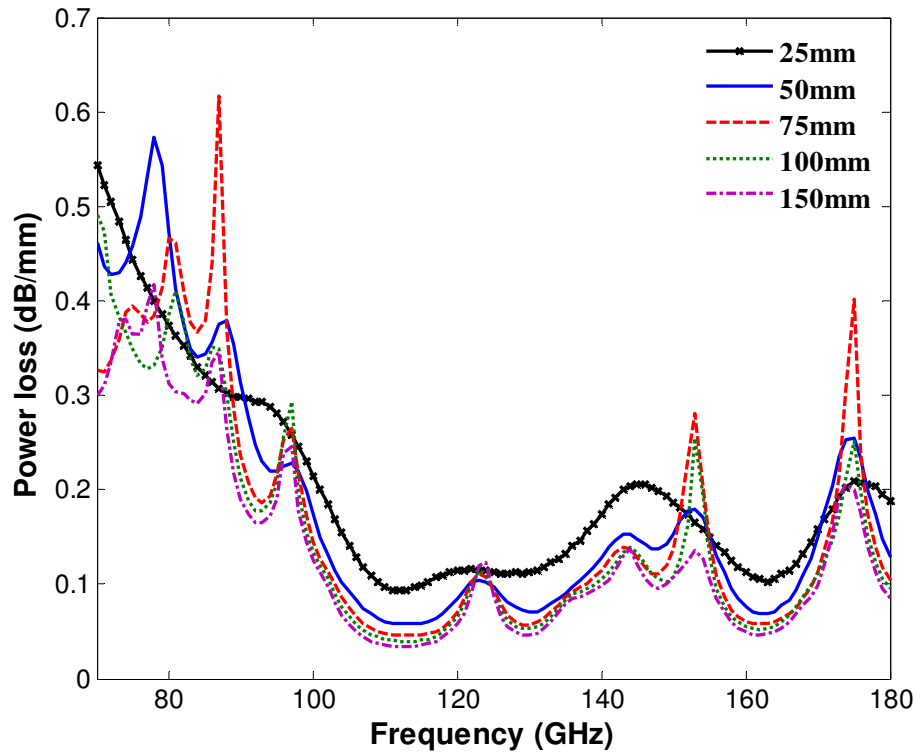


Figure 4-5. Spectra of the waveguide power loss factor for various waveguide lengths.

Simulation results of various waveguide lengths are plotted in Figure 4-5. The power loss factor exhibits a monotonic decrease as the waveguide length increases. A converging trend of the loss factor is observed when the waveguide reaches 75 mm in length. A 25 mm long (more than eight wavelengths for the 1st pass band) waveguide, however, is not enough for the low-loss band features to dominate. This is because a certain waveguide length may be necessary for the fundamental HE_{11} mode to fully establish itself over other propagating or evanescent higher-order modes which may also be excited by the circular PEC waveguide feeds. Those other modes, because of their larger transmission losses, eventually decay along the propagation path and the HE_{11} mode with lowest loss becomes dominant. The converging trend seen as the

waveguide length increases can also be explained by this effect, as the other modes are eventually purged and the overall power loss factor approaches that of the fundamental mode.

4.2.2.3 Defect Core Radius

A defect core provides the channel where the EM wave travels along, and therefore its size directly decides how much the fields interact with both the cladding of the EMXT structure and the build dielectric material. Our first defect radius sweep is carried out with 0.5 mm step for an 84-mm long waveguide with three cladding rings and 0.459 Siemens/m constant conducting loss.

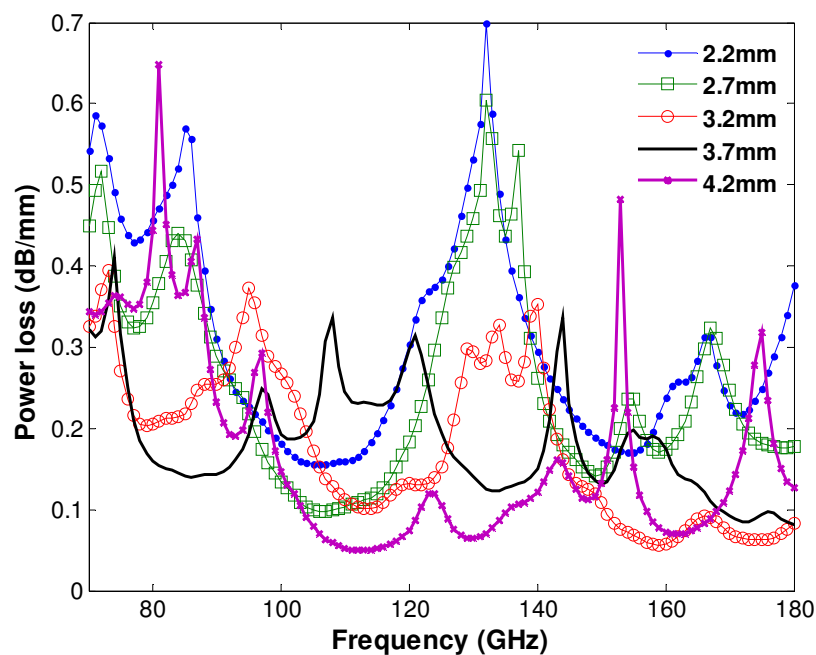


Figure 4-6. Spectra of the waveguide power loss factor for various defect core radii.

As seen in Figure 4-6, a variation of defect core radius changes not only the power loss factor values, but also the pass band frequencies. With a large core radius, higher order modes that can be excited by the incident TE_{11} mode are involved in the power transmission. These modes show up at different frequencies, therefore shifting both the center frequency and the bandwidth of the low-loss bands. Among the radii swept, 2.2 mm, 2.7 mm and 4.2 mm cases exhibit similar pass bands between 100 and 120 GHz. The observation is that a larger defect core leads to a smaller power loss factor, in company with a pass-band center frequency increase.

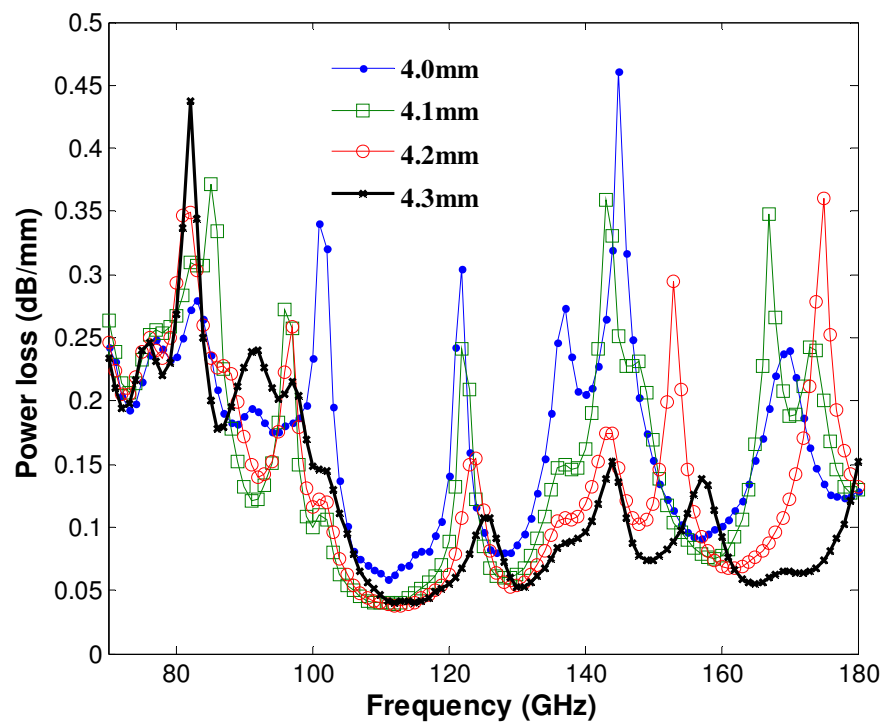


Figure 4-7. Spectra of the waveguide power loss factor for various defect core radii around 4.2 mm, with constant loss tangent used to describe material loss.

Since the 4.2-mm radius waveguide seems to have the best performance, another defect core radius sweep is done around 4.2 mm, with a smaller step (0.1 mm)

of variation. Because the core radius also affects the center frequency of the low-loss bands, a constant loss tangent material-loss model would be more appropriate for a fair comparison than the constant conductivity model which is inversely proportional to the frequency. A constant loss tangent of 0.02 is then applied in this parametric study. The results, as shown in Figure 4-7, yield similar pass band features around 112, 130 and 160 GHz (add explanation of why only 3 pass bands here). It can be observed that larger core radius results in a smaller power loss factor, a broader bandwidth, and a higher pass band center frequency. Moreover, this trend is more obvious in the higher-frequency pass band than in the lower-frequency pass band.

4.2.2.4 Build Material Loss

Power loss due to damping from the build material depends on how much field penetrates and interacts with the dielectric wall of the channel. The fact that the fundamental HE_{11} mode has over 90% of the energy concentrated in the air core area makes the power loss factor under this mode the smallest and least-dependent on any material loss. On the other hand, higher order modes with less energy confinement should show more dependence on the material loss. This is very much the case as the simulation results in Figure 4-8 will reveal. Again, all other parameters are kept the same for this parametric study, for example, 4.2 mm defect radius, 3 cladding rings, and a length of 84 mm. The material loss tangent $\tan\delta$ is varied and the waveguide power loss factor is calculated from the simulated S-parameters. Keep in mind that a waveguide filled with dielectric medium in general has a power attenuation factor

proportional to $(\tan\delta)^2$ [166]. However with power mainly traveling in the air defect, this waveguide design is expected to show much smaller dependence on the build material loss tangent.

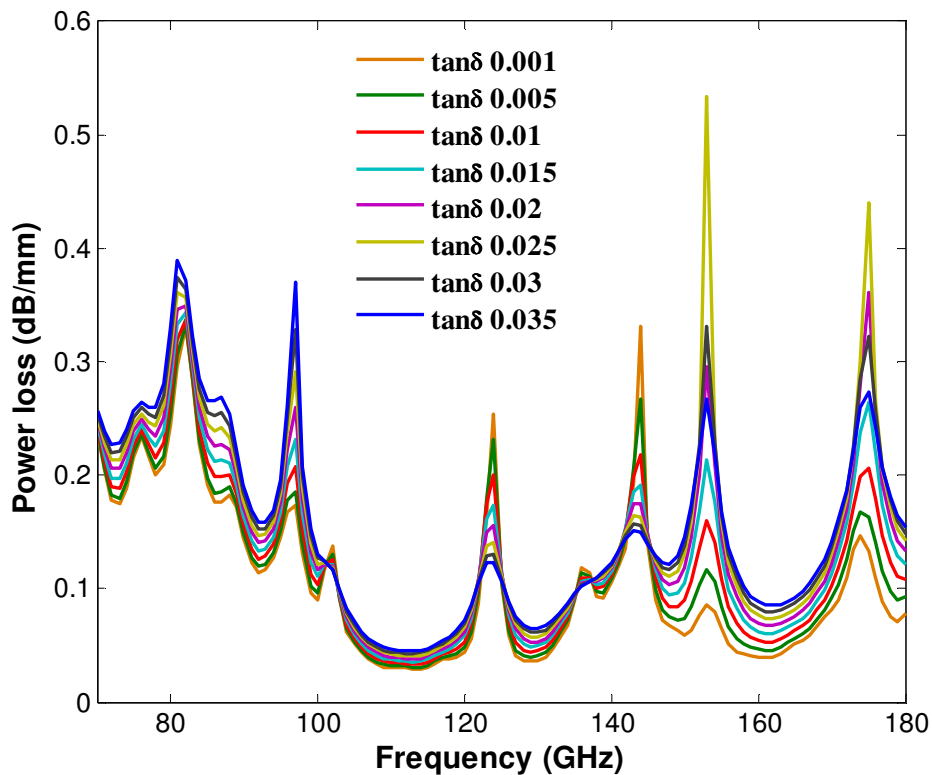


Figure 4-8. Spectra of the waveguide power loss factor for various material losses.

As expected, results in Figure 4-8 show a strict ascending order of the power loss factor in the three pass bands as the loss tangent increases. The center frequencies of the three lowest-loss pass bands are 113, 129 and 161 GHz. It is clear that the pass band at a higher frequency has a stronger dependence on the material loss tangent, since more higher-order modes are involved at higher frequencies. As the semi-log plot of the power loss factor (in dB/mm) versus the loss tangent was considered at

each of the three frequencies, and it is found that the resulting curves can be well fitted to a straight line. Figure 4-9 shows the example at 113 GHz. The slope of the fitted line for the EMXT waveguide at 113 GHz is 0.4624, thus the power loss factor is proportional to $(\tan\delta)^{0.4624}$ at 113 GHz. The fitted slope is 0.9582 and 1.376 at 129 GHz and 161 GHz, respectively. Therefore, this EMXT waveguide suffers more from the material loss in the pass band at higher frequency, probably due to the existence of higher order modes. Nevertheless, all three slopes are indeed smaller than 2, showing less build material loss dependence than the corresponding dielectric filled waveguide.

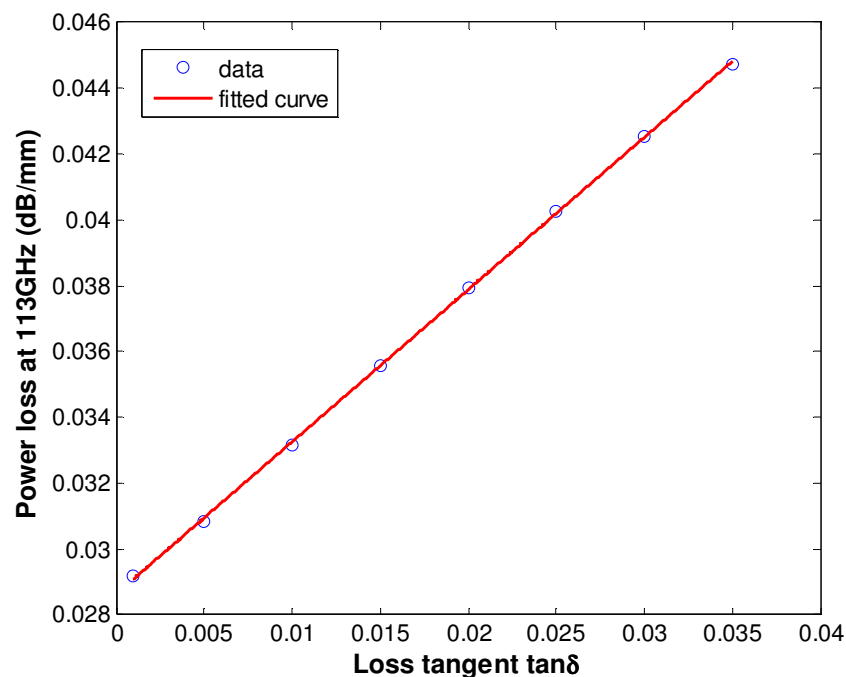


Figure 4-9. Linear fitting of the power loss factor (dB/mm) as a function of $\tan\delta$ at 113 GHz.

4.3 Experimental Characterization of the Waveguide Loss

Fabrication of the waveguide is done by the polymer jetting rapid prototyping technique introduced in Chapter 3. The structure is printed vertically along the wave channel direction. In this case, the glossy printing technique without support material is applied to achieve better surface smoothness, since the support material is not necessary for this structure. Figure 4-10 shows photos of the cross-sectional and a full view of a fabricated waveguide.

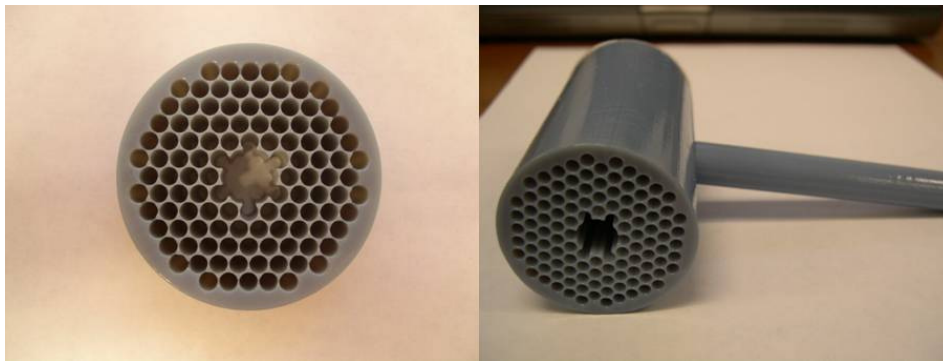


Figure 4-10. Cross-sectional and full views of a fabricated THz waveguide, with lattice constant of 3 mm, center core radius of 4.2 mm, and cladding air cylinder radius of 1.3 mm.

A THz time-domain spectrometer (THz-TDS) utilizing photoconductive antennas as the transmitter and receiver [56] is applied for the waveguide characterization. The antennas used in this work provide usable spectral content from 50 GHz to 1.2 THz and peak around 100 GHz. Two off-axis parabolic mirrors with 152.4 mm effective focal length converge the incident beam from the transmitter to about a 5.4 mm beam waist at the focal point. In order to efficiently convert the

incident Gaussian beam to the desired HE_{11} waveguide mode, their electric field profiles need to be matched [164]. According to the modal field overlap calculation [163], an optimum beam waist of 2.7 mm would convert the Gaussian beam to the HE_{11} mode with over 90% efficiency. Therefore, a plano-convex polymer lens pair is designed and fabricated by the same rapid prototyping method to focus the beam further behind the original focal point. The curved side of the lens has a radius of curvature of 15.3 mm. When placed at the focal point of the off-axis parabolic mirror, the lens focuses the beam to a 2.7 mm waist size at 17.5 mm behind the lens planar surface.

Figure 4-11 shows a photo image of the quasi-optics layout of the waveguide characterization. Lens 1 is positioned at the focal point of the parabolic mirror 1, and 17.5 mm in front of the waveguide input end. Lens 2 is also 17.5 mm behind the waveguide output end, and 152.4 mm away from the second parabolic mirror. The circular aperture in the image is only for the purpose of marking the beam position and opens enough for the entire beam to go through. As discussed previously, waveguides of several lengths need to be measured in order to characterize the propagation loss factor, resembling the “cut-back” method used in an optical fiber loss measurement [167]. Therefore, the spacing between the adjacent parabolic mirror and lens, as well as the spacing between the adjacent lens and waveguide end, are kept the same throughout the measurements to provide an identical optical path except for the waveguide section.

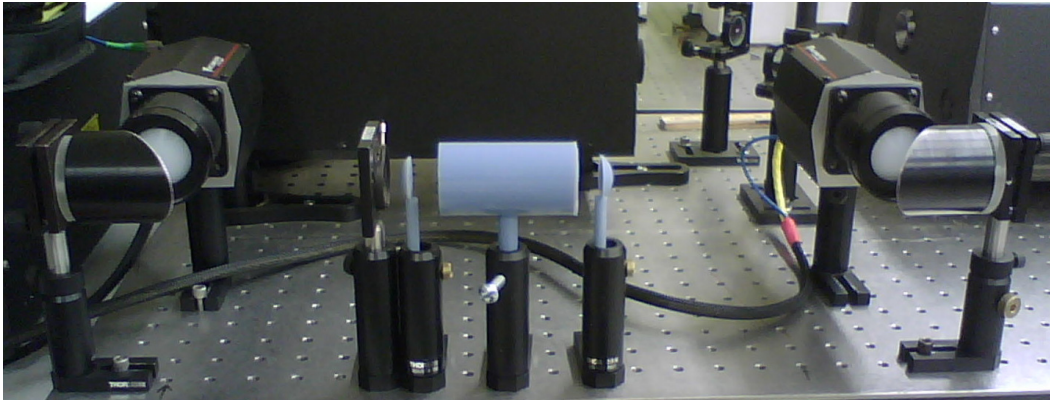
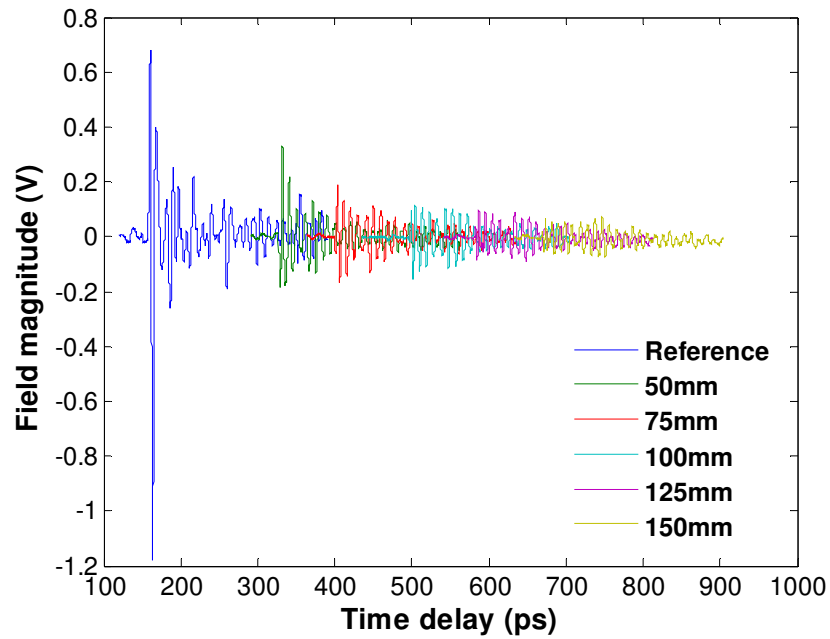
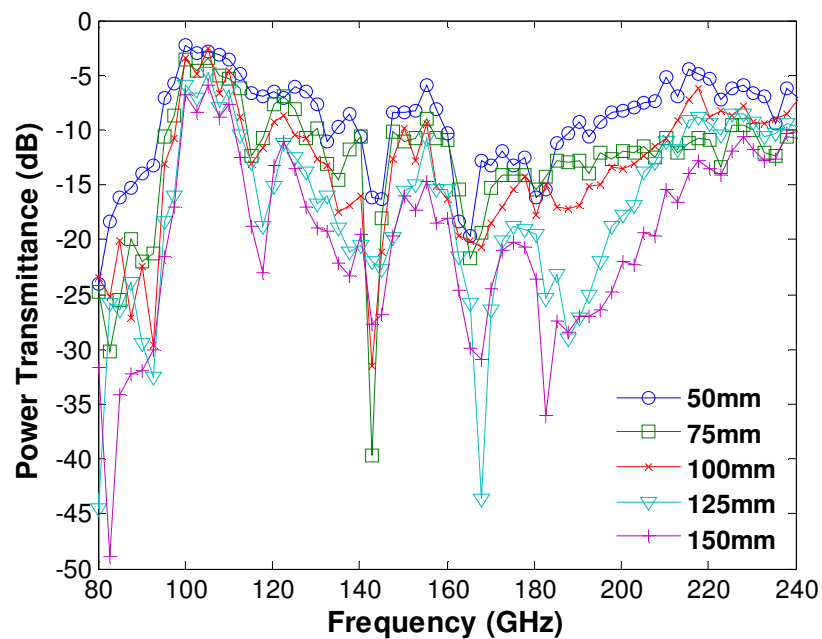


Figure 4-11. Setup of the characterization experiment: from left to right: THz transmitter, parabolic mirror 1, circular aperture, polymer lens 1, waveguide under test, polymer lens 2, parabolic mirror 2, and THz receiver.

Five waveguides of lengths 50, 75, 100, 125, and 150 mm and identical cross section are placed in the beam path, and their transmitted waveforms measured. The two lenses are also positioned 35 mm (17.5 mm x 2) away without a waveguide in between to obtain a reference scan. The recorded waveforms are shown in Figure 4-12(a). The reference scan is leading in time, followed by the five waveguide scans with more delays from the longer waveguides. Dispersions with respect to the reference waveform are observed in all five waveguide scans, which is a clear sign of guided mode resonances. Figure 4-12(b) plots the power transmittances of all the waveguides, which are obtained by Fourier transforming the waveforms to the frequency domain, then normalizing the spectra with respect to the reference spectrum. Four pass bands centered around 105, 123, 153 and 174 GHz can be clearly seen, corresponding to the four pass bands in Figure 4-2, despite a downshift of a few GHz.



(a)



(b)

Figure 4-12. (a) Transmitted waveforms of five waveguides with different lengths, and the reference scan transmitted through free space. (b) Normalized power transmission of the waveguides.

Extraction of the waveguide power loss factor is accomplished through the same linear fitting process of the transmitted power (dB) versus waveguide length

semi-log plot, as discussed in the previous section. Figure 4-13(a) plots the relative transmission power at 107 GHz, which is the center frequency of the first pass band. Except for a slight deviation from a straight line at the data point of 100 mm length, the transmitted power in dB decreases linearly as the waveguide length increases. The slope of 0.056 dB/mm is the measured waveguide power loss factor at this frequency. It is worth mentioning that the time span of the truncated waveforms utilized in Figure 4-12 is short enough so it is fully guaranteed that no multiple reflections are included in the calculation of the power loss factors. The truncation on the other hand keeps a long enough waveform so that the majority of the transmitted power is still kept in the calculation. As shown in Figure 4-13(b), the measured power loss factors agree quite well with the beam-incidence simulation results. The measured 7-GHz downshift is possibly due to fabrication tolerances, since the air cylinder diameter may not be precisely controlled due to the lack of support material under the glossy printing mode. Moreover, the model material has a slight dielectric constant dispersion from 2.8 to 2.73 within the 100-150 GHz range [161], which is not included in the simulations and contributes to the discrepancy too. Note that the dip at 143 GHz is not real because it is at a deep band-stop frequency, as shown in Figure 4-12(b), for which the signal-to-noise-ratio is not good. Nevertheless, the measurement and the simulation results agree well, demonstrating four pass bands with low propagation losses at close frequencies. The lowest power loss factor measured is 0.03 dB/mm at 105.2 GHz.

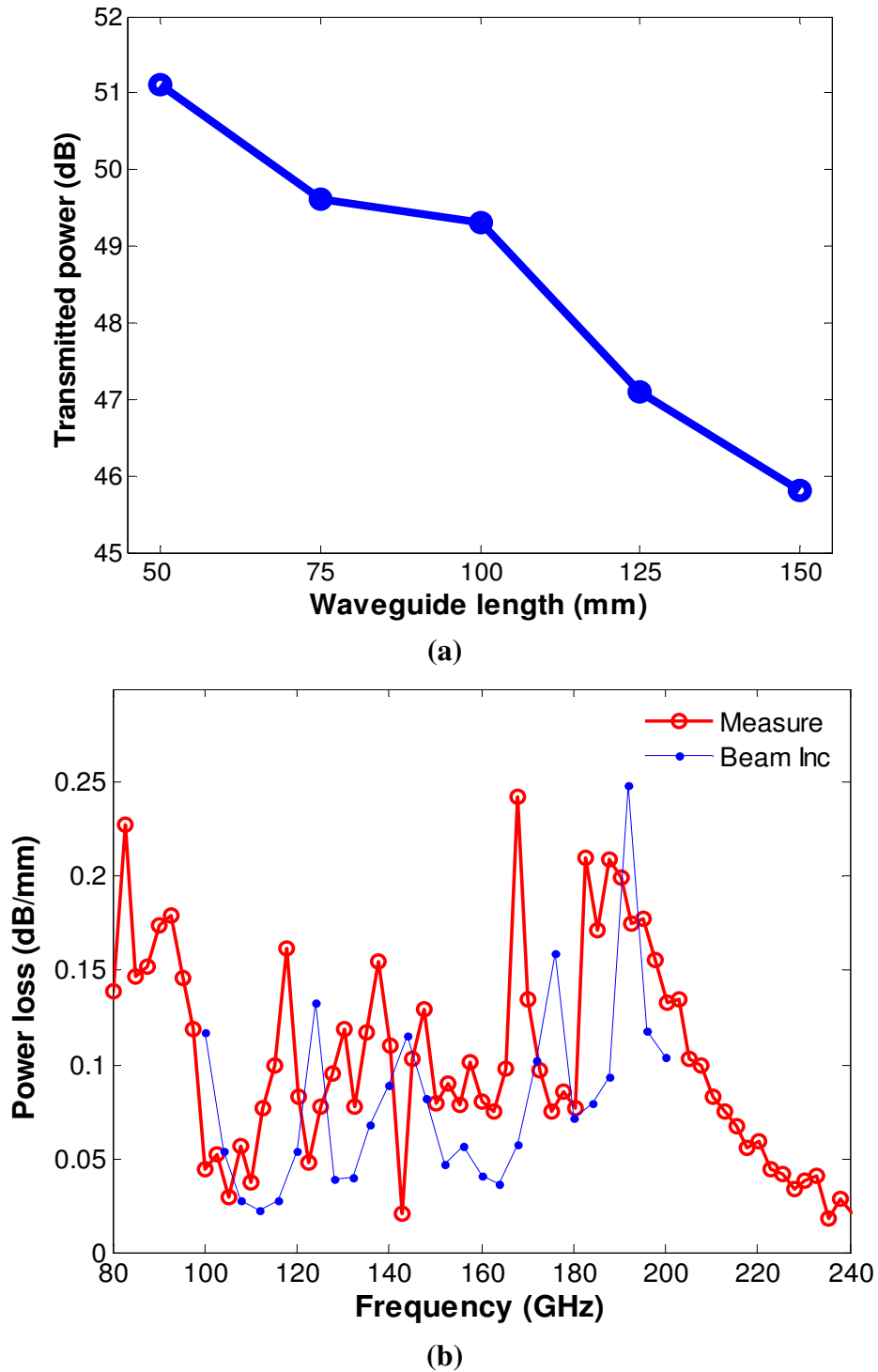


Figure 4-13. (a) Semi-log plot of the measured transmitted power in dB versus waveguide length at 107 GHz. Linearly fitted slope gives the power loss factor at this frequency. (b) Measured and simulated waveguide power loss factor, both excited by Gaussian beam incidence.

4.4 Conclusion and Discussion

A THz waveguide based on a hollow-core defect EMXT structure is designed and fabricated by polymer jetting rapid prototyping technique. Quasi-optical THz lenses are also fabricated by the same technique in facilitation of exciting the waveguide with the optimal beam waist size. Results of the waveguide power loss factor characterization show good agreement with the simulation. A low transmission loss waveguide around 105 GHz is achieved. Because of the systematic fabrication manner of the rapid prototyping technique, this waveguide can be readily integrated with other THz components and quasi-optics parts fabricated by the same approach, therefore leading to compact integrated THz micro-systems.

Parametric studies of several design variables of the EMXT waveguide are performed and their effects on the waveguide loss factor investigated. The study shows that two cladding rings are enough to achieve low propagation loss along the waveguide, therefore the waveguide cross section could be shrunk to a much smaller size than in the fabricated samples without affecting the performance. The waveguide length sweep reveals that a 50 mm length is necessary for the waveguide to exhibit low-loss transmissions, therefore this minimum length needs to be considered when delivering energy from one spot to another using this waveguide when designing the potential THz system. Also, larger center defect radius results in lower transmission loss, broader working bandwidth, as well as a center frequency up-shift of the low-loss bands. Thus, over an ascending center-defect radius range the resulting low-loss bands would overlap, and some common defect modes may very possibly

exist at these overlapping frequencies. This becomes the idea to build an EMXT horn antenna upon the same waveguide but with tapered center-defect radius in the next chapter. The last parametric study of the build material loss reveals a much weaker dependence on the material loss tangent for the waveguide loss, when compared to a general waveguide filled with dielectric. This is simply because the energy is concentrated in the air defect region of the waveguide and only a very small portion of fields exists within the build material.

Another interesting question to think about is how to transit the energy within this waveguide to a THz planar circuit, such as microstrip or coplanar-waveguide transmission line circuits [166] commonly used in semiconductor circuitry. If this technical challenge is met, characterizations of THz semiconductor devices like diodes and transistors or THz planar samples like single carbon nanotube over electrodes [168] could then be well fitted to any THz free-space radiation systems such as the THz-TDS we have, by coupling the radiation into the same waveguide (via an EMXT horn antenna, for example) and eventually onto the planar circuit under test. A potential design of such transition structure within the fabrication capability of the prototyping technique will be proposed in the next chapter.

CHAPTER 5. OTHER EMXT BASED THZ COMPONENTS TOWARD INTEGRATED MICROSYSTEMS

In previous chapters, THz components such as filters (reflectors) and waveguides have been proposed based on EMXT and realized by THz prototyping fabrication. As for coupling energy from THz free-space radiation to waveguides, a THz antenna is required. Also, the waveguide structure needs to be modified for accommodation when THz planar devices need to be integrated into a system or THz samples need to be probed by an EM wave. Designing a transition structure to conduct energy from the EMXT waveguide onto THz planar transmission lines would qualify this potential THz micro-system for planar device/sample integration, testing, and application. This chapter will present our initial efforts to realize the THz antenna and transition structure as well as promising results we obtained so far. Both the antenna and the transition structure are aimed to be manufacturable by the THz 3-D printing technique during the design, so that the future THz micro-system, including these two components, can still be prototyped in an integrated manor. Eventually, a THz transceiver or imager shall be achieved with all the waveguides, antennas, and planar devices (source and detector) integrated together as one prototyped system.

5.1 THz EMXT Horn Antenna

5.1.1 Background and Motivation

As a fundamental component that interfaces free space and circuitry, an antenna plays an important role in many research and technology advancements involving wireless signal propagation. Different antenna structures have been proposed and realized in the THz frequency range. The measurement of a cross-polarized THz dipole antenna was firstly reported in [169]. A dipole antenna located in a pyramidal horn has been reported operating at 800 GHz [170]. Centrally fed Bow-Tie antenna has a broadband nature and a THz Bow-Tie antenna working at 28 THz has been realized [171]. Planar antenna mounted on the back of a dielectric lens is a typical configuration used in astronomical receivers for sending signal to a quasi-optical mixer [164, 173]. The same antenna configuration, if situated on top of a photoconductive substrate, could be employed for THz radiation generation [56]. THz photoconductive antennas with various antenna formations have been proposed and implemented [173, 174]. A corner reflector antenna is naturally fitted for THz application. Because this type of antenna needs a 4λ antenna length as well as about a 1λ distance from the feed to the corner walls, THz wavelength is relatively small and lends itself to a compact size for system integration purposes. Corner reflector antenna arrays have been widely used at THz frequencies, and one example at 2.52 THz is found in [175]. Yagi antennas consisting of an array of different-length dipoles has been realized in the THz regime as well [176]. Last but not least, P. J. Burke [177] first predicted the possibility of having a carbon nanotube transistor with a THz cutoff

frequency. Simulation results of carbon nanotube THz antenna arrays have been reported ever since [178, 179].

People have found various ways to apply EMXT in antenna design, fabrication and optimization. EMXT slabs have been applied as antenna substrates to replace the high-permittivity semiconductor substrates. Because the stop band of the EMXT rejects a majority of the power radiated into the substrate side, the radiation gain and directivity of the antenna at the stop-band frequency are both highly improved [180-183]. Also due to the band gap of the EMXT substrate, inhibitors in the antenna design like surface waves and substrate modes could be reduced or eliminated, therefore improvements on antenna bandwidth, side-lobe suppression, and overall radiation efficiency could be achieved [37, 184-186]. The EMXT has been placed on both sides of a free-standing monopole antenna to enhance the directivity and tune the antenna resonant frequency in [187]. The EMXT structure is also stuck onto the flange plate of a metallic rectangular horn antenna to effectively suppress its surface waves and increase the antenna gain [188]. Two interesting experiments closely related to our THz-TDS instrument are reported: in one experiment the photoconductive antenna of the THz-TDS is embedded into a 3-D EMXT and radiation efficiency peaks near the photonic band edge are observed [189] due to the increase of photon density of states at these frequencies [54]; the second experiment involves replacing common optical fiber with EMXT fiber to deliver the excitation laser pulse onto the photoconductive antenna, which increased the THz-TDS bandwidth from 1 to 2 THz as well as enhanced the THz field amplitude up to a factor

of four [190]. More directly, antennas (array) can be made out of EMXT structures by basically introducing defects with horn shapes in the crystal. This idea has been explored both two-dimensionally with an EMXT wire array structure [191, 192], and three-dimensionally with woodpile structure [193-195] and EMXT fiber array [196, 197].

Now that we demonstrated a low-loss THz waveguide in the last chapter, intuitively if the waveguide defect is flared out to form a horn shape, an EMXT horn antenna would be achieved, just like how a metallic horn antenna is obtained from a metallic waveguide. Because of the larger aperture size at the horn antenna's radiation output end, it has larger gain and directivity [198] than a straight waveguide. With the THz rapid prototyping technique, this type of EMXT horn antenna can be manufactured easily. One potential design concern is that, from the parametric study discussed in Section 4.2.2.3, an increase of the defect core radius up-shifts the center frequency of the pass bands. Since the EMXT horn could have a low-loss transmission only at the overlapping frequencies of the pass bands over the tapered defect radius range, and these defect-mode pass bands are not broadband, this EMXT horn antenna is expected to have a narrowband performance. In the next section, an EMXT horn antenna design is optimized by sweeping the axial length of the horn section and comparing the resulted antenna performance. Simulation results of the optimized antenna design including the return loss, far-field patterns, and radiation efficiency and directivity are then presented, with a comparison to a copper horn antenna of exactly the same dimensions. The comparison will show that this type of

horn antenna based on EMXT hollow-core fiber has comparable performance with the copper horn antenna in the low-frequency pass bands, but much better directivity and far-field pattern in the high-frequency pass bands. We have successfully fabricated two EMXT horn antenna designs so far, and are planning to characterize the antennas using an existing THz-TDS setup. The fabricated sample images and the test plan are presented in the next section as well. To the best of our knowledge, this is the first time a horn antenna based on a hollow-core EMXT fiber is proposed, simulated and fabricated.

5.1.2 Antenna Designs and Simulations

The base EMXT, in which the horn defect is introduced, is exactly the same 2-D triangular lattice air-cylinder array in a polymer background, with 1.3 mm as the air cylinder diameter, 3 mm as the lattice constant, and 5 cladding rings counted from the center of the EMXT cross-section. Figure 5-1 shows the computer rendered image of an EMXT antenna design on the left, as well as a schematic drawing of the defect horn and the straight waveguide section (needed to excite the horn) on the right.

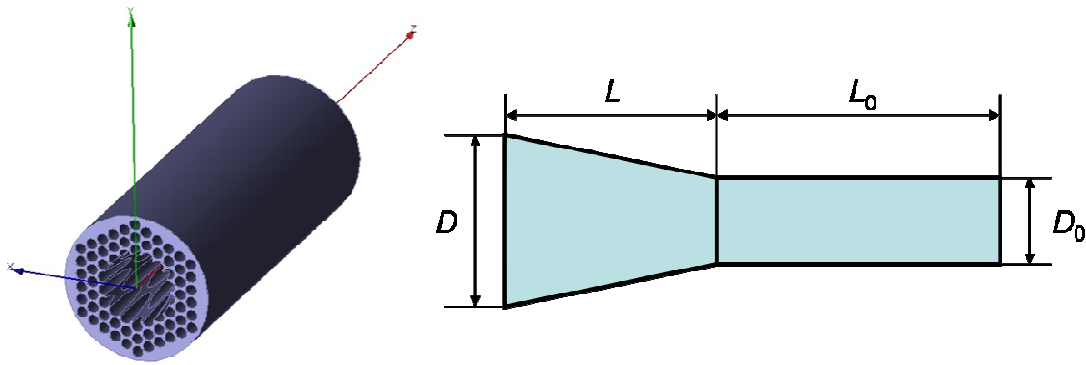
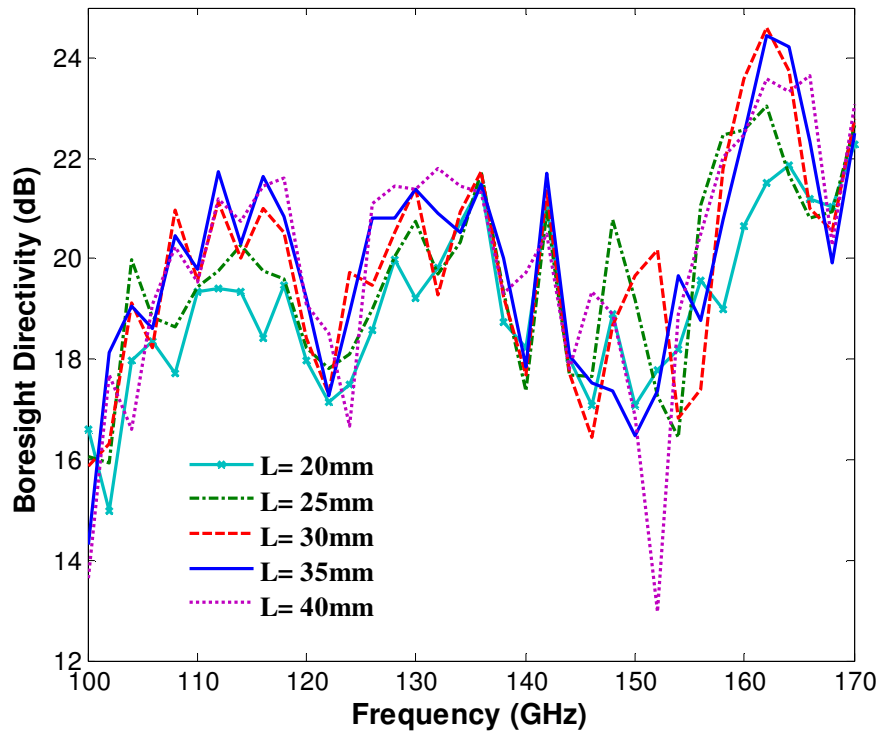


Figure 5-1. Left: Computer rendered image of the EMXT horn antenna. Right: Schematic drawing of the antenna defect shape, with four dimensions defining the horn antenna indicated.

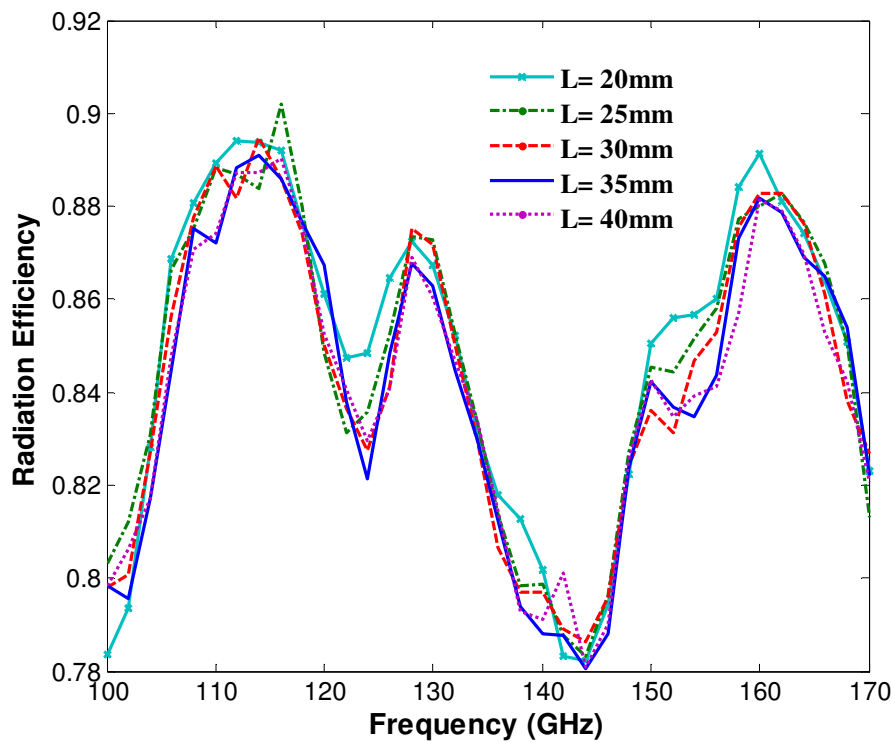
The schematic includes several dimensions that define the horn antenna. They are the aperture diameter D_0 and the axial length L_0 for the straight waveguide section, and the outer aperture diameter D and the axial length L for the horn section. The flare angle Φ of the horn is then calculated:

$$\Phi = 2 \arctan\left(\frac{D - D_0}{2L}\right) \quad (5.1).$$

Since a working THz waveguide with a 4.2-mm defect radius is already realized in the last chapter, this initial trial of the EMXT horn antenna has an inner diameter D_0 of the same size, i.e., 8.4 mm. The original motivation is to expand the aperture size by about twice through the horn. Therefore, the outer diameter D is decided to be 16 mm, which provides an aperture large enough to cover the whole waist (10.8 mm diameter) of the incident Gaussian beam from the THz-TDS transmitter for testing purposes. With these two parameters fixed, the dimensions left for tweaking to optimize the horn antenna performance are the axial lengths of the horn section and the feeding straight-waveguide section.



(a)



(b)

Figure 5-2. (a) EMXT antenna directivity at the boresight direction for various horn axial lengths, resulting a flare angle varying from 10.9° to 21.5° . (b) EMXT antenna radiation efficiency for various horn axial lengths.

Figure 5-2 depicts the simulation results of varying the axial length L . Since the feeding waveguide and horn apertures are fixed, changing L is equivalent to changing the flare angle of the horn. The simulation is done with one PEC circular waveguide feeding the straight waveguide section of the EMXT horn antenna with the TE_{11} mode, and with perfect matching boundaries around the antenna mimicking an infinite open space for the antenna radiation to propagate. During the sweep of L , the axial length of the straight waveguide section is kept at 50 mm. According to the parametric study in 4.2.2.2, this length is sufficiently long for the fundamental low-loss HE_{11} mode to establish itself in the EMXT waveguide with a PEC circular waveguide feed. Also, loss from the build material is not included in this parametric simulation to rule out one variable from any concerns. Study of the material loss impact on the antenna performance will be presented in a later section. In Figure 5-2 (a), three bands with directivity peaks are observed and their center frequencies match with the center frequencies of the waveguide pass bands (Figure 4-2). The boresight direction is the $-Z$ direction in Figure 5-1 (left) along the normal direction of the antenna radiation end, which is the expected direction of highest directivity. The plot reveals that an improvement of antenna directivity is obtained when L is larger than 30 mm. When L is 40 mm long, the directivity is better in the second pass band between 125 and 137 GHz, however much worse in the third pass band around 162 GHz when compared with $L=35$ mm case. The antenna radiation efficiency changes less than 1% with L in all three pass bands (contrary to the case of a copper horn antenna [198]), as seen from Figure 5-2 (b). Based on the parametric study results, $L=$

35 mm is selected as the final dimension for the horn axial length. With this dimension the flare angle of the horn is 12.4 degrees.

As shown in Section 4.2.2.2, a straight waveguide length of 25 mm barely makes the higher-order modes vanish and the propagation within the waveguide is quite lossy. An antenna simulation with $L_0 = 25$ mm has been conducted, and indeed the EMXT band features are absent and poor radiation efficiency is obtained. Keeping in mind that longer L_0 results in slightly better loss per unit length (from Figure 4-5), it is noted that if the waveguide is too long, the total propagation loss would still be larger and would harm the overall antenna radiation efficiency more. Therefore, L_0 is chosen to be 50 mm in this initial trial.

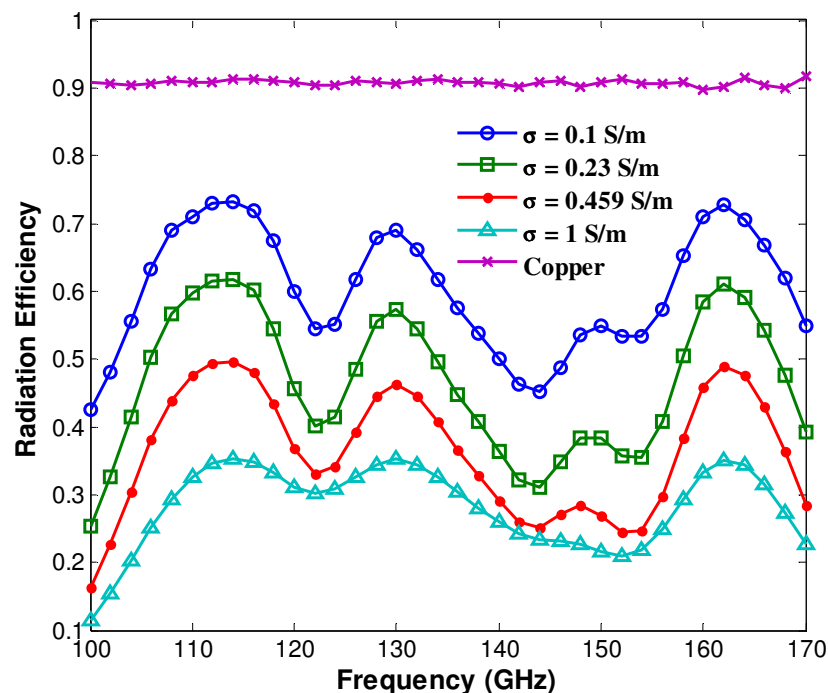


Figure 5-3. Radiation efficiencies of EMXT horn antennas with various build material losses, and a circular horn antenna of exactly the same dimensions made by copper.

With all the dimensions finalized, the build material loss is included in the simulation to study the overall antenna radiation efficiency. The constant conductivity model is applied here to represent the material loss. Figure 5-3 plots the radiation efficiencies of the EMXT antenna with various conductivity losses σ , in comparison with a horn antenna of exactly the same dimensions made by copper ($\sigma = 5.8e7$ Siemens/m). The figure shows a monotonic decrease of the antenna efficiency as the material loss increases. Meanwhile, the copper horn antenna is highly efficient, with a radiation efficiency over 90% over most of the frequency range. However, the antenna efficiency without the material loss reaches over 88% in the pass bands centered around 114 and 162 GHz, as seen in Figure 5-2(b). This means the EMXT cladding performs almost as well as the solid metal cladding in prohibiting radiation loss over the wave path. It is the build material loss that inevitably degrades the EMXT antenna efficiency. In principle the proposed type of EMXT horn antenna could radiate as efficiently as a copper horn antenna if it is fabricated with materials of very low loss over this frequency range. Also as seen in Figure 5-3, the bandwidth of the EMXT antenna is determined by the pass-band bandwidth of the straight EMXT waveguide section. Therefore, the EMXT antenna has a much narrower bandwidth than the copper horn antenna.

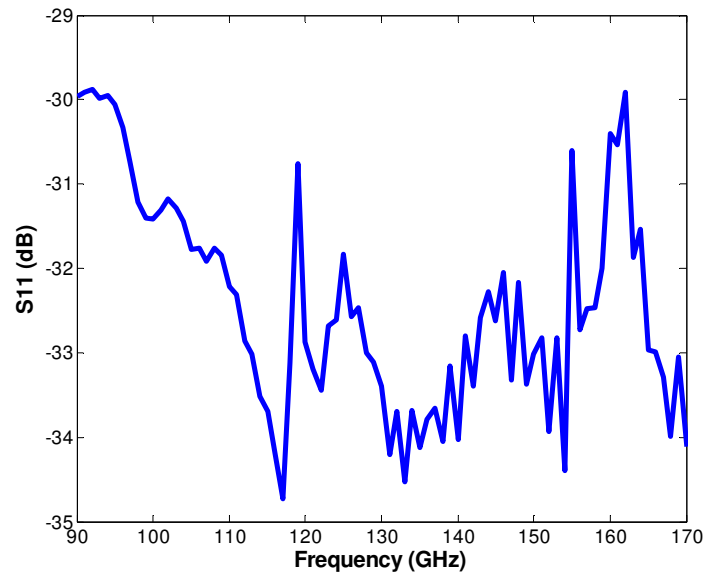
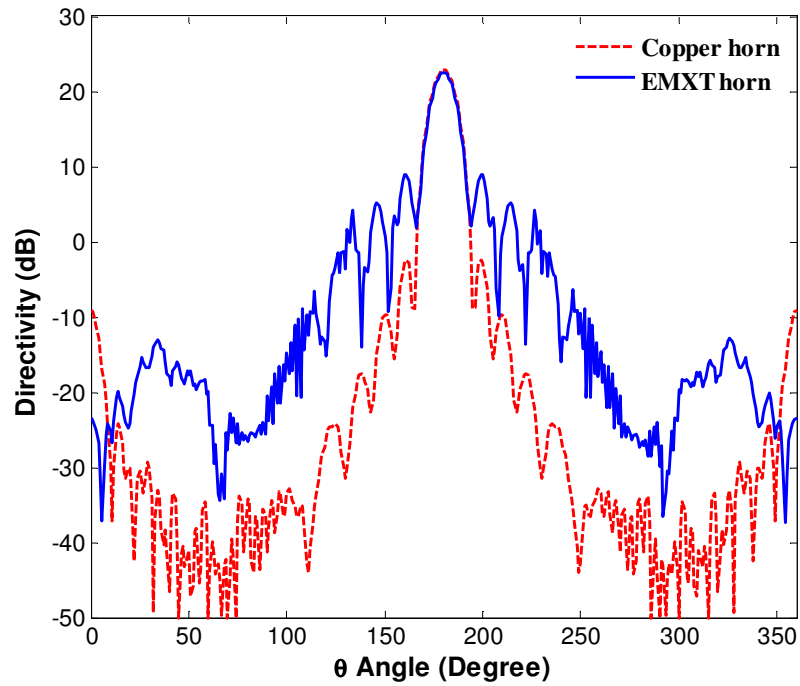
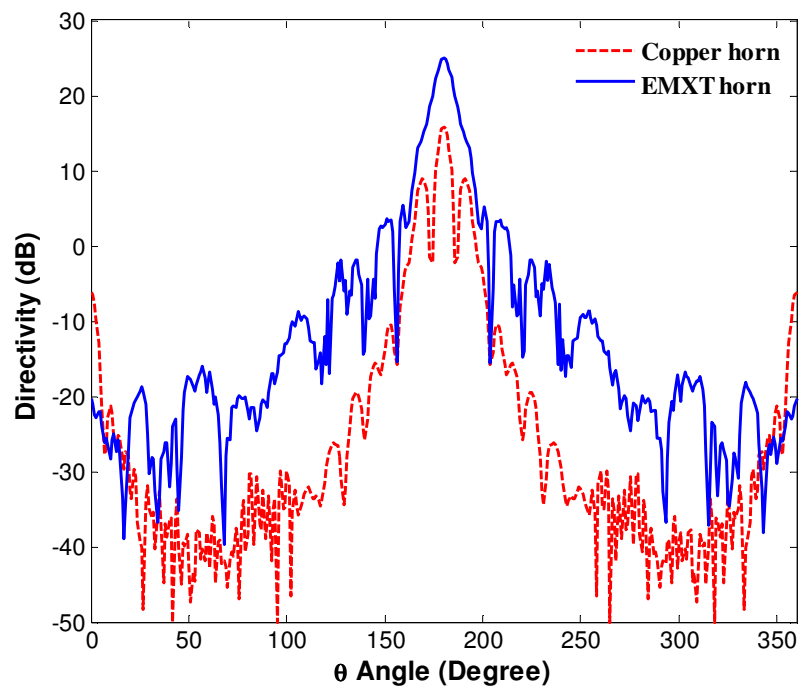


Figure 5-4. Return loss of the optimized EMXT horn antenna, with the material loss represented by $\sigma = 0.459$ Siemens/m.

Since the EMXT antenna will be fabricated with the THz rapid prototyping technique, the constant conductivity of 0.459 Siemens/m corresponding to VeroBlue polymer material loss is employed in the simulations from this point on. Plotted in Figure 5-4, the return loss of the antenna with optimized dimensions is less than -29.8 dB over the simulated frequency range, showing a very good impedance matching between the antenna and the feed.



(a)



(b)

Figure 5-5. Radiation patterns of the EMXT and copper horn antenna at $\phi = 0^\circ$ cut plane with θ sweeping from 0 to 360 degree, at (a) 114 GHz and (b) 162 GHz.

Figure 5-5 depicts the far-field radiation pattern of the EMXT and copper horn antennas captured at $\phi = 0^\circ$ cut plane (X-Z plane in Figure 5-1, left), with θ sweeping

from 0 to 360 degree. Two center frequencies of the pass bands for the EMXT horn antenna are chosen to generate the plots. It is clear that directional beams are obtained from the EMXT antenna at the two working frequencies. At 114 GHz, the EMXT antenna has almost the same boresight ($\theta = 180^\circ$) directivity and main-beam angle with the copper horn antenna of the same dimensions. The copper horn antenna has about 10 dB better side lobe suppression though. However, the EMXT antenna works much better than the copper horn antenna at 162 GHz with 9.4 dB higher directivity at the boresight direction, and the integrity of the main-beam is maintained instead of splitting into three small beams in the copper horn case. The reason the copper horn antenna performs much worse at higher frequency is that it suffers from severe over-mode problem, whereas along the EMXT horn antenna those higher-order modes are evanescent due to their much larger propagation attenuation both from radiation loss and material loss. Therefore, this type of EMXT horn antenna could potentially be a good substitute for metallic horn antenna at over-moded frequencies to achieve highly directional beam.

For reasons that will be elaborated in Section 5.2, a modified EMXT antenna design with the same D , L and L_0 but smaller D_0 (4.2 mm) is also simulated. The results yield similar pass band frequencies and beam width, however about 3.5 dB lower directivity at the center frequency of the first pass band and lower radiation efficiency over the simulated frequency range than the original design. The main reason for this performance deterioration is the greater transmission loss resulted from the smaller D_0 in the straight waveguide section. Nevertheless, the modified design

still provides a usable THz EMXT antenna. Smaller D_0 on the other hand prohibits higher-order modes, so that the requirement on the waveguide length to achieve low-loss transmission is relieved. A later simulation reveals that a 35-mm long EMXT waveguide with aperture diameter of 4.2 mm is long enough to exhibit pass bands with low propagation losses. Therefore, this modified waveguide design would lead to more compact EMXT antennas and an integrated THz system.

5.1.3 EMXT Antenna Fabrication and Measurement Plan

This type of EMXT horn antenna has not been realized in the literature probably because of the practical fabrication difficulty. Due to its tapered defect shape, the commonly used hot-drawn method to fabricate fibers [167] is not applicable since the method is limited to the fabrication of structures with uniform cross section. The hand-assembly method can not be used as well [89] because it would be very difficult to deal with the interception between the cladding tubes and the center horn-shape tube. With the THz prototyping technique developed by our group, fabrication of this structure becomes fairly straight forward. The tapered horn shape is simply input into the machine and printed layer-by-layer along the axial direction.

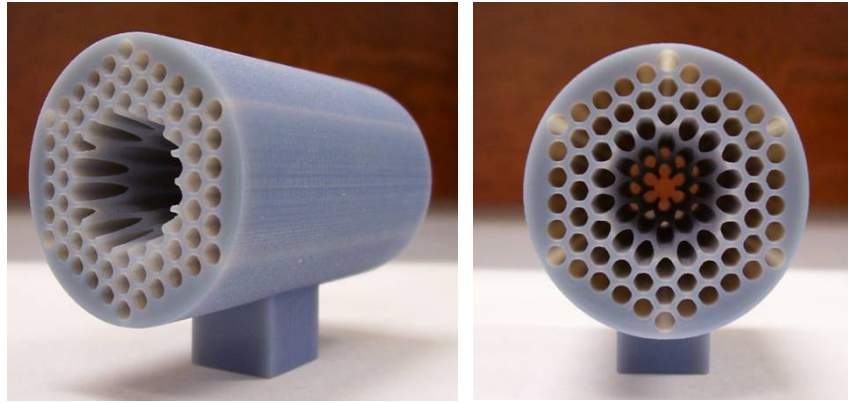


Figure 5-6. Photos of the fabricated THz EMXT horn antenna, with $D = 16$ mm, $D_0 = 4.2$ mm, $L = 35$ mm, and $L_0 = 35$ mm.

Figure 5-6 shows two images of the fabricated EMXT horn antenna sample, with $D = 16$ mm, $D_0 = 4.2$ mm, $L = 35$ mm, and $L_0 = 35$ mm. From the side view the flare-out of the horn shape is clearly observed, and the front view shows the horn tapered down to a 4.2 mm straight waveguide defect diameter. Because of the downshifting of the feature frequencies measured in Chapter 4, we are suspecting that the glossy mode printing causes the fabricated dimension errors. Therefore, in this antenna fabrication matt mode printing is applied with the support material occupying all the air regions in the design. The support material is removed by water flushing after the antenna sample is printed. Another design with $D = 16$ mm, $D_0 = 8.4$ mm, $L = 35$ mm, and $L_0 = 50$ mm is also manufactured.

The experimental plan to characterize the radiation pattern of the fabricated EMXT horn antennas using the same THz-TDS has been made. Figure 5-7 demonstrates the planned measurement setup. The THz beam transmitter will be bolted down to an automated rotating stage together with the EMXT horn antenna, so that their relative positions are fixed. The beam radiated by the transmitter will feed

the antenna through the straight waveguide section (with focusing optics, if necessary), and the THz wave is radiated out on the horn's output end. The receiver of the THz-TDS is placed at a far-field distance away from the EMXT horn antenna, and measures the received power at different θ angles while the rotation stage sweeps it in the $\varphi = 0^\circ$ cut plane, so that the antenna radiation pattern is mapped out. The quantity measured at each θ angle is the transmitted waveform, and the whole power spectrum is obtained by Fourier transforming the waveform to the frequency domain. To avoid multiple reflections from the peripheral of the measurement environment, THz radiation absorption materials (RAM) will be positioned around the test stage to absorb any reflections [135]. The test bench is currently under construction.

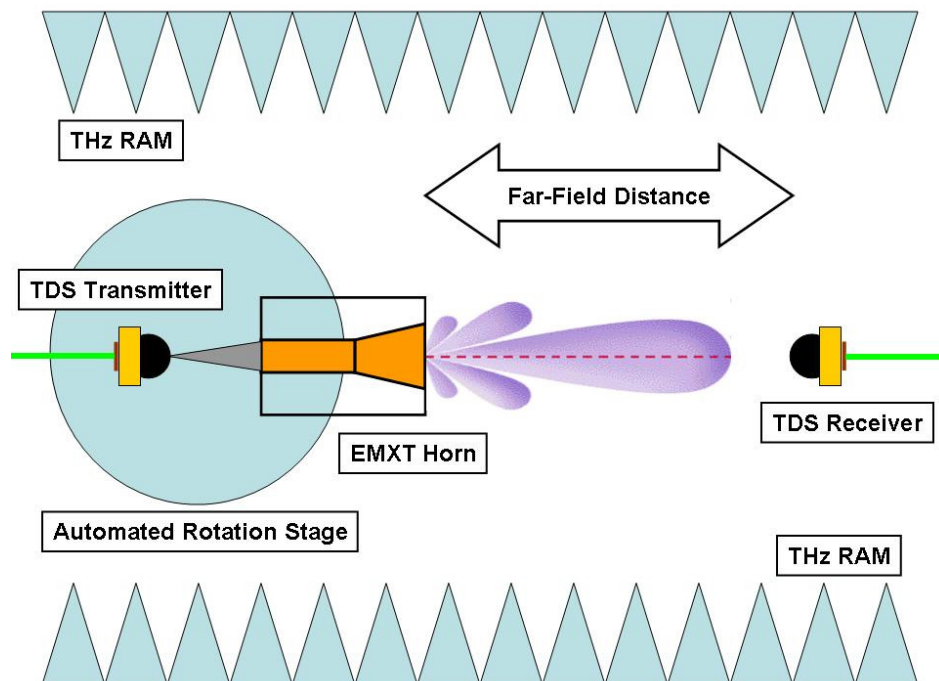


Figure 5-7. Schematic of the planned bench setup to measure the far-field radiation patterns of the EMXT horn antennas.

5.2 THz Waveguide to Microstrip Line Transition

5.2.1 Motivation and Existing Transition Architectures

Solid-state devices have been able to operate at the speed of THz frequencies. A variety of THz solid-state devices have been proposed and realized. To name a few: planar Schottky diode mixers [199, 200], superconductor-insulator-superconductor (SIS) tunnel junction mixers [201-204], hot electron bolometer (HEB) mixers [205-207], and photoconductive antennas on low-temperature-grown GaAs substrate (LTG-GaAs) [56, 174] for THz detectors, and InP MMIC millimeter-wave power amplifiers [59, 208], waveguide-mounted GaAs Schottky barrier diodes [209-211], and again the photoconductive on-chip antennas [174, 212, 213] for THz generation. To be able to characterize or employ these planar devices with free-space THz fields like the THz-TDS, we require a coupling of the power from free space onto the planar circuit incorporating these devices. More importantly, THz sources and detectors made of these planar devices would be able to be integrated into the system if this coupling is realized, which makes the system a self-sufficient THz transceiver. Also, for the necessities of THz material science and biological and biomedical imaging researches, lots of samples such as individual carbon nanotube (CNT) or CNT ensembles, bio-tissues and bio-solutions, and materials in bulky or powder forms need to be characterized at THz frequencies. “Lab-on-Chip” transmission line circuits provide a convenient and reliable method to characterize those samples [168, 214-216]. Again the measurement could only be done under the scope of free-space THz systems if the power propagating in air could be coupled efficiently onto the

planar circuit for sample characterizations. In the previous section the EMXT horn antenna has been proposed and provides a solution to the coupling of a THz wave from free space to a THz waveguide and vice versa already has a solution. The unsolved part now is the transition from the EMXT waveguide to a THz planar transmission line. Since the systematic fabrication of a potential integrated THz system is pursued as mentioned in Section 3.4, it would be ideal if this waveguide-to-planar circuit transition structure can be fabricated by the same THz prototyping technique, just like all the other components.

Several topologies to convert energy from a waveguide mode to a planar transmission line mode, such as the commonly used microstrip line and CPW line, have been reported in literature. Since our ultimate goal is to construct a compact THz micro-system, any transition employing a substrate integrated far-field antenna as a connecting bridge between the waveguide and planar circuit is ruled out from our consideration because that would inevitably increase the size of the whole system. Examples of such a transition using the near-field coupling between a waveguide and planar circuit include: metallic circular waveguide-to-microstrip transition by intruding the trace of the microstrip into the back-shortened waveguide along the radial direction at $\lambda/4$ distance away from the back-short plate [217-222]. This is the most commonly used transition from a circular waveguide to a microstrip and becomes our first trial. The schematic of this topology is shown in Figure 5-8. Also, a circular waveguide-to-coaxial line transition could be realized either by inserting the center conductor of the coaxial line into the waveguide along the axial direction (good

coupling to radially polarized TM modes) with the waveguide shell connected to the coaxial line outer conductor [223-226], or by inserting the center conductor of the coaxial line along the axial direction (good coupling to linearly polarized TE modes) with a back-short plate located a quarter-wavelength away [227-229]. E-plane or H-plane probes inserted into the cross-sectional plane of the rectangular waveguide with back-short plate [230-233]; Coplanar-waveguide line with center trace extended into the rectangular waveguide along the axial direction as well as finline or ridged designs at the junction end of the ground traces to achieve broadband transition [234-236]; And rectangular waveguide backed by microstrip patch antenna or slot antenna for wave coupling [237, 238]. Another type of transition, which motivated our working design presented in the next section, is a tapered dielectric waveguide intruded into either a metallic [239-241] or a two-dimensional EMXT [242-245] waveguide to transmit the energy into the dielectrics. The dielectric waveguide is then tapered down on the other end where it is eventually connected to the microstrip line substrate [239, 240, 246-248]. The working principle of all the above transitions is to modify the field profile of the designated waveguide mode, including both the polarization direction and the field spread, and changing the boundary conditions around the transition section, so that the modified E-field has a very similar field distribution with the transmission mode of the planar transmission line. This mode profile matching theory applies as well when we design the transition structure from our hollow-core EMXT waveguide to planar circuits.

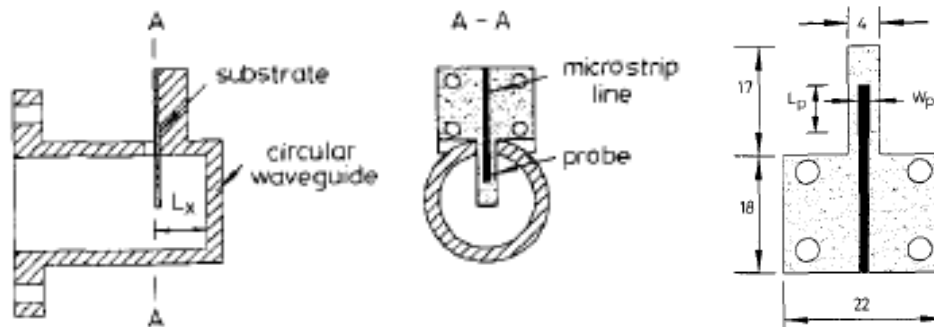


Figure 5-8. Schematics of the most commonly used circular waveguide-to-microstrip line transition. L_x is around quarter-wavelength long of the design frequency. The ground plane of the microstrip line on the back of the substrate connects with the ground of the circular waveguide [221].

The transition topology shown in Figure 5-8 is the initial design we chose to try, because it is the most commonly used topology and our EMXT waveguide also has a circular aperture shape. However, a later simulation revealed that this transition relies on a critical detail which the EMXT waveguide can not satisfy: The ground plane of the microstrip line on the back of the substrate has to be connected to the ground of the circular waveguide (metallic shell), so that they share the same electric potential and the linearly-polarized E-field lines of the fundamental TE_{11} mode in the circular waveguide will be dragged towards the back of the substrate at the transition area, and eventually change the orientation from along the probe to across the substrate connecting the probe and the ground plane of the microstrip line, which is exactly the field distribution of the microstrip-line transmission mode [166]. In fact, our simulations show that if the ground of a circular waveguide is disconnected from the microstrip-line ground plane, this transition would not work at all even if all the other parts of the design remained the same. Since an EMXT waveguide does not have a well defined ground plane anywhere, this design in principle can not be

implemented to accomplish the transition we pursue. Indeed, simulations of THz version of this design with the PEC waveguide replaced by the EMXT waveguide yield an almost zero power transition from the waveguide to the microstrip line no matter how the other design parameters are adjusted. The insight we gained from this unsuccessful initial trial is that any transition design involving reorientation of the E-field direction in the waveguide would not work for our case, due to the lack of a metallic ground plane on the EMXT waveguide. Our trials are then focused on transition designs that only compress the field distribution to that of the planar-circuit mode, but without altering the field line direction [239, 246-248].

5.2.2 Transition Structure Design and Simulations

A microstrip line is a very commonly used planar transmission line [166]. It can be fabricated via PCB photolithography processes and is easily integrated with other passive and active semiconductor devices [166]. Shown in Figure 5-9 (a) is the typical microstrip geometry, including a center conductor trace-line with width w , and a substrate with thickness d and dielectric constant ϵ_r . As plotted in Figure 5-9 (b), the E-field line of its fundamental transmission mode in the substrate is projected from the trace conductor towards the ground plane, with quasi-linear polarization perpendicular to the ground plane. This E-field profile makes the fundamental mode potentially excitable by any incident E-field with the same linear polarization direction and comparable field distribution size. Because of these advantages, the

microstrip line is chosen as our planar transmission-line circuit for the transition design.

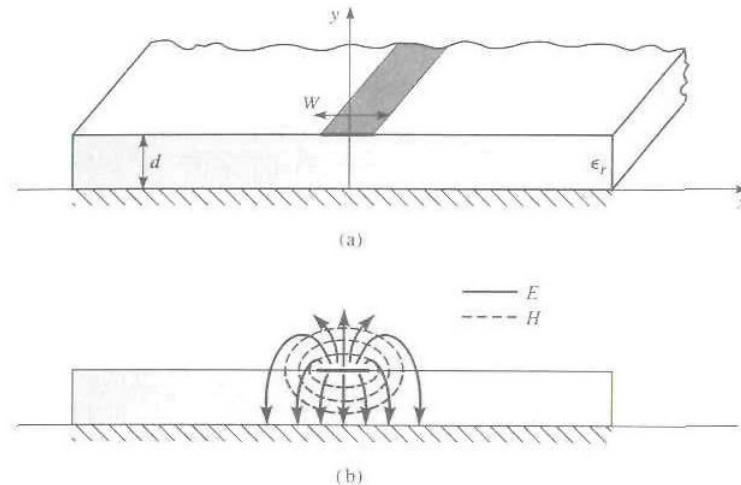


Figure 5-9. (a) Geometry and (b) E and H-field lines of the microstrip transmission line [166].

The thicker the substrate, the more surface-wave modes that are lossy and undesired may exist in the substrate [166]. This is why a microstrip line is rarely used at several hundreds of GHz; a substrate of several tens of micron thickness is needed to guarantee low-loss single mode operation of the microstrip line at these high frequencies [249, 250]. The microstrip line geometry we determined for this initial design has a trace width w of 0.4 mm, substrate thickness d of 0.127 mm and dielectric constant ϵ_r of 2.2, and ground plane width w_0 of 4 mm. This substrate is commercially available as the RT/Duroid 5880 PCB board from Rogers Corporation [251]. The trace width is fabricable with the photolithography processes in our lab. With this geometry, the microstrip line is single-moded up to 123 GHz, according to

the HFSS eigen-mode simulations [124]. Therefore, at least within the first pass band of our EMXT waveguide between 104 and 120 GHz, this microstrip line should provide reasonable propagation with the same mode profile as in Figure 5-9 (b).

Figure 5-10 demonstrates the new EMXT waveguide-to-microstrip line transition structure we propose, in a back-to-back configuration for the convenience of our simulations. It consists of two EMXT waveguides fed by PEC circular waveguides (TE_{11} modes) on both ends, which then feed the transition structure and the planar circuit in the middle with the fundamental HE_{11} mode. The defect core radius of the EMXT waveguide is 2.1 mm and each waveguide is 35 mm long. On each end, the transition structure is made of four sections. The first section is a tapered dielectric cone with circular cross-section, 5 mm height and 2.1 mm base radius as shown in the top middle inset of Figure 5-10. The cone is completely intruded into the EMXT waveguide by the distance of its height. This section, since it connects the air region with the dielectric region by a tapered impedance, helps reduce the reflected power and couples the EMXT waveguide mode to the dielectric waveguide HE_{11} mode [252, 253]. The second section is simply a 5-mm long circular dielectric rod with the same 2.1 mm radius as shown in the middle inset image. This section serves as a region to allow the dielectric waveguide mode to build up and stabilize. It is indispensable. Simulations show that without this section, the transition performance becomes largely degraded. Also shown in the same inset, immediately following the second section is a 5-mm long dielectric section transforming the cross-section shape from a 2.1 mm radius circle to 4.2 mm x 4.2 mm square.

Computer-Aided-Drawing is used to generate the smooth surface curvatures needed to complete this cross-section shape transition. The smoothness of the surfaces ensures that the total-internal-reflection (TIR) mechanism within the dielectric waveguide is maintained [252] and the propagating HE_{11} mode holds throughout the transition. All the above three sections are made of polymer printing material with a relative dielectric constant of 2.75, so that the structure can be accommodated by the THz prototyping fabrication directly. The final transition section is a rectangular wedge with its cross-section tapered, over an axial distance of 5 mm, from a 4.2 mm x 4.2 mm square to a 0.4 mm x 0.127 mm rectangle. This structure exactly fits both the trace width and substrate thickness of the microstrip line. As demonstrated in the right inset, two PEC ground flares (orange color) are placed on the top and bottom surfaces of the dielectric wedge. They connect to the center trace and the ground plane of the microstrip line, respectively. These PEC flares form a wedged parallel plate waveguide [166] and help compress the E-field distribution across them eventually to the tiny size at the joint to the microstrip line. Keeping in mind that the transverse E-field of the incident HE_{11} mode is quasi-linearly polarized across the PEC flares, it could be well coupled to the microstrip-line mode as shown in Figure 5-9 (b). The dielectric wedge is made of Duroid 5880 since it needs to be integrated with the microstrip line substrate. Moreover, it would only result in a tiny 0.3% power reflection loss at the polymer/Duroid interface.

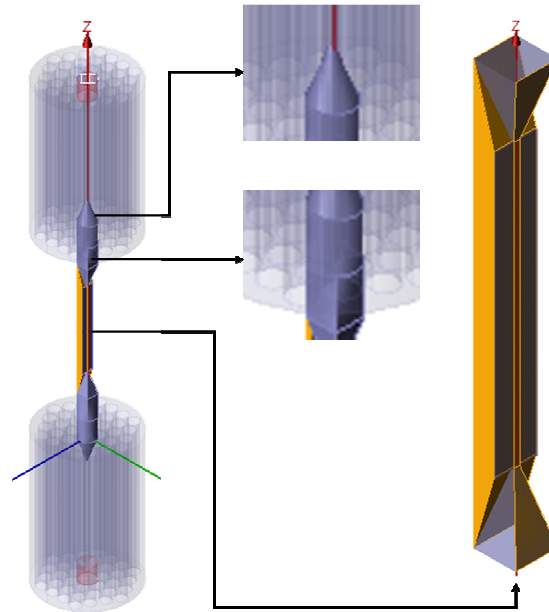


Figure 5-10. Schematic of the EMXT waveguide-to-microstrip line transition design. Three zoomed-in insets demonstrate different sections of the transition structure.

The reason why the EMXT waveguide aperture radius is shrunk from 4.2 mm to 2.1 mm in the design is that the polymer rod waveguide with the 4.2 mm radius works best between 70 and 95 GHz and shows a transmission roll-off at higher frequencies. With the smaller radius of 2.1 mm, the polymer rod waveguide exhibits prime transmission between 100 and 120 GHz, which coincides with the first pass band of the EMXT waveguide whose defect radius is 2.1 mm. Figure 5-11 shows the waveport simulation results of a 60-mm long EMXT waveguide (no material loss) with a 2.1 mm defect radius. From the S_{21} magnitude plot, two pass bands at 97-114 GHz and 145-158 GHz are clearly observed. The $|S_{11}|$ values are below -18 dB over the simulated frequency range. With the S-parameters the calculated power loss factor at 108 GHz is 0.036 dB/mm. This confirms that the EMXT waveguide feeds on both

ends are working and their first pass band aligns with the transmission band of the polymer rod waveguide in frequency.

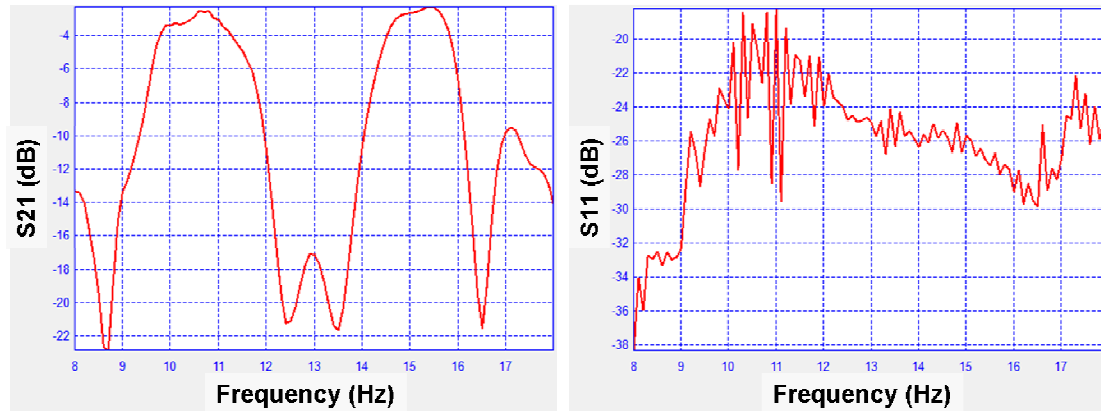


Figure 5-11. Simulated S-parameters of a 60-mm long EMXT waveguide with a 2.1 mm defect radius.

Simulation of the whole transition structure in Figure 5-10 is performed with the GEMS distributed FDTD package [165]. The software divides this tremendously electrically large model into several regions and designates each node computer in the cluster network to calculate the field equations over only one specific region. The head computer in the cluster manages the communication of messages and temporary computation results among the node computers and yields the final simulation results. The microstrip line has a length of 20 mm in the simulation. Material loss is a rather severe problem in this design, because a majority of the wave is traveling within the dielectric medium over an axial distance of 40 mm, counting both ends. The constant conductivity model is applied in the simulation to estimate the various material losses in the structure. For the polymer build material, $\sigma = 0.459$ Siemens/m is used just as

in Chapter 4. For the Duroid 5880, a conductivity of 0.18 Siemens/m, corresponding to a 0.006 loss tangent at 100 GHz [133], is applied. Copper is used as the metal for the PEC flares, microstrip line trace and ground plane, with a conductivity of 5.8×10^7 Siemens/m. Figure 5-12 plots the simulated $|S_{21}|$ values of the whole transition, which exhibits two pass bands corresponding to that of the EMXT waveguide feeds. Without any material loss, the structure has a -6.75 dB and -8.11 dB insertion loss at 108 GHz and 147 GHz, respectively. Considering the 0.036 dB/mm radiation loss factor from the EMXT waveguides, the coupling loss due to radiation leakages along the transition section is $(-6.75 \text{ dB} - (-0.036 \text{ dB/mm} \times 35 \text{ mm} \times 2)) / 2 = -2.115 \text{ dB}$ on each side. When material loss is added in (except the microstrip line section), the insertion loss is increased by about 5.2 dB in the two pass bands. This extra loss includes both the build material loss along the EMXT waveguide and the material absorption losses through the aforementioned four transition sections. Finally, as the conduction and dielectric losses of the microstrip line are added, the total insertion loss increases further by 3 dB at 108 GHz and 5 dB at 147 GHz. The microstrip line section brings in more loss at 147 GHz, because of both the larger dielectric loss tangent at higher frequencies from the constant conductivity model used, and the involvement of higher-order microstrip line modes with larger loss beyond 123 GHz. One simulation is also done with the microstrip line cut open in the middle, and the obtained $|S_{21}|$ values are below -30 dB all over the frequency range. Therefore the energy is indeed conducted through the microstrip line as designed. Despite the overall insertion loss of -15 dB at 108 GHz, as shown by the red-square curve in Figure 5-12, this

transmission is still quite measurable with the ~ 70 dB dynamic range available from our THz-TDS and leaves ~ 55 dB usable signal power for the device/sample under test.

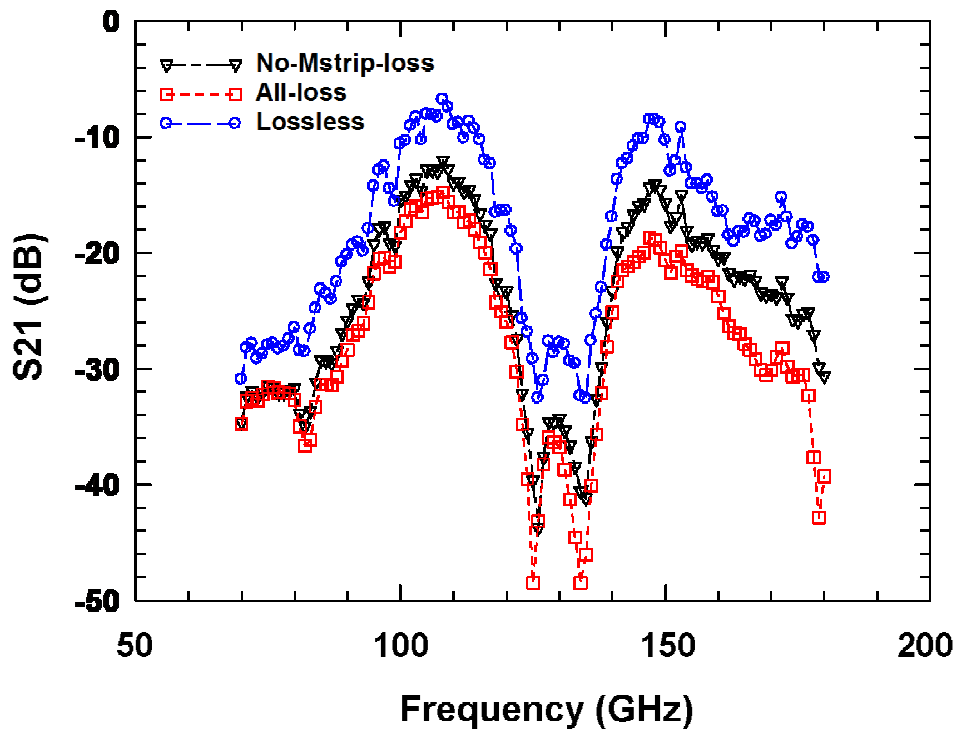


Figure 5-12. Simulated $|S_{21}|$ of the whole EMXT waveguide-to-microstrip line transition structure, including no-material-loss case, all-material-losses except the microstrip line section case, and all-material-losses case.

Figure 5-13 also shows the return loss of the transition structure with all the material losses included. The $|S_{11}|$ is below -10 dB over the entire simulated frequency range, and below -22 dB and -17 dB at 108 GHz and 147 GHz, respectively, showing a good impedance matching along the transition structure. Combining the insertion loss and the return loss, we consider this proposed design an operational EMXT waveguide-to-microstrip line transition. Except for the fourth transition section and

the THz microstrip line part, the whole transition system is designed ready for fabrication using the THz prototyping method. Therefore, this system is low-cost and easy to manufacture.

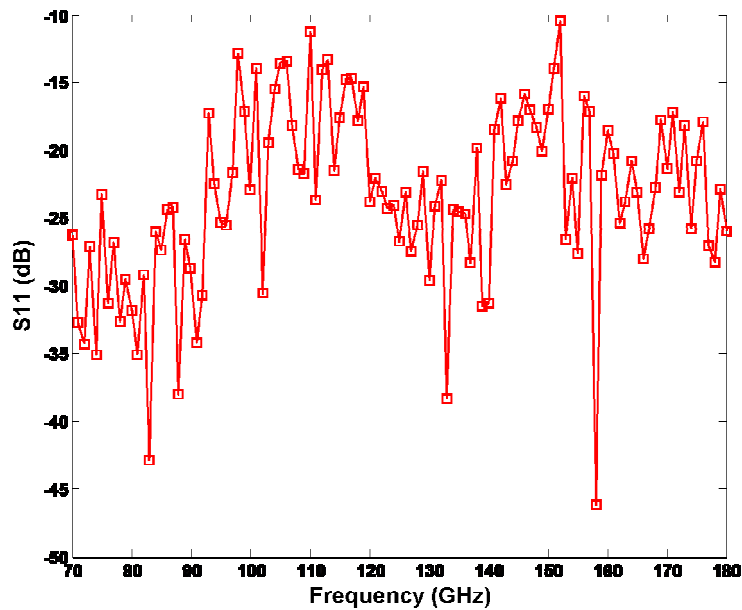


Figure 5-13. Simulated $|S_{11}|$ of the whole EMXT waveguide-to-microstrip line transition structure, including all the material losses.

5.3 Conclusion and Future Work

In the first half of this chapter, a THz EMXT horn antenna based on a flared version of the THz waveguide demonstrated in the last chapter is proposed. The antenna is formed by modifying the defect of the EMXT waveguide to a horn shape. With the outer and inner diameter of the horn pre-determined, optimization of this EMXT horn antenna is done by varying the axial length of the horn to get the overall best antenna directivity and radiation efficiency. With the optimized design

parameters, the antenna is simulated and exhibits very low return loss, almost the same boresight directivity and main-beam width with a copper horn antenna of the same dimensions at the first pass band, and much better boresight directivity and radiation pattern than copper horn at the higher frequency pass band. This EMXT antenna can radiate as efficiently as the copper horn antenna in principle, according to the radiation efficiency simulation of the EMXT antenna without material loss. However, in practice, the build material loss along the rather long straight-waveguide feed for the EMXT horn significantly deteriorates the antenna efficiency. A build material with lower loss is needed to improve its efficiency. EMXT horn antennas of two designs have been fabricated using the THz rapid prototyping technique developed in our group. We believe that this is the first time this type of horn antenna based on a hollow-core EMXT fiber is fabricated. Images of the fabricated sample show good quality. Plans have been made to measure the far-field radiation pattern of the EMXT antenna with the THz-TDS photoconductive antenna system and a test stage setup which is currently undergoing construction.

In the second half of this chapter, demands to integrate THz semiconductor devices or measure sample properties at THz on planar transmission-line circuits are appreciated. Efforts are made to design an EMXT waveguide-to-microstrip line transition structure so that planar circuit source/detector and applications could be included in the final THz micro-system. Our preliminary study rules out any transition design that needs to twist the E-field orientation of the waveguide mode. In a later design we proposed a structure which transmitted energy from the hollow waveguide

aperture into a solid dielectric rod waveguide, and then propagated it to the microstrip line by tapering the dielectric rod cross-section to the sizes of the microstrip-line substrate thickness and trace width. Two PEC terminations are positioned on the top and bottom of the tapered dielectric waveguide surfaces, so that better cladding and compression of the E-field size is achieved. A back-to-back setup, including two EMXT waveguide feeds and two identical transition structures on both ends, and one THz microstrip line section in the middle, has been simulated. Results show a small impedance mismatch and an acceptable insertion loss of the whole back-to-back system. The coupling and radiation loss from each transition structure is estimated to be -2.115 dB. The insertion loss obtained is around -15 dB at the prime working frequency, mainly due to the dielectric material loss when the THz wave is traveling inside the solid dielectric rod waveguide. This insertion loss is quite tolerable with the superior 70-dB signal-to-noise ratio available from the THz-TDS system. Therefore, this design can be tested using our THz-TDS. Fabrication of the transition system is being planned in our lab. Although the fabrication of the EMXT waveguide feeds integrated with the first three transition sections is accommodated readily by our THz prototyping technique, there are still quite some tricky points for the fabrication of the other parts. First, how to make the duroid (or Teflon, same dielectric constant [133]) dielectric wedge as the final transition section; second, how to precisely integrate the dielectric wedge tip onto the microstrip-line substrate and align it with the center trace; and third, the two PEC flares are doable with copper tape [239]. However, the connection of the 400-micron wide tip to the microstrip-line trace needs fine soldering

or some other manufacture processes. If the THz microstrip line circuit can be fabricated with the THz prototyping method – in principle it could since the vertical printing resolution is 16 micron and the polymer material loss is moderate over this frequency range, and cladding the polymer substrate with copper could be done via metallization – then the fabrication of the whole system could potentially all be done by the THz rapid prototyping method. All these fabrication issues are currently under exploration, and the transition design has quite some margin for optimization as well, such as the specific PEC flare designs to enhance transmission [239].

CHAPTER 6. CONCLUSIONS AND FUTURE WORKS

THz spectrum range has become a scientific and engineering research frontier in recent years due to the richness of physical, chemical and biological processes within this frequency range, the higher spatial resolution and bandwidth available for THz imaging and THz communication when compared to microwave systems, as well as the lower scattering loss and non-ionizing energy level at THz frequency when compared to optics. The last decade has been a fast expanding period for THz with many emerging scientific findings, technology innovations and potential applications. However, the growth stride is still hindered by limited availability of sources/detectors, various components including filters, waveguides and antennas, and integrated systems in this frequency region. The primary goal of this dissertation is to develop some of these critical THz resources, including their designs, fabrications and characterizations.

First, thermal radiation from three-dimensional THz electromagnetic crystals is investigated. An EMXT can drastically modify its own spontaneous emission spectra via the redistribution of the photon density of states (DOS) around the band gap frequencies. Within a band gap of an EMXT, there is no photon state capable of coupling with an atomic transition, yielding a zero DOS. Adjacent to band gap edge frequencies, “anti-crossing” effects cause a flat dispersion relationship and result in a large DOS. Assuming ideal coupling to the external environment, thermal radiation emitted by an object has a linear relationship with its photon DOS. Consequently, a

thermal radiation enhancement can be expected around the EMXT band edge frequencies. Therefore, a THz thermal radiation source with a tunable operation frequency could be potentially built by utilizing this nontrivial emission from a 3-D EMXT. The investigation starts with a three-dimensional silicon woodpile EMXT with a band gap centered at 200 GHz. The DOS of this infinite EMXT is calculated using a K-space extrapolation algorithm, followed by the thermal emission calculation with the DOS obtained from Planck's equation. Several enhancement peaks over the normal blackbody emission near the band gap are observed. The prediction is then verified via thermal emission measurement. The silicon woodpile is fabricated by semiconductor saw-blade dicing process, and its thermal radiation at constant temperature is measured by a Fourier Transform Spectrometer (FTS). Thermal radiation from a control blackbody with the same form factor is also measured as a reference. After a two-temperature calibration scheme, the emissivity of the woodpile EMXT is extracted, and the measured radiation-peak frequencies match well with the prediction. However, only at several frequencies where exceptional enhancements occur in the calculation, the measured EMXT emission exceeds the control blackbody, indicating the ideal coupling assumption may not be valid for all photon states. Meanwhile, the investigation is extended to a metallic woodpile structure and a 2-D EMXT structure. The designed metallic WPS has all the same dimensions as the silicon WPS except that it is made of tungsten, so that it can be electrically heated to a very high temperature for larger emission power. Calculations also show thermal radiation enhancements over normal blackbody from the tungsten woodpile EMXT,

but the enhancement factor is not as large as the silicon WPS. The 2-D EMXT is a metallic cubic cavity array with one side of the termination only a skin-depth thick, so that power could radiate out. Strong resonances within the metallic cavity and the array formation promises a greatly enhanced emission peak around a single THz frequency from this structure, which may lead to a low-cost electrically heated THz thermal source.

Second, a novel THz rapid prototyping technique for 3-D THz EMXT structure fabrication is developed. Due to its band gap nature, components such as band pass/stop filters, Bragg reflectors, waveguides, and antennas can be made from an EMXT. However, the THz wavelength makes the characteristic dimensions of such EMXT components lie in between the conventional micromachining at microwave and the micro/nano-fabrication at optical frequencies and practically difficult to manufacture. The THz prototyping technique we invented is based on a polymer jetting 3-D printing. Structures of arbitrary 3-D shape are decomposed into a series of 16- μm thick layers via a CAD design, which are sent sequentially to the prototyping machine. Polymer in liquid phase is jetted from a series of printer heads to form the structure within each slice, and is immediately cured by a UV lamp on the heads. Eventually, the structure is printed following the layer-by-layer sequence. Two structures with complete 3-D band gaps, namely the woodpile structure and the Johnson structure, which were originally proposed at optical frequencies, are scaled to between 200 and 300 GHz and fabricated by this method. Samples are characterized by THz time-domain spectroscopy (THz-TDS) and the result matches the simulations

very well. Therefore, we conclude that high fabrication accuracy is achievable from this technique. This technique is not only applicable for fast, low-cost and accurate THz EMXT component fabrication, but may also lead to systematic prototyping of an integrated THz micro-system. Quasi-3D metallization of the prototyped polymer structures by sputtering is also demonstrated during an attempt to fabricate the photonic cavity array as a proposed THz thermal radiation source. The metallization process, however, still needs improvement and further development.

Third, with the prototyping fabrication tool in hand, several polymer EMXT based THz components are investigated. EMXT structures already suit themselves as band pass/stop filters and reflectors because of their band gaps. With the refractive index contrast a polymer can provide with respect to air, a polymer EMXT shows good stop band depth for a normally incident EM wave. A polymer EMXT can also form a wave guiding structure if a defect channel is introduced into the complete EMXT. A dielectric THz waveguide based on a hollow-core EMXT fiber architect has been designed, fabricated and characterized in our group. Measurements agree fairly well with the design except for a constant 7 GHz downshift of the pass band features caused by the glossy printing inaccuracies. The extracted power loss factor of the waveguide from measurements demonstrates a propagation loss as low as 0.03 dB/mm at its primary operation frequency, due to its exclusion of conduction loss and its weak dependence on the build material dielectric loss. Parametric study of the waveguide design parameters is also conducted to further understand their effects on

the waveguide performance. These understandings provide guidelines for the EMXT horn antenna and waveguide-to-microstrip line transition designs later on.

Simply by expanding the core diameter to form a flare angle, the EMXT waveguide can evolve into a THz EMXT horn antenna. This EMXT antenna design is accomplished by optimizing its directivity and radiation efficiency via varying the axial length of the EMXT horn. Simulation of the optimized antenna design shows almost the same boresight directivity and main beam angular width with a copper horn antenna of identical dimensions at the low-frequency pass band. These performance specifications are much better than the copper horn antenna at higher-frequency pass bands of the EMXT antenna. Fabrication of the finalized EMXT antenna designs has been successful with the prototyping technique, and the measurement of the antenna radiation pattern is planned.

A transition from the EMXT hollow-core waveguide to a THz microstrip line is also proposed and designed to meet the demands to characterize THz semiconductor devices or planar samples using a free-space THz radiation system. More importantly, it is also proposed to integrate it with a THz planar source/detector to make the system a self-sufficient THz transceiver. The guided HE_{11} mode within the defect of the EMXT waveguide is coupled into the guided HE_{11} mode of a solid dielectric waveguide, and then directed onto the microstrip line via a tapered dielectric wedge with PEC flares terminating its top and bottom surfaces. Since the E-field is (quasi-)linearly polarized along the same direction and the dielectric wedge shrinks the field spread eventually to the size of the microstrip-line fundamental mode,

a good coupling of energy is expected. Simulations reveal a coupling and radiation loss of 2.115 dB from the transition section and a very small return loss, although the material loss is inevitably high since the fields are concentrated in the dielectric during the transition. Nevertheless, the overall insertion loss in our THz-TDS system is still acceptable for testing purposes. Fabrication and testing of the transition structure are currently underway. Most importantly, all of the above components can be integrated via THz rapid prototyping in a systematic manner, thus saving a lot of trouble with connections and alignments among the various components.

Unfinished works, as well as interesting extensions exist in both individual topics of this dissertation, and in a bigger picture associated with the integration of all of the various components. They also include achieving a comprehensive THz prototyping methodology.

For the topic of thermal radiation from an EMXT structure, the fundamental question to be answered is whether thermal emission from an EMXT can exceed the normal blackbody at the same temperature. To draw a solid conclusion on that, more obvious emission enhancements (or suppressions) than we have measured to date over the control blackbody are required. The thermal emission experiment needs to be improved: The FTS system has its prime signal-to-noise ratio between 600 GHz and 3.2 THz, so that a thermal emission measurement of an EMXT with its band features within this frequency range would be more reliable. The sample emission reception angle in the system is about 18 degrees, therefore if the EMXT radiation peak has a variation in both frequency and magnitude with the launching angle, the measured

radiation level would be a weighted average over this 18 degree angle and the enhancement may be smeared out. To decrease the reception angle and thus improve the measurement resolution, a smaller sample aperture or collimating mirror would be necessary. Also, to fully eliminate the transmission term in Equation (2.10) and have a more precise emissivity extraction, the EMXT sample should be laid against a metal plate so that almost zero radiation is coming from the back of the EMXT sample. All these issues are currently being addressed in our 1-D EMXT thermal radiation measurement series. Emission from a 2-D photonic cavity array exhibits a more promising large enhancement factor at THz frequencies. An attempt has been made to fabricate the sample discussed in Chapter 3; however, this effort has not been very successful. Eventually this structure will be fabricated and its thermal emissivity will be measured. Theoretically, our experiment result implies that the coupling between the interior photon modes and the outer-space propagation modes can not be omitted in the calculation; i.e., a prediction of the thermal emissivity based on infinite-lattice DOS is not enough. This missing piece in our calculation will be investigated in the future. Also it would be an interesting question to experimentally drive the EMXT structure into a non-equilibrium state. Then, according to theories [76, 105], the EMXT will have exceptionally high thermal emission. The question is worth some theoretical consideration first.

For the established THz rapid prototyping technique, metallization of the polymer is an immediate issue worth exploring. Sputtering will cause a heat-induced deformation of the polymer, and therefore applicability of other three-dimensional

metallization processes such as electroplating, electro-less deposition or e-beam writing onto the polymer need to be studied. The possibility to fabricate a THz microstrip line or CPW line circuits with the prototyping technique is also very interesting to explore, as proposed in Chapter 5. Another broad area that this fabrication technique suits itself in is the sub-wavelength area where the unit cell size of the periodic structure is much smaller than the design wavelength. Useful THz structures such as an effective medium with artificial anisotropy [91] and a gradient index antenna with designable far-field pattern [254] could potentially be realized by this THz rapid prototyping method. There are also possibilities to mix different printing materials such as conducting polymers and magnetic polymers during the prototyping. This would allow one to specify the spatial distribution of material properties that could be achieved. If micro-fluidic channels are integrated into the printed EMXT structure, liquid crystals can then be infiltrated into it and make the composite structure frequency-tunable.

For the topics associated with the THz EMXT waveguides, an EMXT horn antenna and a waveguide-to-planar circuit transition, many interesting aspects remain to be investigated. Waveguide bending is an important component when the propagation direction of the THz wave needs to be altered. Due to the fabrication freedom of the prototyping technique, an EMXT waveguide bent can be manufactured with very uniform bending corners, as well as any specific corner design to reduce the bending loss. This application is currently under study via simulations. Fabrication of the optimized EMXT antenna design has been accomplished and the test bench for its

antenna radiation-pattern measurements is under construction. Also, the potential to build a phased array antenna by integrating multiple EMXT antennas together is being considered. Phase synchronization among these antennas would need the realization of an EMXT waveguide-to-planar circuit transition. The currently proposed transition design has many aspects yet to be optimized. The practical fabrication of the transition system has several challenging points that need subtle processes. Again if a THz microstrip line can be fabricated via the prototyping technique, the integration of the transition sections with the microstrip line would not be necessary and the whole fabrication process would be greatly simplified. Once the transition system is realized, it will be possible to characterize THz samples and semiconductor devices in the time-domain using our THz-TDS. Integration of planar THz solid-state sources and detectors into the system would become feasible as well, and it will lead to a compact THz transceiver or imaging system.

Ultimately, with all the aforementioned THz components achieved in the future, efforts shall be put forth to realize the bigger picture of fabricating a THz micro-system in an integrated manner. As shown in Figure 6-1, every single THz component in the system can be prototyped with the 3-D printing technique. Therefore, the design of the whole system can be input into the 3-D printing machine and manufactured in a single fabrication. All the elaborations needed for mounting and alignment, when the components are fabricated individually, will be circumvented this way. The THz system would be inexpensive and precisely recurring the design that would be very easy to customize.

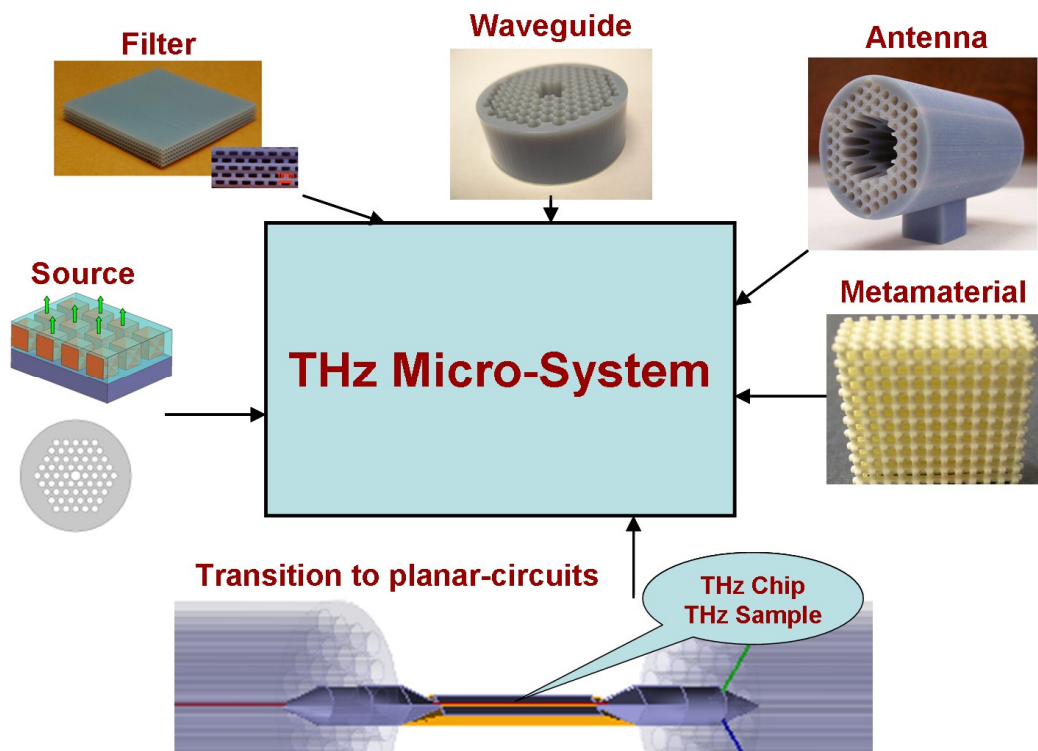


Figure 6-1. Integrated THz micro-system including various THz components. The system can be manufactured by the THz prototyping in a single fabrication.

REFERENCES

1. I. Hosako, N. Sekine, M. Patrashin, S. Saito, K. Fukunaga, Y. Kasai, P. Baron, T. Seta, J. Mendrok, S. Ochiai, and H. Yasuda, Proc. IEEE **95**, 1611 (2007).
2. E. Yablonovitch, Phys. Rev. Lett. **58**, 2059 (1987).
3. S. John, Phys. Rev. Lett. **58**, 2486 (1987).
4. J. D. Joannopoulos, S. G. Johnson, J. N. Winn, and R. D. Meade, *Photonic Crystals: Molding the Flow of Light*, 2nd Ed. (Princeton University Press, Princeton, 2008).
5. G. P. Williams, Rep. Prog. Phys. **69**, 301 (2006).
6. D. L. Woolard, E. R. Brown, M. Pepper, and M. Kemp, Proc. IEEE **93**, 1722 (2005).
7. H. M. Pickett, Proc. SPIE **3617**, 2 (1999).
8. H. J. Hansen, Proc. IEEE **95**, 1691 (2007).
9. D. Jaksch, J. I. Cirac, P. Zoller, S. L. Rolston, R. Cote, and M. D. Lukin, Phys. Rev. Lett. **85**, 2208 (2000).
10. S. G. Carter, V. Ciulin, M. S. Sherwin, M. Hanson, A. Huntington, L. A. Coldren, and A. C. Gossard, Appl. Phys. Lett. **84**, 840 (2004).
11. B. E. Cole, J. B. Williams, B. T. King, M. S. Sherwin, and C. R. Stanley, Nature **410**, 60 (2001).
12. N. Nagai, R. Kumazawa, and R. Fukasawa, Chem. Phys. Lett. **413**, 495 (2005).
13. B. N. Flanders and N. F. Scherer, Proc. SPIE **3273**, 256 (1998).
14. H. Ogasawara, D. Nordlund, and A. Nilsson, in Proc. 27th Intl. Free Electron Laser Conf. (Stanford, CA, 2005), pp. 343-346.
15. R. J. Foltynowicz, R. E. Allman, and E. Zuckerman, Chem. Phys. Lett. **431**, 34 (2006).

16. A. Markelz, S. Whitmore, J. Hillebrecht, and R. Birge, *Phys. Med. Bio.* **47**, 3797 (2002).
17. E. W. Castner, Jr. M. Maroncelli, and G. R. Fleming, *J. Chem. Phys.* **86**, 1090-1097 (1987).
18. B. N. Flanders, R. A. Cheville, D. Grischkowsky, and N. F. Scherer, *J. Phys. Chem.* **100**, 11824 (1996).
19. J. W. Waters, *Proc. IEEE* **80**, 1679 (1992).
20. M. S. Sherwin, C. A. Schmuttenmaer, and P. H. Bucksbaum, “*Opportunities in THz Science*,” Report of a DOE-NSF-NIH Workshop held February 12 – 14, 2004, Arlington, VA.
21. P. H. Siegel, *IEEE Trans. Microwave Theory Tech.* **50**, 910 (2002).
22. P. H. Siegel, *IEEE Trans. Microwave Theory Tech.* **52**, 2438 (2004).
23. D.M. Mittleman, M. Gupta, R. Neelamani, R.G. Baraniuk, J.V. Rudd, and M.Koch, *Appl. Phys. B.* **68**, 1085 (1999).
24. B. B. Hu and M. C. Nuss, *Opt. Lett.* **20**, 1716 (1995).
25. M. J. Fitch and R. Osiander, *John Hopkins APL Tech. Dig.* 25, 348 (2004).
26. K. Yamamoto, M. Yamaguchi, F. Miyamaru, M. Tani, M. Hangyo, T. Ikeda, A. Matsushita, K. Koide, M. Tatsuno, and Y. Minami, *Jap. J. Appl. Phys.* **43**, L414 (2004).
27. M. C. Kemp, P. F. Taday, B. E. Cole, J. A. Cluff, A. J. Fitzgerald, and W. R. Tribe, *Proc. SPIE* **5070**, 44 (2003).
28. C. Zandonella, *Nature* **424**, 721 (2003).
29. W. R. Tribe, D. A. Newnham, P. F. Taday, and M. C. Kemp, *Proc. SPIE* **5354**, 44 (2004).
30. B. M. Fischer, H. Helm, and P. U. Jepsen, *Proc. IEEE* **95**, 1592 (2007).
31. Y. C. Shen, T. Lo, P. F. Taday, B. E. Cole, W. R. Tribe, and M. C. Kemp, *Appl. Phys. Lett.* **86**, 241116 (2005).

32. M. Nagel, M. Forst, and H. Kurz, *J. Phys.: Condens. Matter* **18**, S601 (2006).
33. D. D. Arnone, C. M. Ciesla, A. Corchia, S. Egusa, M. Pepper, J. M. Chamberlain, C. Bezzant, E. H. Linfield, R. Clothier, and N. Khammo, *Proc. SPIE* **3828**, 209 (1999).
34. M. W. Burke, *Engineering Research and Technology Report*, FY07, 48 (2007).
35. A. R. Parker, *Materials Today* **5**, 26 (2002).
36. T. D. Drysdale, R. J. Blaikie, and D. R. S. Cumming, *Proc. SPIE* **5070**, 89 (2003).
37. P. de Maagt, R. Gonzalo, Y. C. Vardaxoglou, and J.-M. Baracco, *IEEE Trans. Antenn. Propag.* **51**, 2667 (2003).
38. Q. Chen and D. W.E. Allsopp, *Opt. Commun.* **281**, 5771 (2008).
39. T. Yoshie, J. Vuckovic, A. Scherer, H. Chen, and D. Deppe, *Appl. Phys. Lett.* **79**, 4289 (2001).
40. K. Busch, G. von Freymann, S. Linden, S. F. Mingaleev, L. Tkeshelashvili, and M. Wegener, *Phys. Report* **444**, 101 (2007).
41. J. S. Jensen, O. Sigmund, L. H. Frandsen, P. I. Borel, A. Harpoth, and M. Kristensen, *IEEE Photonics Technol. Lett.* **17**, 1041 (2005).
42. S. Fan, P. R. Villeneuve, J. D. Joannopoulos, and H. A. Haus, *Phys. Rev. Lett.* **80**, 960 (1998).
43. S. Fan, P. R. Villeneuve, J. D. Joannopoulos, and H. A. Haus, *Opt. Express* **3**, 4 (1998).
44. Y. Sugimoto, S. Lan, S. Nishikawa, N. Ikeda, H. Ishikawa, and K. Asakawa, *Appl. Phys. Lett.* **81**, 1946 (2002).
45. L. J. Wu, M. Mazilu, J. F. Gallet, T. F. Krauss, A. Jugessur, and R. M. De La Rue, *Opt. Lett.* **29**, 1620 (2004).
46. D. Pustai, S. Y. Shi, C. H. Chen, A. Sharkawy, and D. Prather, *Opt. Express* **12**, 1823 (2004).

47. P. V. Parimi, W. T. Lu, P. Vodo, J. Sokoloff, J. S. Derov, and S. Sridhar, *Phys. Rev. Lett.* **92**, 127401 (2004).
48. J. B. Pendry, *Phys. Rev. Lett.* **85**, 3966 (2000).
49. E. Cubukcu, K. Aydin, and E. Ozbay, S. Foteinopoulou, and C. M. Soukoulis, *Phys. Rev. Lett.* **91**, 207401 (2003).
50. O. Painter, R. K. Lee, A. Scherer, A. Yariv, J. D. O'Brien, P. D. Dapkus, and I. Kim, *Science* **284**, 1819 (1999).
51. D. Englund, D. Fattal, E. Waks, G. Solomon, B. Y. Zhang, T. Nakaoka, Y. Arakawa, Y. Yamamoto, and J. Vuckovic, *Phys. Rev. Lett.* **95**, 013904 (2005).
52. Z. Y. Li, *Phys. Rev. B* **66**, 241103 (2002).
53. S. Y. Lin, J. G. Fleming, and I. El-Kady, *Opt. Lett.* **28**, 1909 (2003).
54. H. Xin, Z. R. Wu, A. Young, and R. W. Ziolkowski, *IEEE Trans. Antenn. Propag.* **56**, 2970 (2008).
55. T. F. Krauss and R. M. De La Rue, *Prog. Quantum Electron.* **23**, 51 (1999).
56. G. Gruner, Ed., *Millimeter and Submillimeter Wave Spectroscopy of Solids*, chap. 1 (Springer, Berlin, German, 1998).
57. K. L. Wang and D.M. Mittleman, *J. Opt. Soc. B* **22**, 2001 (2005).
58. H. Eisele and G. Haddad, *IEEE Trans. Microwave Theory Tech.* **46**, 739 (1998).
59. L. Samoska, V. Radisic, M. Micovic, M. Hu, P. Janke, and C. Ngo, in 12th Intl. Space Terahz. Technol. Symp. (San Diego, CA, 2001), Paper 11.1.
60. A. Staprans, E. McCune, and J. Ruetz, *Proc. IEEE* **61**, 299 (1973).
61. A. Dobroiu, M. Yamashita, Y. N. Ohshima, Y. Morita, C. Otani, and K. Kawase, *Appl. Opt.* **43**, 5637 (2004).
62. E. R. Brown, F. W. Smith, and K. A. McIntosh, *J. Appl. Phys.* **73**, 1480 (1993).
63. E. R. Brown, K. A. McIntosh, K. B. Nichols, and C. L. Dennis, *Appl. Phys. Lett.* **66**, 285 (1995).

64. K. Kawase, M. Sato, T. Taniuchi, and H. Ito, *J. Appl. Phys.* **68**, 2483 (1996).
65. X. Zernike and P. R. Berman, *Phys. Rev. Lett.* **15**, 999 (1965).
66. C. C. Bradley, *Infrared Phys.* **12**, 287 (1972).
67. H. P. Roser, *Infrared Phys.* **32**, 385 (1991).
68. J. H. Smet, C. F. Fonstad, and Q. Hu, *J. Appl. Phys.* **79**, 9305 (1996).
69. B. Xu, Q. Hu, and M. R. Melloch, *Appl. Phys. Lett.* **71**, 440 (1997).
70. M. Reddy, S. C. Martin, A. C. Molnar, R. E. Muller, R. P. Smith, P. H. Siegel, M. J. Mondry, M. J. W. Rodwell, and S. J. Allen, Jr., in 8th Intl. Space Terahz. Technol. Symp. (Cambridge, MA, 1997), pp. 149-161.
71. M. Nagai, K. Tanaka, H. Ohtake, T. Bessho, T. Sugiura, T. Hirosumi, and M. Yoshida, *Appl. Phys. Lett.* **85**, 3974 (2004).
72. E. R. Mueller, *Submillimeter wave lasers*, in *Wiley Encyclopedia of Electrical and Electronics Engineering*. **20**, pp. 597-615 (Wiley, New York, 1999).
73. A. V. Raisanen, *Proc. IEEE* **80**, 1842-1852 (1992).
74. X. Melique, C. Mann, P. Mounaix, J. Thornton, O. Vanbesien, F. Mollot, and D. Lippens, *IEEE Microw. Guided Wave Lett.* **8**, 384 (1998).
75. M. Planck, *The Theory of Heat Radiation* (Dover, New York, 1959).
76. I. El-Kady, W. W. Chow, and J. G. Fleming, *Phys. Rev. B* **72**, 195110 (2005).
77. C. H. Seager, M. B. Sinclair, and J. G. Fleming, *Appl. Phys. Lett.* **86**, 244105 (2005).
78. C. D. Nordquist, M. C. Wanke, A. M. Rowen, C. L. Arrington, M. Lee, and A. D. Grine, in *IEEE AP-S Intl. Symp.* (San Diego, CA, 2008).
79. T. Ito, Y. Matsuura, M. Miyagi, H. Minamide, and H. Ito, *J. Opt. Soc. Am. B.* **24**, 1230 (2007).

80. B. Martinez, I. Ederra, R. Gonzalo, B. Alderman, L. Azcona, P. G. Huggard, B. D. Hon, A. Hussain, S. R. Andrews, L. Marchand, and P. de Maagt, *IEEE Trans. Microwave Theory Tech.* **55**, 672 (2007).
81. R. Gonzalo, B. Martinez, C. M. Mann, H. Pellemans, P. H. Bolivar, and P. de Maagt, *IEEE Trans. Microwave Theory Tech.* **50**, 2384 (2002).
82. E. Öbay, E. Michel, G. Tuttle, R. Biswas, K. M. Ho, J. Bostak, and D. M. Bloom, *Opt. Lett.* **10**, 1155 (1994).
83. F. Laermer and A. Urban, *Microelectron. Eng.* **67–68**, 349 (2003).
84. G. Kiriakidis and N. Katsarakis, *Mater. Phys. Mech.* **1**, 20 (2000).
85. A. Dupuis, J.-F. Allard, D. Morris, K. Stoeffler, C. Dubois, and M. Skorobogatiy, *Opt. Express* **17**, 8012 (2009).
86. M. Goto, A. Quema, H. Takahashi, S. Ono, and N. Sarukura, *Jpn. J. Appl. Phys.* **43**, L317 (2004).
87. K. Nielsen, H. K. Rasmussen, A. J. L. Adam, P. C. M. Planken, O. Bang, and P. U. Jepsen, *Opt. Express* **17**, 8592 (2009).
88. M. Skorobogatiy and A. Dupuis, *Appl. Phys. Lett.* **90**, 113514 (2007).
89. J. Y. Lu, C. P. Yu, H. C. Chang, H. W. Chen, Y. T. Li, C. L. Pan, and C. K. Sun, *Appl. Phys. Lett.* **92**, 064105 (2008).
90. B. S. Liu, X. Gong, and W. J. Chappell, *IEEE Trans. Microwave Theory Tech.* **52**, 2567 (2004).
91. K. F. Brakora, J. Halloran, and K. Sarabandi, *IEEE Trans. Antenn. Propag.* **55**, 790 (2007).
92. V. K. Varadan, X. Jiang, and V. V. Varadan, *Microstereolithography and Other Fabrication Techniques for 3D MEMS* (Wiley, Chichester, U.K., 2001).
93. N. Delhote, D. Baillargeat, S. Verdeyme, M. Thevenot, C. Delage, and C. Chaput, *IEEE MTT-S Intl. Microwave Symp. Dig.* **4**, 1431 (2007).
94. A. Tal, Y. S. Chen, H. E. Williams, R. C. Rumpf, and S. M. Kuebler, *Opt. Express* **15**, 18283 (2007).

95. P. C. Hidber, P. F. Nealey, W. Helbig, and G. M. Whitesides, *Langmuir* **12**, 5209 (1996).
96. M. B. Schubert, *Thin Solid Films* **377**, 240 (1997).
97. J. K. Rath, A. J. Hardeman, C. H. M. van der Werf, P. A. T. T. van Veenendaal, M. Y. S. Rusche, and R. E. I. Schropp, *Mat. Res. Soc. Symp. Proc.* **762**, A6.7.1 (2003).
98. J. W. Fleming, *IEEE Trans. Microwave Theory Tech.* **22**, 1023 (1974).
99. R. J. Dengler, A. Skalare, and P. H. Siegel, *IEEE MTT-S Intl. Microwave Symp. Dig.* **3**, 1951 (2004).
100. J. R. Ashley and F. M. Palka, *IEEE MTT-S Intl. Microwave Symp. Dig.* **73**, 181 (1973).
101. E. J. Nichols and J. D. Tear, *Astrophys. J.* **61**, 17 (1925).
102. P. Coleman, *IEEE Trans. Microwave Theory Tech.* **11**, 271 (1963).
103. A. Maestrini, J. S. Ward, J. J. Gill, H. S. Javadi, E. Schlecht, C. T. Canseliet, G. Chattopadhyay, and I. Mehdi, *IEEE Trans. Microwave Theory Tech.* **53**, 2835 (2005).
104. C. H. Chao, C. Y. Kang, and C. F. Lin, in *Optics and Photonics* (Tainan, Taiwan, 2005).
105. W. W. Chow, *Phys. Rev. A* **73**, 013821 (2006).
106. I. Celanovic, F. O'Sullivan, M. Ilak, J. Kassakian, and D. Perreault, *Opt. Lett.* **29**, 863 (2004).
107. S. Y. Lin, J. G. Fleming, E. Chow, Jim Bur, K. K. Choi, and A. Goldberg, *Phys. Rev. B* **62**, R2243 (2000).
108. C. F. Lin, C. H. Chao, L. A. Wang, and W. C. Cheng, *J. Opt. Soc. Am. B* **22**, 1517 (2005).
109. C. M. Cornelius and J. P. Dowling, *Phys. Rev. A* **59**, 4736 (1999).
110. A. Narayanaswamy and G. Chen, *Phys. Rev. B* **70**, 125101 (2004).

111. C. Luo, A. Narayanaswamy, G. Chen, and J. D. Joannopoulos, Phys. Rev. Lett. **93**, 213905 (2004).
112. T. Trupke, P. Wurfel, and M. A. Green, Appl. Phys. Lett. **84**, 1997 (2004).
113. S. Noda, K. Tomoda, N. Yamamoto, and A. Chutinan, Science **289**, 604 (2000).
114. H. Han, H. Park, M. Cho, and J. Kim, Appl. Phys. Lett. **80**, 2634 (2002).
115. D. Arnone, Technology Review **107**, 32 (2004).
116. S. Y. Lin, J. Moreno, and J. G. Fleming, Appl. Phys. Lett. **83**, 380 (2003).
117. S. Y. Lin, J. Moreno, and J. G. Fleming, Appl. Phys. Lett. **84**, 1999 (2004).
118. J. G. Fleming, Appl. Phys. Lett. **86**, 249902 (2005).
119. J. H. Lee, Y. S. Kim, K. Constant, and K. M. Ho, Adv. Mater. **19**, 791 (2007).
120. S. Y. Lin, J. G. Fleming, D. L. Hetherington, B. K. Smith, R. Biswas, K. M. Ho, M. M. Sigalas, W. Zubrzycki, S. R. Kurtz, and Jim Bur, Nature **394**, 251 (1998).
121. S. G. Johnson and J. D. Joannopoulos, Opt. Express **8**, 173 (2001).
122. G. Lehmann and M. Taut, Phys. Stat. Sol. (b) **54**, 469 (1972).
123. O. Jepsen and O. K. Anderson, Solid State Commun. **9**, 1763 (1971).
124. High Frequency Structure Simulator, Version 11, Ansoft Corporation, 2008.
125. R. C. Jaeger, "Thermal oxidation of silicon," *Introduction to Microelectronic Fabrication* (Prentice Hall, Upper Saddle River, New Jersey, 2002).
126. F. Kusunoki, J. Takahara, and T. Kobayashi, Elec. Lett. **39**, 23 (2003).
127. F. Kusunoki, T. Kohama, T. Hiroshima, S. Fukumoto, J. Takahara, and T. Kobayashi, Jap. J. Appl. Phys. **43**, 5253 (2004).
128. H. Yokoyama, Science **256**, 66 (1992).
129. D. K. Cheng, *Field and Wave Electromagnetics*, 2nd Ed. (Addison-Wesley, New York, 1989).

130. S. Maruyama, T. Kashiwa, H. Yugami, and M. Esashi, *Appl. Phys. Lett.* **79**, 1393 (2001).
131. M. Sugawara and B. L. Stansfield, *Plasma Etching: Fundamentals and Applications* (Oxford University Press, New York, 1998).
132. J. R. Sheats and B. W. Smith, *Microlithography: Science and Technology* (Marcel Dekker, New York, 1998).
133. J. W. Lamb, *Intl. J. Infrared Milli. Waves* **17**, 1997 (1996).
134. P. Y. Han, M. Tani, M. Usami, S. kono, R. Kersting, and X. C. Zhang, *J. Appl. Phys.* **89**, 2357 (2001).
135. R. H. Giles and T. M. Horgan, "Silicone-Based Wedged-Surface Radiation Absorbing Material," U.S. Patent Number 5,260,513 (1993).
136. H. Xin, Z. R. Wu, A. Young, and R. W. Ziolkowski, in *Proc. IEEE AP-S Intl. Symp.* (Honolulu, HI, 2007), pp. 2249-2252.
137. J. G. Fleming, S. Y. Lin, I. El-Kady, R. Biswas, and K. M. Ho, *Nature* **417**, 52 (2002).
138. B. Kraabel, M. Shiffmann, and P. Gravisse, "On the validity of Kirchhoff's law", unpublished.
139. F. Nicodemus, *Appl. Opt.* **4**, 767 (1965).
140. C. J. Schuler, C. Wolff, K. Busch, and M. Florescu, *Appl. Phys. Lett.* **95**, 241103 (2009).
141. P.-M. Robitaille, *IEEE Trans. Plasma Sci.* **31**, 1263 (2003).
142. B. Ferguson and X.C. Zhang, *Nat. Mater.* **1**, 26 (2002).
143. Z. L. Lu, S. Y. Shi, J. A. Murakowski, G. J. Schneider, C. A. Schuetz, and D. W. Prather, *Phys. Rev. Lett.* **96**, 173902 (2006).
144. N. Delhote, D. Baillargeat, S. Verdeyme, C. Delage, and C. Chaput, *IEEE Trans. Microwave Theory Tech.* **55**, 548 (2007).
145. Objet™, <http://www.2objet.com/Default.aspx>.

146. Microwave Studio, Computer Simulation Technology, 2006.
147. Z. R. Wu, L. Wang, Y. T. Peng, A. Young, S. Seraphin, and H. Xin, *J. Appl. Phys.* **103**, 094324 (2008).
148. K. M. Ho, C. T. Chan, C. M. Soukoulis, C. M., R. Biswas, and M. Sigalas, *Solid State Commun.* **89**, 413 (1994).
149. P. U. Jepsen and B. M. Fischer, *Opt. Lett.* **30**, 29 (2005).
150. S. G. Johnson and J. D. Joannopoulos, *Appl. Phys. Lett.* **77**, 3490 (2000).
151. M. Qi, E. Lidorikis, P. T. Rakich, S. G. Johnson, J. D. Joannopoulos, E. P. Ippen, and H. I. Smith, *Nature* **429**, 538 (2004).
152. S. Y. Lin, D. X. Ye, T. M. Lu, J. Bur, Y. S. Kim, and K. M. Ho, *J. Appl. Phys.* **99**, 083104 (2006).
153. W. R. McGrath, C. Walker, M. Yup, and Y. C. Tai, *IEEE Microwave Guided Wave Lett.* **3**, 61 (1993).
154. G. O. Mallory and J. B. Hajdu, Ed., *Electroless Plating* (William Andrew Publishing, Norwich, New York, 1990).
155. S. Atakaramians, S. Afshar V. B. M. Fischer, D. Abbott, and T. M. Monro, *Opt. Express* **16**, 8845 (2008).
156. R. Mendis and D. Grischkowsky, *Opt. Lett.* **26**, 846 (2001).
157. K. Wang and D. M. Mittleman, *Nature* **432**, 376 (2004).
158. T. I. Jeon, J. Zhang, and K. W. Goossen, *Appl. Phys. Lett.* **86**, 161904 (2005).
159. T. I. Jeon and D. Grischkowsky, *Appl. Phys. Lett.* **85**, 6092 (2004).
160. L. J. Chen, H. W. Chen, T. F. Kao, J. Y. Lu, and C. K. Sun, *Opt. Lett.* **31**, 308 (2006).
161. Z. R. Wu, J. Kinast, M. E. Gehm, and H. Xin, *Opt. Express* **16**, 16442 (2008).
162. Z. R. Wu, W.-R. Ng, M. Gehm, and H. Xin, in *IEEE MTT-S Intl. Microwave Symp.* (Anaheim, CA, 2010).

163. Lumerical MODE Solutions package, v2.3, 2009.
164. P. F. Goldsmith, *Quasioptical systems: Gaussian beam quasioptical propagation and applications* (IEEE Press, Piscataway, New Jersey, 1997).
165. W. H. Yu, Y. J. Liu, T. Su, H. Neng-Tien, and M. Raj., IEEE Antenn. Propag. Mag. **47**, 39 (2005).
166. D. M. Pozar, *Microwave Engineering*, 2nd Ed. (John Wiley & Sons, Inc., New York, 2005).
167. J. C. Daly, *Fiber Optics* (CRC Press, Inc., Boca Raton, Florida, 2000).
168. L. Wang, *Investigation of Carbon Nanotube Properties and Applications at Microwave and THz Frequencies*, Ph. D. dissertation, University of Arizona, 2010.
169. J. V. Rudd, J. L. Johnson, and D. M. Mittleman, Opt. Lett. **25**, 1556 (2000).
170. C. Fumeaux, G. D. Boreman, W. Herrmann, F. K. Neubuhi, and H. Rothuizen, Appl. Phys. Lett. **38**, 37 (1999).
171. G. M. Rebeiz, L. F. B. Katehi, W. Y. Ali-Ahmad, G. V. Eleftheriadws, and C. C. Ling, IEEE Antenn. Propag. Mag. **34**, 7 (1992).
172. M. Bin, Ph. D. dissertation, California Institute of Technology, 1997.
173. J. A. Deibel, M. D. Escarra, and D. M. Mittleman, in Quant. Electron. Laser Sci. Conf. (QELS, Baltimore, MD, 2005), pp. 1239-1241.
174. M. C. Hoffmann, *Novel Techniques in THz-Time-Domain Spectroscopy: A Comprehensive Study of Technical Improvements to THz-TDS*, Ph. D. dissertation, Albert-Ludwigs-Universitat, 2006.
175. S. S. Gearhart, C. C. Ling, G. M. Rebeiz, H. Davee, and G. Chin, IEEE Microwave Guided Wave Lett. **1**, 155 (1991).
176. K. Han, T. K. Nguyen, I. Park, and H. Han, J. Infrared Milli. Terahz. Waves **31**, 441 (2010).
177. P. J. Burke, in Proceedings of SPIE, 5593 (SPIE, Bellingham, WA, 2004), pp.52-61.

178. Y. Lan, B. Zeng, H. Zhang, B. Chen, and Z. Yang, *Intl. J. Infrared Milli. Waves.* **27**, 871 (2006).
179. Y. Wang, Q. Wu, W. Shi, X. J. He, X. F. Sun, and T. L. Gui, *Intl. J. Infrared Milli. Waves.* **29**, 35 (2008).
180. E. R. Brown, O. B. McMahon, and C. D. Parker, *Lincoln Lab J.* **11**, 159 (1998).
181. E. R. Brown, C. D. Parker, and E. Yablonovitch, *J. Opt. Soc. Am. B* **10**, 404 (1993).
182. A. Sharma, V. K. Dwivedi, and G. Singh, in *Prog. Electro. Mag. Res. Symp.* (Cambridge, MA, 2008), pp. 161-165.
183. D. Serhal, M. Hajj, R. Chantalat, J. Drouet, and B. Jecko, *IEEE Antenn. Wireless Propag. Lett.* **8**, 620 (2009).
184. K. C. Huie, *Microstrip Antennas: Broadband Radiation Patterns Using Photonic Crystal Substrates*, M. Sci. thesis, Virginia Polytechnic Institute, 2002.
185. R. Gonzalo, I. Ederra, C. M. Mann, and P. de Maagt, *Electron. Lett.* **37**, 613 (2001).
186. G. Singh, *Infrared Phys. Tech.* **53**, 17 (2010).
187. B. Temelkuran, M. Bayindir, E. Ozbay, R. Biswas, M. M. Sigalas, G. Tuttle, and K. M. Ho, *J. Appl. Phys.* **87**, 603 (2000).
188. Z. Y. Zhao, Q. L. Deng, H. L. Xu, C. L. Du, and X. G. Luo, *Microwave Opt. Technol. Lett.* **50**, 965 (2008).
189. M. Iida, M. Tani, P. Gu, K. Sakai, M. Watanabe, H. Kitahara¹, S. Kato, M. Suenaga, H. Kondo, and M. W. Takeda, *Jpn. J. Appl. Phys.* **42**, L1442 (2003).
190. Y. Lee, S. Tanaka, N. Uetake, S. Fujisaki, R. Inoue, and M. Tonouchi, *Appl. Phys. B* **87**, 405 (2007).
191. C. H. Chen, S. Y. Shi, D. W. Prather, and A. Sharkawy, *Opt. Eng.* **43**, 174 (2004).
192. A. R. Weily, K. P. Esselle, and B. C. Sanders, *Phys. Rev. E* **68**, 016609 (2003).

193. A. R. Weily, L. Horvath, K. P. Esselle, B. C. Sanders, and T. S. Bird, *IEEE Trans. Antenn. Propag.* **53**, 216 (2005).
194. A. R. Weily, K. P. Esselle, and B. C. Sanders, *Phys. Rev. E* **70**, 037602 (2004).
195. A. R. Weily, K. P. Esselle, T. S. Bird, and B. C. Sanders, *IEEE Trans. Antenn. Propag.* **54**, 2263 (2006).
196. Y. Q. Jiang, B. Howley, Z. Shi, Q. J. Zhou, R. T. Chen, M. Y. Chen, G. Brost, and C. Lee, *IEEE Photon. Tech Lett.* **17**, 187 (2005).
197. H. Subbaraman, M. Y. Chen, and R. T. Chen, *Appl. Opt.* **47**, 6448 (2008).
198. C. A. Balanis, *Antenna Theory: Analysis and Design*, 3rd Ed. (John Wiley & Sons, Inc., New York, 2005).
199. D. T. Young and J. C. Irwin, *Proc. IEEE* **53**, 2130 (1965).
200. M. C. Gaidis, H. M. Pickett, C. D. Smith, R. P. Smith, S. C. Martin, and P. H. Siegel, *IEEE Trans. Microwave Theory Tech.* **48**, 733 (2000).
201. N. Wyborn, in *Eur. Space Agency Symp.* (Grenoble, France, 1997), pp. 19-24.
202. A. Karpov, D. Miller, F. Rice, J. Zmuidzinas, J. A. Stern, B. Bumble, and H. G. Leduc, in *8th Intl. Superconduct. Electron. Conf.* (Osaka, Japan, 2001), pp. 521-522.
203. R. Blundel and C. Y. E. Tong, *Proc. IEEE* **80**, 1702 (1992).
204. J. E. Carlstrom and J. Zmuidzinas, *Reviews of Radio Science 1993–1995*, W. R. Stone, Ed. (Oxford Univ. Press, Oxford, UK, 1996).
205. S. Cherednichenko, in *12th Intl. Space Terahz. Technol. Symp.* (San Diego, CA, 2001), Paper 6.1.
206. B. S. Karasik, M. C. Gaidis, W. R. McGrath, B. Bumble, and H. G. LeDuc, *Appl. Phys. Lett.* **71**, 1567 (1997).
207. A. D. Semenov, H. W. Hubers, J. Schubert, G. N. Goltsman, A. I. Elantiev, B. M. Voronov, and E. M. Gershenzon, in *11th Intl. Space Terahz. Technol. Symp.* (Ann Arbor, MI, 2000), pp. 39-48.

208. S. Weinreb, T. Gaier, R. Lai, M. Barsky, Y. C. Leong, and L. Samoska, *IEEE Microwave Guided Wave Lett.* **9**, 282 (1999).
209. S. Martin, B. Nakamura, A. Fung, P. Smith, J. Bruston, A. Maestrini, F. Maiwald, P. H. Siegel, E. Schlecht, and I. Mehdi, *IEEE MTT-S Intl. Microwave Symp. Dig.* **3**, 1641 (2001).
210. A. Maestrini, J. Bruston, D. Pukala, S. Martin, and I. Mehdi, *IEEE MTT-S Intl. Microwave Symp. Dig.* **3**, 1657 (2001).
211. F. Maiwald, S. Martin, J. Bruston, A. Maestrini, T. Crawford, and P. H. Siegel, *IEEE MTT-S Intl. Microwave Symp. Dig.* **3**, 1637 (2001).
212. D. H. Austen, *Appl. Phys. Lett.* **26**, 101 (1975).
213. S. Verghese, K. A. McIntosh, and E. R. Brown, *IEEE Trans. Microwave Theory Tech.* **45**, 1301 (1997).
214. M. D. Janezic, E. F. Kuester, and J. Baker-Jarvis, *IEEE MTT-S Intl. Microwave Symp. Dig.* **3**, 1817 (2004).
215. J. Baker-Jarvis, M. D. Janezic, and C. A. Jones, *IEEE Trans. Instrum. Measure.* **47**, 338 (1998).
216. P. Gravesen, K. R. Poulsen, and H. Dirac, *J. Diabetes Sci. Technol.* **1**, 372 (2007).
217. F. D. Q. Pereira, P. V. Castejon, J. L. G. Tornero, D. C. Rebenaque, J. P. Garcia, and A. A. Melcon, *Microwave Opt. Technol. Lett.* **45**, 563 (2005).
218. N. S. Seong and S. O. Park, *Microwave Opt. Technol. Lett.* **48**, 2454 (2006).
219. M. H. Ho and C. I. G. Hsu, *Electron. Lett.* **41**, 1202 (2005).
220. B. S. Wang, *IEEE Trans. Microwave Theory Tech.* **37**, 1006 (1989).
221. L. Fan, M. Y. Li, and K. Chang, *Electron. Lett.* **31**, 294 (1995).
222. J. Navarro, *Microwave Opt. Technol. Lett.* **34**, 253 (2002).
223. M. Razaz and J. B. Davies, *Electron. Lett.* **10**, 324 (1974).

224. Z. X. Shen and R. H. MacPhie, *Microwave Opt. Technol. Lett.* **27**, 183 (2000).
225. D. N. Bykov, N. M. Bykov, A. I. Klimov, I. K. Kurkan, and V. V. Rostov, *Electron. Radio Eng.* **51**, 724 (2008).
226. Y. Chuan and W. Geyi, *Microwave Opt. Technol. Lett.* **19**, 225 (1998).
227. M. D. Deshpande and B. N. Das, *IEEE Trans. Microwave Theory Tech.* **25**, 954 (1977).
228. M. K. Thumm and W. Kasparek, *IEEE Trans. Plasma Sci.* **30**, 755 (2002).
229. P. Wade, *Understanding Circular Waveguide — Experimentally*, online article, <http://www.qsl.net/n1bwt/preface.htm>, Ch. 6.5.
230. J. W. Kooi, G. Chattopadhyay, S. Withington, F. Rice, J. Zmuidzinas, C. Walker, and G. Yassin, *Intl. J. Infrared Milli. Waves* **24**, 261 (2003).
231. Y. C. Shih, T. N. Ton, and L. Q. Bui, *IEEE MTT-S Intl. Microwave Symp. Dig.* **1**, 473 (1988).
232. G. Yassin and S. Withington, *Intl. J. Infrared Milli. Waves* **17**, 1685 (1996).
233. Y. C. Leong and S. Weinreb, *IEEE MTT-S Intl. Microwave Symp. Dig.* **6**, 1435 (1999).
234. J. H. C. van Heuven, *IEEE Trans. Microwave Theory Tech.* **24**, 144 (1976).
235. G. Yassin, R. Padman, S. withington, K. Jacobs, and S. Wulff, *Electron. Lett.* **33**, 498 (1997).
236. G. Yassin, S. Withington, M. Buffey, K. Jacobs, and S. Wulff, *IEEE Trans. Microwave Theory Tech.* **48**, 662 (2000).
237. H. Iizuka, T. Watanabe, K. Sato, and K. Nishikawa, *R&D Review of Toyota CRDL* **37**, 13 (2002).
238. W. Simon, M. Werthen, and I. Wolff, *IEEE MTT-S Intl. Microwave. Symp. Dig.* **1**, 257 (1998).
239. J. A. Miller, M. Y. Li, and K. Chang, *Microwave Opt. Technol. Lett.* **2**, 393 (1989).

240. C. Yeh, T. Y. Otoshi, and F. I. Shimabukuro, TDA Progress Report 42-117, May 15th, 1994.
241. T. N. Trinh, J. A. G. Malherbe, and R. Mittra, IEEE MTT-S Intl. Microwave Symp. Dig. **80**, 205 (1980).
242. C. S. Ponseca, Jr., E. Estacio, R. Pobre, G. Diwa, G. de los Reyes, S. Ono, H. Murakami, N. Sarukura, K. Aosaki, Y. Sakane, H. Sato, A. Argyros, and M. C. J. Large, J. Opt. Soc. Am. B **26**, A95 (2009).
243. A. Suntives and R. Abhari, IEEE Trans. Adv. Packaging **30**, 163 (2007).
244. A. Mekis and J. D. Joannopoulos, J. Lightwave Technol. **19**, 861 (2001).
245. J. Bauer and S. John, Phys. Rev. A **77**, 013819 (2008).
246. R. A. Stern and R. W. Babbitt, "Microstrip to Dielectric Waveguide Transition," U.S. Patent Number 4,745,377 (1998).
247. R. M. Knox, "Dielectric waveguide to TEM transmission line signal launcher," U.S. Patent Number 5,107,231 (1992).
248. A. G. Engel, N. I. Dib, and L. P. B. Katehi, IEEE Trans. Microwave Theory Tech. **42**, 847 (1994).
249. F. Schnieder and W. Heinrich, Frequenz **59**, 5-6 (2005).
250. C. Wood, J. Cunningham, I. C. Hunter, P. Tosch, E. H. Linfield, and A. G. Davies, Intl. J. Infrared Milli. Waves **27**, 557 (2006).
251. Rogers Corporation, <http://www.rogerscorp.com/>.
252. C. Yeh and F. I. Shimabukuro, *The Essence of Dielectric Waveguides* (Springer, New York, 2008).
253. G. Armbrrecht, C. Zietz, E. Denicke, and I. Rolfes, in 4th CST Euro. User Group Meeting (Darmstadt, Germany, 2009).
254. W. R. Ng, Z. R. Wu, H. Xin, and M. E. Gehm, in Frontiers in Optics, OSA Technical Digest (San Jose, CA, 2009), paper FWX2.